A NUMERICAL STUDY OF CONVECTION IN A CHANNEL WITH POROUS BAFFLES

A Thesis

by

BRUNO MONTE DA SILVA MIRANDA

Submitted to the Office of Graduate Studies of
Texas A&M University
in partial fulfillment of the requirements for the degree of

MASTER OF SCIENCE

December 2003

Major Subject: Mechanical Engineering

A NUMERICAL STUDY OF CONVECTION IN A CHANNEL WITH POROUS BAFFLES

A Thesis

by

BRUNO MONTE DA SILVA MIRANDA

Submitted to Texas A&M University
in partial fulfillment of the requirements
for the degree of

MASTER OF SCIENCE

Approved as to style and content by:

Nagamangala K. Anand (Chair of Committee)	Kumbakonam Rajagopal (Member)
Hamn-Ching Chen (Member)	Dennis L. O'Neal (Head of Department)

December 2003

Major Subject: Mechanical Engineering

ABSTRACT

A Numerical Study of Convection in a Channel
with Porous Baffles. (December 2003)
Bruno Monte da Silva Miranda, B.E.,
N.E.D University of Engineering & Technology, Pakistan
Chair of Advisory Committee: Dr. N.K. Anand

The effects on heat transfer in a two-dimensional parallel plate channel with sixteen porous baffles in a staggered arrangement with a uniform heat flux heating applied to the top and bottom walls has been numerically investigated. Developing Flow (DF) was considered for this study. The Brinkman-Forchheimer-extended Darcy model was used for modeling the heat transfer and fluid flow through the porous baffles. The flow was assumed to be laminar. A finite volume based method in conjunction with the SIMPLEC algorithm was used to solve the model equations. Calculations were made by varying several independent parameters such as Reynolds number (Re), Darcy number (Da), thermal conductivity ratio $\left({}^{k_e}\!/_{k_f}\right)$, baffle thickness $\left(W^* = {}^{H}\!/_{w}\right)$, non-dimensional baffle spacing $\left(D^* = {}^{d}\!/_{w}\right)$, and non-dimensional baffle height $\left(B^* = {}^{b}\!/_{H}\right)$.

The results of the study established that porous baffles out perform solid baffles from a pressure drop point of view. However, porous baffles under perform solid baffles from a heat transfer point of view. The ratio representing increase in heat transfer per unit increase in pumping power (heat transfer performance ratio) was found to be less than unity for all cases. Increasing the Darcy number was found to produce less desirable heat transfer enhancement ratios. Increasing the non-dimensional baffle spacing (d/w) and the baffle aspect ratio (H/w) were found to enhance heat transfer.

To my maternal grand parents

Alba Lucinda Colaco de Sa

and

Bruno Joseph de Sa

Without whom I could have never come so far

ACKNOWLEDGEMENTS

It is with great satisfaction and a sense of accomplishment that I present this thesis, “A Numerical Study of Convection in a Channel with Porous Baffles”. I would like to express my gratitude and deepest appreciation to Dr. N.K. Anand for his untiring assistance, encouragement, vision, and patience that has helped me successfully accomplish this research. I am also grateful to Dr. Anand for proof-reading and scrutinizing this thesis. I extend my appreciation to Dr. K. Rajagopal and Dr. H.C. Chen for their consideration shown by serving on my advisory committee.

I thank my office mate Mr. Ko, for helping me debug my code. I also need to thank the staff of the Department of Mechanical Engineering for their kindness and help provided during my studies at Texas A&M University.

Finally, I thank my mother Zelia de Sa Miranda for the financial and moral support given me during the difficult periods of my research. I am grateful to my maternal grandmother and grandfather who taught me that if I worked hard enough the stars could come to me and that honesty is the key to education.

TABLE OF CONTENTS

Page

CHAPTER

Page

LIST OF TABLES

TABLE Page

TABLE Page

LIST OF FIGURES

FIGURE Page

FIGURE Page

CHAPTER I

INTRODUCTION

In channel flows, the heat transfer rate is known to be high in the entrance region. This is because the hydrodynamic and thermal boundary layers are developing in this region. Thickness of both these boundary layers increases in the stream-wise direction. Far from the entrance of the channel the thickening of the boundary layers results in poor heat transfer, because the dominant method by which heat transfer takes place is diffusion.

To enhance the heat transfer it is desirable to periodically disrupt the hydrodynamic and thermal boundary layers, so that a series of entry lengths can be created. Higher heat transfer coefficients are associated with each entry length. Disruption of the boundary layers can be achieved by inserting solid baffles in the channel. Although, the use of solid baffles enhances heat transfer it results in larger pressure drops as the fluid flows over the solid baffles. This in turn implies that a more powerful blower or pumping source would be required if solid baffles were to be used.

The use of porous baffles does not suffer from the problems of solid baffles as a fluid can flow through the porous baffles. The through flow results in lower pressure drops. Periodic positioning of baffles results in periodic interruptions in hydrodynamic and thermal boundary layers resulting in a series of entry lengths. Higher heat transfer coefficients are associated with each entry length. In addition, the use of porous baffles

---

Thesis style and format follow that of ASME Journal of Heat Transfer.

increases the contact area between the solid surface and the fluid. The porous baffles provide a feasible economic alternative to heat transfer enhancement. Therefore, heat transfer problems involving forced convection in a channel, having partial or completely filled porous media, have been of considerable interest to industry because of the wide range of industrial applications that can be derived by such inclusions. Thus studies of heat transfer problems in porous media tend to be investigated especially those that relate to industries that manufacture direct contact heat exchangers, electronic cooling packages, and heat pipes.

A porous media is said to be unsaturated for flows involving more than one fluid flowing through the porous matrix. However, a homogenous porous media completely flooded by a homogenous fluid in a single phase is called a saturated porous media. A numerical investigation of developing flow (DF) was conducted to study the effects, of using saturated porous baffles in a two-dimensional rectangular channel, on pressure drop and heat transfer. In this study, consideration was given to porous baffles with varying permeability and geometry. The porous baffles were positioned alternately on the top and bottom walls of the channel.

This thesis contains a detailed description of the numerical study that was conducted to investigate the effects of porous baffles on heat transfer and fluid flow in a two-dimensional parallel plate channel. An account of the literature survey with particular emphasis on heat transfer enhancements using porous media in two-dimensional channels is given in Chapter 2. The derivations of the governing equations that were used to simulate the flow and heat transfer in the porous media are shown in Chapter 3.

A description of the basic concepts needed to develop the finite volume code are illustrated in Chapter 4. A rigorous validation of the code and systematic grid independence was done and the documentation of it can be found in Chapter 5. Representative results and the interpretation of these results are documented in Chapter 6. Concluding remarks on this study and some suggestions for future work can be found in Chapter 7.

CHAPTER II

LITERATURE SURVEY

In the extensive literature survey that was conducted before starting this research topic, it was found that there is no dearth of information on porous packed bed media. This includes both experimental and numerical studies. A porous packed bed setup is formed when a porous media is sandwiched between two parallel plates, the porous media being the same length as the parallel plates. On the other hand, reported experimental work is meager on forced flows in channels with porous media obstacles. This could also be attributed to the fact that packed bed porous media applications are heavily utilized in industries affiliated with heat exchangers, nuclear power generation, and oil drilling exploration. Nevertheless, a plethora of research has been conducted using numerical techniques on problems including forced convection in porous media. Such forced convection problems can be classified into two distinct groups. They are the internal and the external flows in which the porous media could take the form of substrates, blocks, or baffles.

Huang and Vafai [1], through numerical study successfully demonstrated that significant heat transfer enhancements could be achieved by the inclusion of porous baffles in a parallel plate channel. Consideration was given to a two-dimensional rectangular channel with four porous blocks attached to the bottom wall of the channel. Isothermal boundary conditions were imposed at the walls. The parabolic velocity and uniform temperature profile were used as the boundary conditions at the entrance of the channel. A Reynolds number (based on channel height) in the range of 750 - 1500 was considered. A finite volume based approach was used for the numerical investigation. Because of the lack of experimental data, the effective viscosity of the fluid in the porous matrix was assumed to be the same as the viscosity of the fluid in the clear medium. Air was taken to be the primary working fluid and the flow was assumed to be laminar for the study. The effects of Reynolds number, Darcy number, inertial parameters, Prandtl number, and geometric parameters on heat transfer and fluid flow were considered. The Darcy number was shown to have a profound effect on the Nusselt number and there was an optimum Darcy number for which the Nusselt number was maximum. When the Reynolds number was increased, the Nusselt number was also shown to increase. The increase in inertial effects was shown to enhance the blowing effect which is known to occur in porous blocks. This blowing effect occurs because the stream-wise flow through the porous blocks is retarded. However, this retardation is compensated for by an increase in the velocity normal to the stream-wise flow in the porous media. The blowing effect was also shown to increase the recirculation found on the right top corners of the porous blocks. The most visible and distinct effects on the Nusselt number were documented when the Prandtl number was increased from 0.7 to 100. When the height of the blocks was decreased the distortion in the streamlines became less pronounced. An increase in the pitch was shown to result in the adjacent blocks becoming independent of each other's influence upstream.

Ould-Amer et al. [2] investigated the benefits of using porous inserts for cooling electronic chips in a two-dimensional channel with laminar flow by making use of a control volume approach. The configuration for the study was similar to that of Huang and Vafai [1]. The difference being that porous substrates were placed between the heat generating blocks. Three heat generating blocks were considered for this study. The heat generating blocks simulated heat generation by the electronic chips. Lowering of temperatures on the side walls of the heat generating blocks was reported. Enhancement of cooling was obtained on the condition that the effective thermal conductivity of the porous medium should be much larger than the conductivity of the fluid. Increases of 50% in the Nusselt numbers were predicted and a subsequent lowering of maximum temperatures within the heat sources was reported.

Kim and Vafai [3] investigated the enhancement effects of a porous substrate on a flat plate using a numerical approach. The configuration for his investigation was that of a flat plate mounted by a porous substrate. This numerical study could also be classified as two-dimensional external flow problems involving porous media. A two-dimensional laminar flow was considered for this study; However, a finite volume based approach was used. The results of the investigation indicated that the use of porous media could lead to a reduction in frictional drag, and heat transfer enhancement or retardation.

Amiri et al. [4] conducted an experimental and numerical investigation on the effects of boundary conditions on non-Darcian heat transfer within porous media. A finite volume method was used to conduct the numerical investigation of the two-dimensional laminar flow in the packed bed porous media. A two-phase model equation for the transport was used. Both cases of constant wall temperature and constant wall heat flux boundary conditions were examined. Results showed that both constant wall temperature and constant wall heat flux result in heat transfer enhancement. Further, that the constant temperature wall case had an edge over the constant wall heat flux case.

Sung et al. [5] considered a two-dimensional laminar forced convection study in a parallel plate channel having a single porous block. The isolated heat source of uniform heat flux was located either under the porous block or on the channel wall directly opposite to it. Simulation experimentation using variations in the height and Darcy numbers concluded that it was not favorable to have porous blocks of larger height and low Darcy number in electronic cooling equipment. For one of the geometric arrangements that had the heat source located directly opposite the porous block on the other wall, it was demonstrated that as the Darcy number decreased it resulted in a decrease in the maximum wall temperature. The other geometric arrangement that had the heat source located directly below the porous block, demonstrated that as the Darcy number decreased it resulted in an increase in the maximum wall temperature. The study also established that both favorable and unfavorable conditions did exist when the height of the porous block was varied as well as the location of the heat source.

Although the numerical investigation of Webb and Ramadhyani [6] did not involve porous media, some of the conclusions are of importance to this research work and are therefore being included. A two-dimensional laminar flow in a rectangular channel with staggered internal ribs subjected to uniform heat flux was considered. The resulting serpentine flow that developed was shown to produce large vorticities downstream of the ribs. This behavior was more pronounced for ribs taller than one-fourth the height of the channel and at higher Reynolds numbers (400 – 2000 based on the hydraulic diameter).

For low Reynolds numbers ($\leq$ 400) and for Prandtl number 0.7 (air), heat transfer enhancement was found to be poor. In fact for this range the ratio of the Nusselt number for this study to that for a parallel plate channel was found to be less than, or around one. This poor heat enhancement could; however, be improved considerably if a larger Prandtl number fluid such as water (Pr = 7.0) were to be used.

In the current study a two-dimensional fluid flow was considered in a horizontal rectangular parallel plate channel with staggered internal porous baffles subjected to uniform heat flux heating. The configuration of this study was similar to an investigation conducted by Huang and Vafai [1]. Some of the differences between the Haung and Vafai [1] investigation and the current investigation are; this current study considered porous baffles while in the published work of Huang and Vafai [1] porous blocks were used. The current study considered a uniform heat flux boundary condition for the parallel plates. The published work [1] considered isothermal boundary conditions for the parallel plates of the channel. The current study considered sixteen porous baffles positioned alternately on the top and bottom walls of the channel. The published work [1] considered four porous blocks attached to the bottom wall of the channel. In this study the Reynolds number (based on channel height) varied from 50 to 200, while in the published work it varied from 750 – 1500. The current study also investigated in depth the effect of porous baffles on friction factor. In the current study, the pumping power was also computed to provide a realistic expectation of the pressure drop that is encountered when dealing with porous baffles in parallel plate channels. The current study was restricted to laminar flows (Reynolds numbers below 400 based on hydraulic diameter). This was done because of the complexity of the serpentine flow as it is unlikely that the flow could be deemed to be laminar for Reynolds numbers that are appreciably larger than 400. In addition, the developed code became unstable for Reynolds numbers greater than 400 for a channel with sixteen porous baffles. In this study, porous baffles of varying permeability and geometry were considered and the effect of such variation on heat transfer was analyzed. The heat transfer results have been presented in terms of the average Nusselt number for each module. The result of the current two-dimensional steady state laminar flow simulation was then compared with other similar published works for the purpose of validation.

In this study, consideration was given to a heat transfer enhancement in a two-dimensional laminar flow in a parallel plate channel in the presence of sixteen wall mounted porous baffles positioned alternately on the top and bottom walls of the channel whose walls were subjected to uniform wall heat flux condition. To provide insight into the transport process, that takes place in the porous media, the derivation of the governing equations in light of volume averaging has been carried out in Chapter 3.

CHAPTER III

MODEL DEVELOPMENT

3.1 Volume Averaging

The complexity in dealing with porous media restricts us from calculating the detailed velocity profile inside each pore; this is so even with modern computing facilities. It is not practical as it is extremely cost prohibitive to do a detailed microscopic investigation of heat transfer and fluid flow in porous media. So it has become common practice to use a macroscopic approach for solving heat transfer problems in porous media. In the macroscopic model the strategy is to average or smooth out the local complexities of the actual flow and temperature fields. Velocity, pressure, and temperature fields can be obtained, by volume averaging techniques.

A porous media is said to be unsaturated for flows involving more than one fluid flowing through the porous matrix. However, a homogenous porous media is that comprised of only one fluid and the porous matrix itself is called a saturated porous media. Now consider a control volume V in fluid saturated porous media as shown in Figure 3.1. The characteristic length of such a control volume would be of the order $V^{\frac{1}{3}}$ (L1). The characteristic length should be greater than the characteristic length of the porous structure d_p (pore diameter). This characteristic length needs to be larger to provide for a reasonable localized spatial average. However the characteristic length of the control volume has to be several orders smaller than the macroscopic characteristic length such as the height or length (L) of a channel. Under this conditional constraint

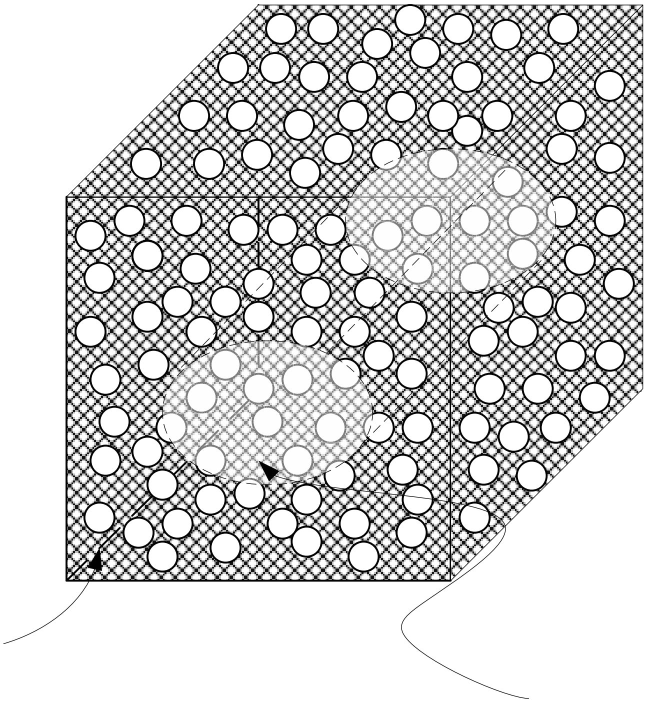

Fig. 3.1 Macroscopic view of a porous media element

L >> L1 >> d_p the local Darcian velocity $\langle \boldsymbol{u} \rangle$ vector ***u*** can be defined as:

$$\langle \boldsymbol{u} \rangle = \frac{1}{V} \int_{V_f} \boldsymbol{u} dV \tag{3.1}$$

Where V_f is the volume that is occupied by the fluid in the control volume. Some authors such as Vafai and Tien [7] use another method of volume averaging that is known as the intrinsic volume averaging and is defined as:

$$\langle \boldsymbol{u} \rangle^f = \frac{1}{V_f} \int_{V_f} \boldsymbol{u} dV \tag{3.2}$$

Where V_f is the volume that is occupied by the fluid in the control volume, $\langle \boldsymbol{u} \rangle^f$ is better known by the name "pore velocity". From these two definitions of volume averaging it can be ascertained that:

$$\langle \boldsymbol{u} \rangle^f = \frac{V}{V_f}\frac{1}{V}\int_{V_f} \boldsymbol{u}dV = \frac{V}{V_f}\langle \boldsymbol{u} \rangle \tag{3.3}$$

At this point it is important to define the term called porosity. Porosity is defined as the ratio of the volume of the fluid occupied in a control volume to the volume of the control volume itself. Using this definition of porosity the following expression can be obtained:

$$\varepsilon = \frac{V_f}{V} \tag{3.4}$$

By using Equations 3.3 and 3.4 it follows that the pore velocity $\langle \boldsymbol{u} \rangle^f$ can be related to the Darcian velocity $\langle \boldsymbol{u} \rangle$, which is sometimes known as the "seepage velocity", by the following expression:

$$\langle \boldsymbol{u} \rangle^f = \frac{1}{\varepsilon}\langle \boldsymbol{u} \rangle \tag{3.5}$$

3.2 Volume Averaged Navier Stokes Equations

Before deriving the volume averaged Navier-Stokes equation it is important to make assumptions that are used later to simplify the equation. The fundamental assumptions that have to be made are, the porous matrix is isotropic, homogenous, and non-deformable. Simply meaning that properties of the transport are not a function of the coordinate system, nor is the porous matrix susceptible to expansion, contraction, or flexure. At this point, it is important to establish some basic operations that will be used in deriving the Forchheimer-extended Darcy equation. In porous media research, the Forchheimer-extended Darcy model is preferred because Darcy's law does not adequately reflect the fluid flow through the porous media, this in turn affects the proper determination of the actual heat transfer that takes place. This occurs because Darcy's law does not take into account solid boundaries and it neglects the inertial effects. These shortcomings in Darcy's model become more pronounced near the solid boundary and when the porosity of the porous medium is high. The intrinsic average of a product "ab" can be obtained by methods analogous to the ones used in the formulation of the well known Reynolds averaging procedure in the study of turbulence flow:

$$\langle ab\rangle^f = \langle a\rangle^f \langle b\rangle^f + \langle a'b'\rangle^f \tag{3.6}$$

where prime in a' and b' represents the fluctuating components. The fluctuating component of "a" is related to the intrinsic average $\langle a\rangle^f$ by the following relationship:

$$a = \langle a\rangle^f + a' \tag{3.7}$$

Using Equations 3.5 and 3.6 the following equation can be deduced:

$$\langle ab\rangle = \frac{1}{\varepsilon}\langle a\rangle\langle b\rangle + \langle a'b'\rangle \tag{3.8}$$

The Leibnitz rule can be used to produce another analogy:

$$\langle \nabla a\rangle = \nabla\langle a\rangle + \frac{1}{V}\int_{A_{interface}} a d\boldsymbol{A} \tag{3.9}$$

where, dA is the vector normal, pointing outward from the fluid side to the solid side, and $A_{interface}$ is the surface area between the solid and fluid. Now, first taking the volume average of the continuity equation and using Equation 3.9 it can be shown that:

$$\langle \nabla.\boldsymbol{u} \rangle = \nabla.\langle \boldsymbol{u} \rangle + \frac{1}{V} \int_{A_{interface}} \boldsymbol{u}.d\boldsymbol{A} = 0 \tag{3.10}$$

The surface integral taken at the interface of the control volume should yield zero since the fluid cannot flow through the solid walls. Therefore:

$$\nabla.\langle \boldsymbol{u} \rangle = 0 \tag{3.11}$$

The volume averaged form of the Navier-Stokes equations is:

$$\langle \nabla.(\rho \boldsymbol{u}\boldsymbol{u}) \rangle = -\langle \nabla P \rangle + \langle \nabla.\tilde{\boldsymbol{\tau}} \rangle \tag{3.12}$$

In Equation 3.12 the stress tensor ($\tilde{\boldsymbol{\tau}}$) for Newtonian fluids can also be written as $(\nabla \mu \boldsymbol{u}) + (\nabla \mu \boldsymbol{u})^T + \lambda \tilde{\boldsymbol{I}} \nabla.\boldsymbol{u}$. Now to simplify Equation 3.12 by making use of Equations 3.8, 3.9, and 3.11:

$$\begin{aligned} \frac{\rho}{\varepsilon} \langle \boldsymbol{u} \rangle . \nabla \langle \boldsymbol{u} \rangle + \rho \nabla \langle \boldsymbol{u}'\boldsymbol{u}' \rangle = -\nabla \langle P \rangle - \frac{1}{V} \int_{A_{interface}} P d\boldsymbol{A} + \nabla.\left\langle \left[(\nabla \mu \boldsymbol{u}) + (\nabla \mu \boldsymbol{u})^T + \lambda \tilde{\boldsymbol{I}} \nabla.\boldsymbol{u} \right] \right\rangle \\ + \frac{1}{V} \int_{A_{interface}} \tilde{\boldsymbol{\tau}} d\boldsymbol{A} \end{aligned} \tag{3.13}$$

Using the same approach as Equation 3.3 it can be shown to be:

$$\langle P \rangle^f = \frac{1}{\varepsilon} \langle P \rangle \tag{3.14}$$

By making an assumption that the porosity ε is constant and by substituting Equation 3.14 in 3.13, and dividing the whole equation by ε we can obtain:

$$\frac{\rho}{\varepsilon^2}\langle \boldsymbol{u}\rangle.\nabla\langle \boldsymbol{u}\rangle = -\nabla\langle P\rangle^f + \frac{\mu}{\varepsilon}\nabla^2\langle \boldsymbol{u}\rangle + \boldsymbol{r} \tag{3.15}$$

Where **r** is the apparent body force vector given by:

$$\boldsymbol{r} = \frac{\rho}{\varepsilon}\nabla\langle \boldsymbol{u}'\boldsymbol{u}'\rangle - \frac{1}{V_f}\int_{A_{interface}} PdA \quad + \frac{1}{V_f}\int_{A_{interface}} \tilde{\boldsymbol{\tau}}dA \tag{3.16}$$

Another way to view **r** is to think of it as a resistance that is encountered as the fluid flows through the porous media. Vafai and Tien [7] have shown by theoretical consideration **r** to be:

$$\boldsymbol{r} = -\frac{\mu}{K}\langle \boldsymbol{u}\rangle - \frac{\rho F}{\sqrt{K}}\left|\langle \boldsymbol{u}\rangle\right|\langle \boldsymbol{u}\rangle \tag{3.17}$$

Where ρ is the fluid density, K is the permeability of the porous medium, and F is the inertial coefficient that is better known as the Forchheimer constant. Substituting Equation 3.17 in 3.15 gives the macroscopic equation governing the steady flow in a porous medium.

$$\frac{\rho}{\varepsilon^2}\langle \boldsymbol{u}\rangle.\nabla\langle \boldsymbol{u}\rangle = -\nabla\langle P\rangle^f + \frac{\mu}{\varepsilon}\nabla^2\langle \boldsymbol{u}\rangle - \frac{\mu}{K}\langle \boldsymbol{u}\rangle - \frac{\rho F}{\sqrt{K}}\left|\langle \boldsymbol{u}\rangle\right|\langle \boldsymbol{u}\rangle \tag{3.18}$$

3.3 Volume Averaged Energy Equation

Before deriving the volume averaged energy equation it is important to make assumptions that are used later to simplify the equation. The fundamental assumptions that have to be made are, there is no internal heat generation within the porous matrix, the effects of thermal radiation are assumed negligible, and the viscous dissipation is negligible. The volume-averaged form of the energy equation for the fluid can be written in the form:

$$\left\langle \nabla.(\rho_f c_{pf} T\boldsymbol{u}) \right\rangle = \left\langle \nabla.(k_f \nabla T) \right\rangle \tag{3.19}$$

Now to simplify Equation 3.19 by making use of Equation 3.9.

$$\nabla.\left\langle (\rho_f c_{pf} T\boldsymbol{u}) \right\rangle + \frac{1}{V} \int\limits_{A_{interface}} (\rho_f c_{pf} T\boldsymbol{u}) d\boldsymbol{A} = \nabla.\left\langle (k_f \nabla T) \right\rangle + \frac{1}{V} \int\limits_{A_{interface}} (k_f \nabla T) d\boldsymbol{A} \tag{3.20}$$

The second term on the left-hand side of the equation surface integral, taken at the interface of the control volume, should yield zero since an assumption that there is no internal heat generation has been made; therefore:

$$\nabla.\left\langle (\rho_f c_{pf} T\boldsymbol{u}) \right\rangle = \nabla.\left\langle (k_f \nabla T) \right\rangle + \frac{1}{V} \int\limits_{A_{interface}} (k_f \nabla T) d\boldsymbol{A} \tag{3.21}$$

Again making use of Equations 3.8 and 3.9, Equation 3.21 becomes:

$$\begin{aligned} \nabla.\left[\frac{\rho_f c_{pf}}{\varepsilon} \langle T \rangle \langle \boldsymbol{u} \rangle + \rho_f c_{pf} \langle T'\boldsymbol{u}' \rangle \right] &= \nabla.\left[(k_f \nabla \langle T \rangle) + \frac{1}{V} \int\limits_{A_{interface}} (k_f T) d\boldsymbol{A} \right] \\ &\quad + \frac{1}{V} \int\limits_{A_{interface}} (k_f \nabla T) d\boldsymbol{A} \end{aligned} \tag{3.22}$$

Using a similar form of Equation 3.5 for T it can be shown that Equation 3.22 becomes:

$$\begin{aligned} \nabla.\left[\rho_f c_{pf} \langle T \rangle^f \langle \boldsymbol{u} \rangle \right] &= \nabla.\left[(k_f \nabla \varepsilon \langle T \rangle^f) + \frac{1}{V} \int\limits_{A_{interface}} (k_f T) d\boldsymbol{A} - \rho_f c_{pf} \langle T'\boldsymbol{u}' \rangle \right] \\ &\quad + \frac{1}{V} \int\limits_{A_{interface}} (k_f \nabla T) d\boldsymbol{A} \end{aligned} \tag{3.23}$$

The volume-averaged form of the energy equation for the porous matrix that is a solid can be written in the form:

$$\left\langle \nabla.(k_s \nabla T) \right\rangle = 0 \tag{3.24}$$

When deriving the energy equation for the fluid phase the unit vector normal dA, pointed outward from the fluid phase to the porous matrix (solid phase). However, when the area integral is carried out it should be noted that the unit normal now points in the opposite direction this is the reason why the negative sign appears in the next equation:

$$\nabla.\left[\left(k_s \nabla \langle T \rangle \right) - \frac{1}{V} \int_{A_{interface}} \left(k_s T \right) d\boldsymbol{A} \right] - \frac{1}{V} \int_{A_{interface}} \left(k_s \nabla T \right) d\boldsymbol{A} = 0 \tag{3.25}$$

The continuity of heat flux at the interface between the solid-fluid has to be matched at the interface, since there should not be a jump in the heat flux at the interface. Using this condition it is possible to obtain the following equation:

$$-k_s \nabla T \Big|_{solid\ side\ of\ interface} = -k_f \nabla T \Big|_{fluid\ side\ of\ interface} \tag{3.26}$$

Now substituting Equation 3.26 in Equation 3.25 to get:

$$\nabla.\left[\left(k_s \nabla \langle T \rangle \right) - \frac{1}{V} \int_{A_{interface}} \left(k_s T \right) d\boldsymbol{A} \right] - \frac{1}{V} \int_{A_{interface}} \left(k_f \nabla T \right) d\boldsymbol{A} = 0 \tag{3.27}$$

At this point, analogous to Equation 3.2, it is important to define the term solid temperature intrinsic volume average as follows:

$$\langle T \rangle^s = \frac{1}{V_s} \int_{V_f} T dV = \frac{1}{V - V_f} \int_{V_f} T dV = \frac{1}{(1-\varepsilon)} \frac{1}{V} \int_{V_f} T dV = \frac{\langle T \rangle}{(1-\varepsilon)} \tag{3.28}$$

Using the relation in Equation 3.28 to simplify Equation 3.27 to get:

$$\nabla.\left[\left(k_s \nabla \left((1-\varepsilon) \langle T \rangle^s \right) \right) - \frac{1}{V} \int_{A_{interface}} (k_s T) d\boldsymbol{A} \right] - \frac{1}{V} \int_{A_{interface}} (k_f \nabla T) d\boldsymbol{A} = 0 \tag{3.29}$$

Now assuming the fluid and the solid porous matrix are in thermal equilibrium:

$$\langle T\rangle^f = \langle T\rangle^s \tag{3.30}$$

This assumption is valid for most cases except in highly conductive solid porous matrix. Substituting Equation 3.30 in Equation 3.29, then adding the resultant equation, to Equation 3.23 to obtain:

$$\begin{aligned}\nabla.\left[\rho_f c_{pf}\langle T\rangle^f\langle \boldsymbol{u}\rangle\right] = \nabla.&\left[\left(k_f\varepsilon + k_s(1-\varepsilon)\right)\nabla\langle T\rangle^f + \frac{1}{V}\int_{A_{interface}}\left(k_f - k_s\right)Td\boldsymbol{A}\right]\\ &-\nabla.\left[\rho_f c_{pf}\langle T'\boldsymbol{u}'\rangle\right]\end{aligned} \tag{3.31}$$

The term $\nabla.\left[\left(k_f\varepsilon + k_s(1-\varepsilon)\right)\nabla\langle T\rangle^f + \frac{1}{V}\int_{A_{interface}}\left(k_f - k_s\right)Td\boldsymbol{A}\right]$ on the right side of Equation 3.31 is called molecular diffusion and can be modeled as:

$$\nabla.\left[\left(k_f\varepsilon + k_s(1-\varepsilon)\right)\nabla\langle T\rangle^f + \frac{1}{V}\int_{A_{interface}}\left(k_f - k_s\right)Td\boldsymbol{A}\right] = -k_{effective}\nabla.\langle T\rangle^f \tag{3.32}$$

The second term in Equation 3.32 is called the “tortuosity” term. The tortuosity is supposed to account for the thermal diffusion due to the microscopic structure of the porous matrix. This term disappears if the $\left(k_f - k_s\right)T$ is constant over the interface. Using an analogy similar to that of turbulent heat flux the term $\nabla.\left[\rho_f c_{pf}\langle T'\boldsymbol{u}'\rangle\right]$ can be modeled as:

$$\nabla.\left[\rho_f c_{pf}\langle T'\boldsymbol{u}'\rangle\right] = -k_{dispersion}\nabla\langle T\rangle^f \tag{3.33}$$

As stated in the assumptions before commencing this derivation, that the dispersion effects can be neglected, this assumption holds true for laminar flows. Then using this

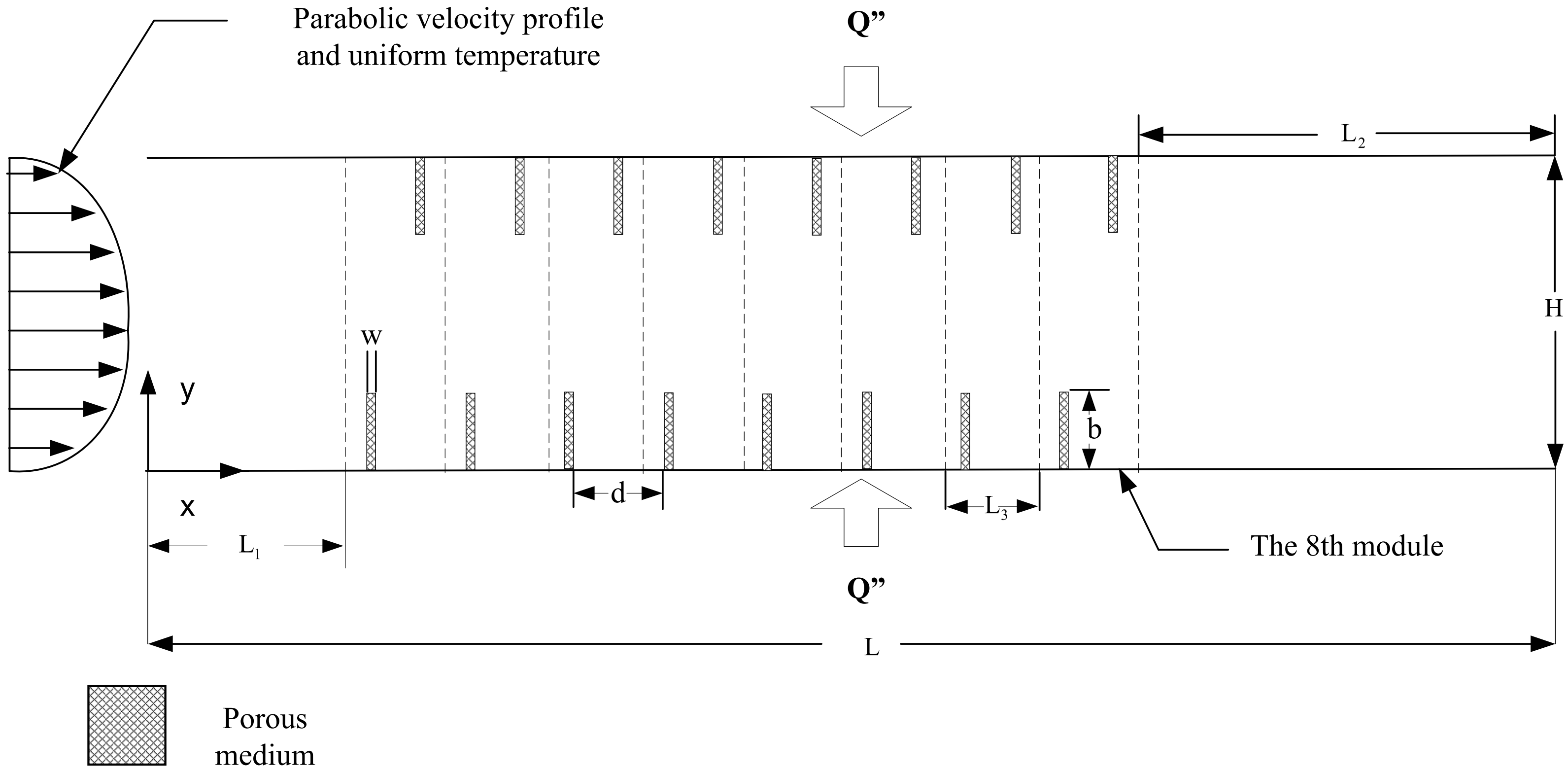

Fig. 3.2 Geometry

assumption and Equation 3.32 to simplify Equation 3.31, and thus obtain the volume averaged temperature equation as:

$$\nabla.\left[\rho_f c_{pf} \langle T \rangle^f \langle \boldsymbol{u} \rangle\right] = -k_{effective} \nabla.\langle T \rangle^f \qquad (3.34)$$

3.4 Geometric Configuration and Boundary Conditions

The Figure 3.2 shows the geometric configuration for the two-dimensional parallel plate channel with sixteen porous baffles in a staggered arrangement with a uniform heat flux heating applied to the top and bottom walls. When studying the configuration in Figure 3.2 the following have to be borne in mind. The spacing between two adjacent baffles is d, which can be varied. At the inlet of the channel, a parabolic velocity profile $u(y) = 6u_o \, {}^{y}\!/_{H}\left(1 - {}^{y}\!/_{H}\right)$ was prescribed for the velocity field; while a uniform temperature profile T_o was used for the temperature solution. The entry length (L_1) of the channel was fixed at six times the height of the channel (H). Henceforth, the region of the channel from the channel entrance up to the entrance of the first module entry length encompassing the entry length (L_1) (see Figure 3.2) shall be referred to as the “entry module”. At the exit the natural conditions $\frac{\partial u}{\partial x} = \frac{\partial v}{\partial x} = 0$ were applied for the velocity field; while the axial diffusion was set to a constant for the temperature solution. The exit length was set to twelve times the height of the channel (H), and was assumed to be long enough so as not to have any elliptic effects at the exit. Henceforth, the region of the channel beginning immediately after the eighth module up to the exit of the channel encompassing the entry length (L_2) (see Figure 3.2), shall be referred to as the "exit module". The upper and lower walls of the channel were impervious ($u = 0$, $v = 0$) to the flowing fluid while a uniform flux heating source ($\dot{q}'' = constant$) was prescribed at theses impervious boundaries. The width of the porous baffles (w) was varied and the height of the porous baffles (b) was held constant at one-third the channel height. The parallel channel had eight identical modules. The length of the channel (L) was calculated by adding the entry length, the eight module lengths, and the exit length of the channel. The length of each module L_3 was equal to $2\times(\mathrm{w+d})$. Table 3.1 lists a summary of the boundary conditions that were considered for this study:

Table 3.1 Boundary conditions

Left Boundary (Channel Entrance)	Right Boundary (Fully Developed)	Upper Boundary (Top Wall)	Lower Boundary (Bottom Wall)
$u(y) = 6u_o \dfrac{y}{H}\left(1 - \dfrac{y}{H}\right)$	$\dfrac{\partial u}{\partial x} = 0$	$u = 0$	$u = 0$
$v = 0$	$\dfrac{\partial v}{\partial x} = 0$	$v = 0$	$v = 0$
$T = T_o$	$\dfrac{\partial T}{\partial x} = \text{constant} \neq 0$	$\dot{q}'' = k\dfrac{\partial T}{\partial y}$	$\dot{q}'' = -k\dfrac{\partial T}{\partial y}$

3.5 The Governing Independent Parameters Influencing Fluid Flow and Heat Transfer

In this study there were several independent parameters that influenced the fluid flow and heat transfer in porous media. However, for the sake of brevity not all of the parameters were varied. The main governing parameters are listed as follows:

The first parameter was the Reynolds number (Re); it was based on the hydraulic diameter of the parallel plate channel. To ensure that the flow was truly laminar Reynolds numbers of 100, 200, 300, and 400 were considered.

The second parameter was the Darcy number (Da); it was based on the permeability of the porous medium (K) that was given in Kim et al. [8]. Kim et al. [8] listed three permeability values for porous aluminum foams, they were K = 1.04E-7 m^2, 0.76E-7 m^2, and 0.51e-7 m^2. From this the Darcy number was calculated by using the relationship between the Darcy number (Da) and the permeability of a porous medium (K) which is $\mathrm{Da}={}^{\mathrm{K}}\!/_{\mathrm{H}^2}$. Therefore, the Darcy numbers that were considered are Da = 8.783E-6, 1.309E-5, and 1.791E-5.

The third parameter was the Prandtl number (Pr); since, air flow was only considered for this study the Prandtl was held constant at 0.7 for the entire study.

The fourth parameter was the ratio of the height of the channel to the baffle thickness ($\mathrm{W}^*={}^{\mathrm{H}}\!/_{\mathrm{W}}$). For this study porous baffles of three different thicknesses (W^* = 4, 6, and 12) were considered, W^* = 12 being the thinnest baffle and W^* = 4 being the thickest baffle.

The fifth parameter was the non-dimensional baffle spacing ($D^* = d/w$) this is the ratio of the baffle spacing (d) between two consecutive baffles and the baffle thickness (w). In this study three different baffle spacings (d) were considered. The non-dimensional baffle spacing (D^*) corresponding to these three spacings were 11, 13, and 15.

The sixth parameter was the non-dimensional baffle height ($B^* = b/H$) this is the ratio of height of the porous baffle (b) to the height of the channel (H). For this study, the non-dimensional height (B^*) was held constant at 1/3.

The seventh parameter was the thermal conductivity ratio $\left(K^* = k_e/k_f\right)$. This is the ratio of the effective thermal conductivity of the porous matrix k_e to the thermal conductivity k_f of the fluid (air). In this study, three different thermal conductivity ratios of 1, 10, and 100 were considered. Kelkar [9] investigated heat transfer problems involving large differences in the thermal conductivities. In that it was conclusively demonstrated that poor convergence rates are associated in problems which have large differences in thermal conductivities. This phenomenon was also experienced in the current research; therefore, the largest thermal conductivity ratio was capped at 100. In addition, Table 3.2 lists the geometric, physical, and non-dimensional parameters used in this study:

Table 3.2 Parametric range

Re = 100, 200, 300, and 400	H = 7.620E-2 m	Pr = 0.7
$\mu_f = \mu_p$ = 1.843E-5 $\mathrm{N.s}/\mathrm{m}^2$	$\rho_f = \rho_p$ =1.177 Kg/m^3	$\dot{q}''$ = 10 W/m^2
$c_{pf} = c_{pp}$ = 1.005E+3 $\mathrm{J}/(\mathrm{Kg \cdot K})$	L = 2.5908 m (at least)	T_o = 37 C^{o}
u_o (to be calculated from Re)	K* = 1, 10, and 100	ε_p = 0.92
Da$_p$ = 8.783E-6, 1.309E-5, and 1.791E-5	Da$_f$ = 1.722E+62	ε_f = 1
$\mathrm{k_f}$ (to be calculated from Pr)	$\mathrm{F_f}$ = 1E-30	$\mathrm{F_p}$ = 0.55
W* = 4, 6, and 12	D* = 11, 13, and 15	B* = $1/3$

In Table 3.2 it should be noted that the terms $\mathrm{Da_f}$ and $\mathrm{F_f}$, the Darcy number in the fluid and the Forchheimer coefficient, respectively, do not exist physically but have been used as a numerical approximation so as to help reduce the Brinkman-Forchheimer-extended Darcy equations to the Navier-Stokes set of equations. This approximation was used in order to treat the full computational domain as a single domain rather then as two separate domains (one domain for fluid and the other for the porous matrix).

CHAPTER IV

NUMERICAL PROCEDURE

The closed form solutions for heat transfer and fluid flow in a two-dimensional parallel plate channel are limited due to the non-linear nature of the governing equations, warranting experimentation or numerical solutions. However, it is not always economically viable to conduct experiments for every single test case that may have an industrial use. Therefore, solutions by numerical methods have been used to simulate such experimentation; one branch of numerical technique is the finite volume method which was developed to provide approximate but realistic solutions to complex problems, such as those involving porous media. Patankar and Spalding [10] proposed one such method called the Semi Implicit Method for Pressure-Linked Equations (SIMPLE), that has been useful in providing numerical solutions for complex heat transfer and fluid flow problems. In the SIMPLE finite volume method ascribed to Patankar and Spalding [10] the momentum equations are solved while, at the same time being coupled to the pressure field. This method is useful since it provides the flexibility to directly solve primitive variables such as velocities and pressure (U, V and P). This particular finite volume technique avoids defining stream function as an intermediate step for obtaining the numerical solution. The importance of this cannot be over emphasized when dealing with the numerical simulations in three-dimensions. This is why SIMPLE has become one of the standard tools for seeking numerical solutions. A finite volume method very similar to the SIMPLE algorithm called the Semi Implicit Method for Pressure-Linked Equations Consistent (SIMPLEC) was developed by Van

Doormal and Raithby [11] and this method has the additional benefit of faster convergence but comes with an additional computation cost. Now it is important to mention that porous media simulations make use of a very complicated source term, which needs to be linearized to provide numerical stability, the details of which will be documented later in this chapter. The non-linear source term slows down the convergence; therefore, the SIMPLEC algorithm was selected over the SIMPLE algorithm to speedup convergence. A FORTRAN code was developed to implement the SIMPLEC algorithm to solve the numerical problem of the current study.

4.1 Numerical Techniques

Essentially all numerical techniques used to solve the convection-diffusion equations can be broken down into three distinct components, the components being the formulation, the discretization, and the solution. Either a vorticity or primitive variables formulation can be adopted to help steer the course of the numerical technique. Once the formulation for the numerical scheme is set the next important step is to select a discretization method. There are several methods that can be used, the finite volume method, spectral method, finite element method, and the finite difference method just to name a few. The final step entails the solver i.e., exactly how the numerical computation is carried out to obtain the solution to the set of discretization equations that were obtained using one of the various discretization methods. Patankar and Spalding [10] developed a numerical technique called SIMPLE to solve the Navier-Stokes set of governing equations. SIMPLE uses primitive variables for its formulation, a finite volume method to develop the discretization equations, and the line-by-line method was used to solve a set of algebraic equations. The line-by-line method is a combination of Gauss-Seidel and the tri-diagonal matrix algorithm. The vorticity-based method has a disadvantage in that it cannot be easily extended to three-dimensional configurations. The vorticity based method also creates problems in implementing the no slip boundary conditions. While the primitive variables based methods are easily extendable to three-dimensions and have no problems in representing the no slip boundary conditions.

4.2 The Power Law Scheme

In the formulation of an acceptable solution for the one-dimensional convection-diffusion equation $\frac{\partial}{\partial x}\left[\rho u\phi - \Gamma\frac{\partial \phi}{\partial x}\right]=0$ and the continuity equation $\frac{\partial}{\partial x}\left(\rho u\right)=0$ several schemes are available to link the convection and diffusion terms in the convection-diffusion equation. The exact solution, being the exponential scheme, provides a mechanism for linking the convective and diffusive terms, however since the use of the exponent is a computationally expensive operation this method is not useful practically. Patankar [12] developed the power law scheme $A\left(|P|\right)=\left[\!\left[0,\left(1-0.1|P|\right)^5\right]\!\right]$ which better represents the curve fit solution of the exponential scheme. Details of the terms used in this scheme are described in Section 4.2. The power law scheme is the most accurate, and is a computationally reasonable scheme that is available to combine the diffusion and convection effects. Other schemes like the upwind scheme and the hybrid scheme have been developed, but are not as accurate as the power law scheme. For more details on the various schemes, coupling the convection and diffusion see Patankar [12].

4.3 The Discretization of the Two-Dimensional General Convection-Diffusion Equation

Consider the steady state two-dimensional general convection-diffusion equation as shown in Equation 4.1

$$\frac{\partial}{\partial x}\left[\rho u\phi-\Gamma\frac{\partial\phi}{\partial x}\right]+\frac{\partial}{\partial y}\left[\rho v\phi-\Gamma\frac{\partial\phi}{\partial y}\right]=S \tag{4.1}$$

Now, consider a unit control volume for the two-dimensional transport of property ϕ as shown in Figure 4.1. Where ϕ could represent U, V, or T i.e., the component of the velocity in the x-direction, the component of the velocity in the y-direction, and the temperature, respectively. When ϕ = 1, Equation 4.1 reduces to the continuity equation. At this instance using Equation 4.1 and carrying out an integration over the control volume $\Delta x\Delta y$ yields:

$$\int_s^n\int_w^e\frac{\partial}{\partial x}\left[\rho u\phi-\Gamma\frac{\partial\phi}{\partial x}\right]dxdy+\int_s^n\int_w^e\frac{\partial}{\partial y}\left[\rho v\phi-\Gamma\frac{\partial\phi}{\partial y}\right]dxdy=\int_s^n\int_w^e Sdxdy \tag{4.2}$$

Integrating once:

$$\left[\rho u\phi-\Gamma\frac{\partial\phi}{\partial x}\right]_w^e\Delta y+\left[\rho v\phi-\Gamma\frac{\partial\phi}{\partial y}\right]_s^n\Delta x=S\Delta x\Delta y \tag{4.3}$$

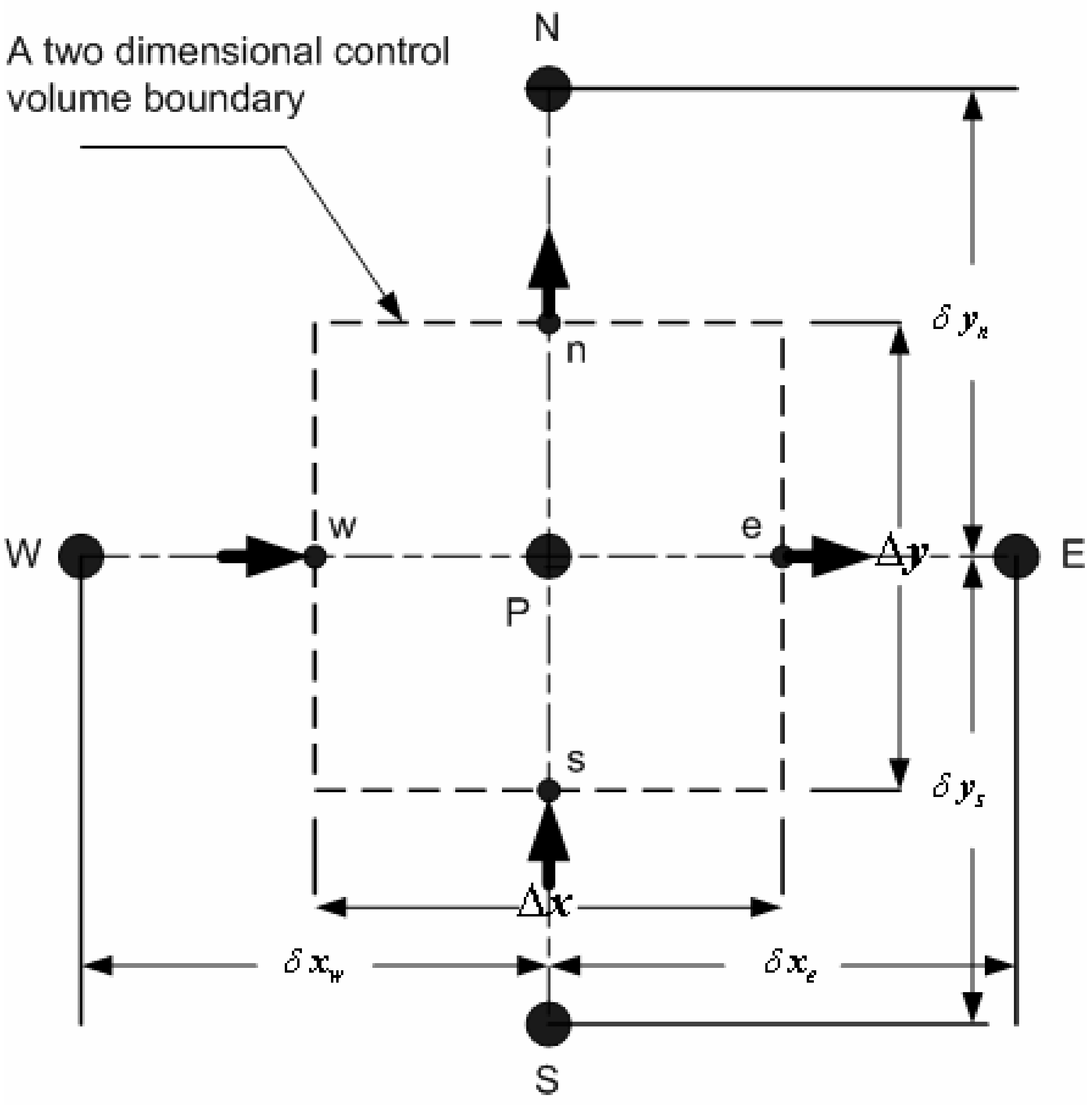

Fig. 4.1 A five node stencil for the integration of convection-diffusion transport equation

Assuming that the source term is linearized in the form of $S = S_C + S_P\phi$ and that it is being evaluated at the current location of the P node as shown in Figure 4.1. The source term needs to be linearized as shown by Patankar [12] because it benefits numerical stability. However, if incorrectly done or ignored it can prevent the solution process from ever converging and/or violate the Scarborough criteria. In the governing equations of porous media, there exist such source-terms that need to be linearized correctly to maintain the stability of the solution process. An additional condition is that the S_P term in the linearized source term mentioned earlier always needs to be negative Patankar [12]. Then by using Equation 4.3 and the linearized source term, it can be shown that the general convection-diffusion discretization equation takes the form:

$$a_P\phi_P = a_E\phi_E + a_W\phi_W + a_S\phi_S + a_N\phi_N + b \tag{4.4}$$

Where

$$a_W = D_w A\left(\left|P_w\right|\right) + [\![F_w, 0]\!] \tag{4.5}$$

$$a_E = D_e A\left(\left|P_e\right|\right) + [\![-F_e, 0]\!] \tag{4.6}$$

$$a_S = D_s A\left(\left|P_s\right|\right) + [\![F_s, 0]\!] \tag{4.7}$$

$$a_N = D_n A\left(\left|P_n\right|\right) + [\![-F_n, 0]\!] \tag{4.8}$$

$$a_P = a_W + a_E + a_S + a_N - S_P\Delta x\Delta y \tag{4.9}$$

$$b = S_C\Delta x\Delta y \tag{4.10}$$

$$F_w = \left(\rho u\right)_w \Delta y \quad F_e = \left(\rho u\right)_e \Delta y \quad F_s = \left(\rho v\right)_s \Delta x \quad F_n = \left(\rho v\right)_n \Delta x \tag{4.11}$$

$$D_w = \frac{\Gamma_w\Delta y}{\delta X_w} \quad D_e = \frac{\Gamma_e\Delta y}{\delta X_e} \quad D_s = \frac{\Gamma_s\Delta x}{\delta Y_s} \quad D_n = \frac{\Gamma_n\Delta x}{\delta Y_n} \tag{4.12}$$

$$P_w = \frac{F_w}{D_w} \quad P_e = \frac{F_e}{D_e} \quad P_s = \frac{F_s}{D_s} \quad P_n = \frac{F_n}{D_n} \tag{4.13}$$

$$A\left(|P|\right)=\left[\!\left[0,\left(1-0.1|P|\right)^5\right]\!\right] \tag{4.14}$$

Note the $\left[\!\left[a_1, a_2, a_3, a_4, \ldots\ldots\ldots\ldots\ldots, a_n\right]\!\right]$ is an operator that returns the largest number in the list of numbers represented by $a_1, a_2, a_3, a_4, \ldots\ldots\ldots\ldots\ldots, a_n$. In FORTRAN it is equivalent to $DMAX1\left(a_1, a_2, a_3, a_4, \ldots\ldots\ldots\ldots\ldots, a_n\right)$ when considering double precision.

4.4 Staggered Grid and the Discretized Porous Media Governing Equations

Patankar and Spalding [10] to deal with the instability that is prevalent in wavy pressure and velocity distributions adopted, the staggered grid system. In the staggered grid there are three different control volumes that are encountered. Two of these control volumes are displaced half a control volume in the x- and the y-direction of the third control volume which is called the scalar control volume. The first two control volumes being the U-velocity and the V-velocity control volumes. The staggered grid places the nodal points at the center of the control volumes. In the staggered grid, the control volumes are first positioned and then the centers of the control volumes are located. This way when a non-uniform grid is used the location of the control volume faces will not be located mid-way between two adjacent grid points. The advantage of the staggered grid is that it is robust.

Before beginning the discussion on discretization, it is best to recap all the governing equations derived in Chapter 3, the continuity equation, the momentum equations, and the energy equation are:

$$\frac{\partial u}{\partial x}+\frac{\partial u}{\partial y}=0 \tag{4.15}$$

$$\begin{aligned}\rho_p\left[u\frac{\partial u}{\partial x}+v\frac{\partial u}{\partial y}\right]=-\varepsilon^2\frac{\partial p}{\partial x}+\left[\frac{\partial}{\partial x}\left(\varepsilon\mu_p\frac{\partial u}{\partial x}\right)+\frac{\partial}{\partial y}\left(\varepsilon\mu_p\frac{\partial u}{\partial y}\right)\right]-\frac{\varepsilon^2\mu_p}{K}u\\ -\rho_p\frac{F\varepsilon^2}{\sqrt{K}}\left(\sqrt{u^2+v^2}\right)u\end{aligned} \tag{4.16}$$

$$\begin{aligned}\rho_p\left[u\frac{\partial v}{\partial x}+v\frac{\partial v}{\partial y}\right]=-\varepsilon^2\frac{\partial p}{\partial y}+\left[\frac{\partial}{\partial x}\left(\varepsilon\mu_p\frac{\partial v}{\partial x}\right)+\frac{\partial}{\partial y}\left(\varepsilon\mu_p\frac{\partial v}{\partial y}\right)\right]-\frac{\varepsilon^2\mu_p}{K}v\\ -\rho_p\frac{F\varepsilon^2}{\sqrt{K}}\left(\sqrt{u^2+v^2}\right)v\end{aligned} \tag{4.17}$$

$$\rho_p\left[u\frac{\partial T}{\partial x}+v\frac{\partial T}{\partial y}\right]=\left[\frac{\partial}{\partial x}\left(\frac{k_{effective}}{cp_p}\frac{\partial T}{\partial x}\right)+\frac{\partial}{\partial y}\left(\frac{k_{effective}}{cp_p}\frac{\partial T}{\partial y}\right)\right] \tag{4.18}$$

A close examination of Equation 4.16 with the general transport Equation 4.1 reveals that the $\Gamma=\varepsilon\mu$ and that $S=0-\left[\frac{\varepsilon_p{}^2\mu_p}{K}+\rho_p\frac{F\varepsilon_p{}^2}{\sqrt{K}}\sqrt{u_p{}^2+v_p{}^2}\right]u_p$ note the $-\varepsilon^2\frac{\partial p}{\partial x}$ term in Equation 4.16, has not been accounted for. It should not be included in the source term (S) but rather must be expressed as a separate term: $\varepsilon_e{}^2\Delta y\left(p_w-p_e\right)$. This change is done to provide a coupling mechanism for the pressure since the pressure field will also be calculated using the continuity equation (4.15). Using a similar approach as discussed for the x-momentum equation it can be shown for the y-momentum equation that $\Gamma=\varepsilon\mu$, $S_p=-\left[\frac{\varepsilon_p{}^2\mu_p}{K}+\rho_p\frac{F\varepsilon_p{}^2}{\sqrt{K}}\sqrt{u_p{}^2+v_p{}^2}\right]$ and that the $-\varepsilon^2\frac{\partial p}{\partial y}$ term can be expressed as $\varepsilon_n{}^2\Delta x\left(p_s-p_n\right)$. Finally, for the energy Equation (4.18) if a comparison is made with Equation 4.1 it reveals that $\Gamma = \frac{k_{effective}}{cp_p}$ and the source of S to be zero. After simplification, all three equations will yield the following three-discretization equations:

$$a_e^u u_e = a_E^u u_E + a_W^u u_W + a_S^u u_S + a_N^u u_N + \varepsilon_e{}^2 \Delta y \left(p_w - p_e \right) + b_e^u \tag{4.19}$$

$$a_n^v v_n = a_E^v v_E + a_W^v v_W + a_S^v v_S + a_N^v v_N + \varepsilon_n{}^2 \Delta x \left(p_s - p_n \right) + b_n^v \tag{4.20}$$

$$a_P^T T_P = a_E^T T_E + a_W^T T_W + a_S^T T_S + a_N^T T_N \tag{4.21}$$

4.5 The Velocity and Pressure Corrections

In the SIMPLE algorithm the velocities (U and V) and the pressure (P) are decomposed into a guessed value and a correction value denoted by the superscripts “ * ” and “ ′ ”, respectively. Using this decomposition it can be shown that:

$$u = u^* + u', \quad v = v^* + v', \quad p = p^* + p' \tag{4.22}$$

Now it is important to mention that the discretized form of the momentum equations, given in Equations 4.19 and 4.20, could be solved directly to yield the velocity fields if the correct pressure field was given. However, generally it is not possible to obtain the pressure field prior to solving the momentum equations, therefore a guessed pressure field is needed to solve the momentum equation but the resulting velocity fields from the guessed pressure fields will not satisfy the continuity equation, thus requiring an adjustment in the pressure field. If such a guessed pressure field (p^*) was used to solve the discretized momentum equations given (4.19) and (4.20) it would generate a guessed velocity field given by:

$$a_e^u u_e^* = a_E^u u_E^* + a_W^u u_W^* + a_S^u u_S^* + a_N^u u_N^* + \varepsilon_e{}^2 \Delta y \left(p_P^* - p_E^* \right) + b_e^u \tag{4.23}$$

$$a_n^v v_n^* = a_E^v v_E^* + a_W^v v_W^* + a_S^v v_S^* + a_N^v v_N^* + \varepsilon_n{}^2 \Delta x \left(p_P^* - p_N^* \right) + b_n^v \tag{4.24}$$

Now using Equation 4.22 and subtracting Equations 4.23 and 4.24 from 4.19 and 4.20, respectively we obtain:

$$a_e^u u_e' = \left[a_E^u u_E' + a_W^u u_W' + a_S^u u_S' + a_N^u u_N' \right] + \varepsilon_e{}^2 \Delta y \left(p_P' - p_E' \right) \tag{4.25}$$

$$a_n^v v_n' = \left[a_E^v v_E' + a_W^v v_W' + a_S^v v_S' + a_N^v v_N' \right] + \varepsilon_n{}^2 \Delta x \left(p_P' - p_N' \right) \tag{4.26}$$

Now dropping the terms inside the [ ] brackets to obtain the velocity correction equations for the SIMPLE algorithm:

$$u_e' = \frac{\varepsilon_e{}^2 \Delta y}{a_e^u} \left(p_P' - p_E' \right) \tag{4.27}$$

$$v_n' = \frac{\varepsilon_n{}^2 \Delta x}{a_n^v} \left(p_P' - p_N' \right) \tag{4.28}$$

The dropping of the terms inside the [ ] brackets does not invalidate the approximation for the velocity corrections given in Equations 4.27 and 4.28 because in the converged solution the guessed pressure field p^* will assume the actual pressure field. The momentum equations will be satisfied by the velocity fields that correspond to this pressure field. This also is the reason why the SIMPLE algorithm is defined as a semi-implicit method since the bracket terms are omitted. In the SIMPLE algorithm, because of the bracket terms being omitted, it is possible to obtain a large pressure correction based on a poorly guessed pressure field. This large pressure correction would in itself introduce instability in the numerical scheme; hence Patankar [12] suggested that the pressure equation should be under-relaxed. However in the SIMPLEC algorithm the under relaxed form of x- and y-momentum equations are used accordingly, Equations 4.19 and 4.20 can be rearranged as:

$$\frac{a_e^u}{\alpha_u} u_e = a_E^u u_E + a_W^u u_W + a_S^u u_S + a_N^u u_N + \varepsilon_e^2 \Delta y \left(p_P - p_E \right) + b_e^u + \left(\frac{1}{\alpha_u} - 1 \right) a_e^u u_e^o \tag{4.29}$$

$$\frac{a_n^v}{\alpha_v} v_n = a_E^v v_E + a_W^v v_W + a_S^v v_S + a_N^v v_N + \varepsilon_n^2 \Delta x \left(p_P - p_N \right) + b_n^v + \left(\frac{1}{\alpha_v} - 1 \right) a_n^v v_n^o \tag{4.30}$$

Now if a guessed pressure field (p^*) was used to solve the discretized momentum equations given in (4.29) and (4.30) it would generate a guessed velocity field given by:

$$\frac{a_e^u}{\alpha_u} u_e^* = a_E^u u_E^* + a_W^u u_W^* + a_S^u u_S^* + a_N^u u_N^* + \varepsilon_e^2 \Delta y \left(p_P^* - p_E^* \right) + b_e^u + \left(\frac{1}{\alpha_u} - 1 \right) a_e^u u_e^o \tag{4.31}$$

$$\frac{a_n^v}{\alpha_v} v_n^* = a_E^v v_E^* + a_W^v v_W^* + a_S^v v_S^* + a_N^v v_N^* + \varepsilon_n^2 \Delta x \left(p_P^* - p_N^* \right) + b_n^v + \left(\frac{1}{\alpha_v} - 1 \right) a_n^v v_n^o \tag{4.32}$$

Now using Equation 4.22 and subtracting Equations 4.29 and 4.30 from 4.31 and 4.32, respectively, to obtain:

$$\frac{a_e^u}{\alpha_u} u_e' = \left[a_E^u u_E' + a_W^u u_W' + a_S^u u_S' + a_N^u u_N' \right] + \varepsilon_e^2 \Delta y \left(p_P' - p_E' \right) \tag{4.33}$$

$$\frac{a_n^v}{\alpha_v} v_n' = \left[a_E^v v_E' + a_W^v v_W' + a_S^v v_S' + a_N^v v_N' \right] + \varepsilon_n^2 \Delta x \left(p_P' - p_N' \right) \tag{4.34}$$

Further subtracting the term $\sum a_{nb}^u u_e'$ from both sides of Equation 4.33 and the term $\sum a_{nb}^v v_n'$ from both sides of Equation 4.34. Where $\sum a_{nb}^u u_e'$ represents

$a_E^u u_e' + a_W^u u_e' + a_S^u u_e' + a_N^u u_e'$ and $\sum a_{nb}^v v_n'$ represents $a_E^v v_n' + a_W^v v_n' + a_S^v v_n' + a_N^v v_n'$ then it can be shown that:

$$\left(\frac{a_e^u}{\alpha_u} - \sum a_{nb}^u\right) u_e' = \sum a_{nb}^u \left(u_{nb}' - u_e'\right) + \varepsilon_e{}^2 \Delta y \left(p_e' - p_E'\right) \tag{4.35}$$

$$\left(\frac{a_n^v}{\alpha_v} - \sum a_{nb}^v\right) v_n' = \sum a_{nb}^v \left(v_{nb}' - v_n'\right) + \varepsilon_n{}^2 \Delta x \left(p_P' - p_N'\right) \tag{4.36}$$

Now neglecting the summation terms on the right hand side of Equations 4.35 and 4.36 and rearranging to obtain the velocity correction equations for the SIMPLEC algorithm given by:

$$u_e' = \frac{\varepsilon_e{}^2 \Delta y}{\left(\frac{a_e^u}{\alpha_u} - \sum a_{nb}^u\right)} \left(p_P' - p_E'\right) \tag{4.37}$$

$$v_n' = \frac{\varepsilon_n{}^2 \Delta x}{\left(\frac{a_n^v}{\alpha_v} - \sum a_{nb}^v\right)} \left(p_P' - p_N'\right) \tag{4.38}$$

Here it is important to note that the approximation that was made to obtain Equations 4.27 and 4.28 from 4.23 and 4.24 for the case of SIMPLE is inconsistent. However, the approximation made by dropping the summation terms on the right hand side of Equations 4.35 and 4.36 to obtain Equations 4.37 and 4.38 for the case of SIMPLEC is consistent. The advantage of using a consistent approximation for SIMPLEC results in a less costly computational process. Now using Equation 4.9 it can be shown that:

$$a_e^u = \sum a_{nb}^u - S_e \Delta x \Delta y, \qquad a_n^v = \sum a_{nb}^v - S_n \Delta x \Delta y \tag{4.39}$$

Now using the relations given in (4.39) and substituting them in Equations 4.37 and 4.38, to obtain the velocity correction equations for the SIMPLEC algorithm that was considered for this study and is given by:

$$u'_e = \frac{{\varepsilon_e}^2 \Delta y}{\left(\frac{1}{\alpha_u} - 1\right) a_e^u - S_e \Delta x \Delta y} \left(p'_P - p'_E\right) \tag{4.40}$$

$$v'_n = \frac{{\varepsilon_n}^2 \Delta x}{\left(\frac{1}{\alpha_v} - 1\right) a_n^v - S_n \Delta x \Delta y} \left(p'_P - p'_N\right) \tag{4.41}$$

4.6 The Pressure Correction Equation in SIMPLE

In the solution of the x- and y-momentum equation the most challenging aspect is extracting the pressure field solution from the continuity equation where, the pressure term does not even appear, unlike the momentum equation. For the SIMPLE algorithm making use of the continuity Equation 4.15 and integrating it over a control volume $\Delta x \Delta y$ yields:

$$\int_s^n \int_w^e \frac{\partial}{\partial x}[\rho u] dx dy + \int_s^n \int_w^e \frac{\partial}{\partial y}[\rho v] dx dy = 0 \tag{4.42}$$

Integrating once:

$$\rho u\Big|_w^e \Delta y + \rho v\Big|_s^n \Delta x = 0 \tag{4.43}$$

Now making use of the relationships for the velocity given in Equation 4.22, and Equations 4.27 and 4.28 to get:

$$u_e = u_e^* + \frac{\varepsilon_e^{\,2}\Delta y}{a_e^u}\left(p'_P - p'_E\right), \quad v_n = v_n^* + \frac{\varepsilon_n^{\,2}\Delta x}{a_n^v}\left(p'_P - p'_N\right) \tag{4.44}$$

Substituting relations given in (4.44) into Equation 4.43 to get:

$$\begin{aligned} &\frac{\rho_e.\varepsilon_e^{\,2}\Delta y}{a_e^u}\left(p'_P - p'_E\right)\Delta y - \frac{\rho_w.\varepsilon_w^{\,2}\Delta y}{a_w^u}\left(p'_W - p'_P\right)\Delta y + \\ &\frac{\rho_n.\varepsilon_n^{\,2}\Delta x}{a_n^v}\left(p'_P - p'_n\right)\Delta x - \frac{\rho_s.\varepsilon_s^{\,2}\Delta x}{a_s^v}\left(p'_S - p'_P\right)\Delta x + \\ &\left(\rho_e u_e^* - \rho_w u_w^*\right) - \left(\rho_n v_n^* - \rho_s v_s^*\right) = 0 \end{aligned} \tag{4.45}$$

Now rewriting Equation 4.45 to obtain the pressure correction equation:

$$a_P p'_P = a_E p'_E + a_W p'_W + a_S p'_S + a_N p'_N + b \tag{4.46}$$

Where:

$$\begin{aligned} &a_E = \rho_e d_e \Delta y, \quad a_W = \rho_w d_w \Delta y, \quad a_S = \rho_s d_s \Delta x, \\ &a_N = \rho_n d_n \Delta x, \quad a_P = a_E + a_W + a_S + a_N \\ &b = \left(\rho_w u_w^* - \rho_e u_e^*\right) + \left(\rho_s v_s^* - \rho_n v_n^*\right) \end{aligned} \tag{4.47}$$

$$d_e = \frac{\varepsilon_e^{\,2}\Delta y}{a_e^u}, \quad d_w = \frac{\varepsilon_w^{\,2}\Delta y}{a_w^u}, \quad d_s = \frac{\varepsilon_s^{\,2}\Delta x}{a_s^u}, \quad d_n = \frac{\varepsilon_n^{\,2}\Delta x}{a_n^u} \tag{4.48}$$

Note Equations 4.46-4.48 are the equations that would be used by the SIMPLE algorithm method. In SIMPLE the pressure relation given in Equation 4.22 would have to be modified to $p = p^* + \alpha_P p'$ i.e., it would have to be under-relaxed to keep the numerical process stable. In SIMPLEC the pressure correction equation would be given by Equation 4.46-4.48 but Equation 4.48 would have to be modified since pressure correction in SIMPLEC is not given by Equations 4.27 and 4.28 but rather by (4.40) and (4.41) therefore, for SIMPLEC Equation 4.48 would become:

$$
\begin{aligned}
d_e &= \frac{{\varepsilon_e}^2 \Delta y}{\left(\dfrac{1}{\alpha_u} - 1\right) a_e^u - S_e \Delta x \Delta y}, \quad d_w = \frac{{\varepsilon_w}^2 \Delta y}{\left(\dfrac{1}{\alpha_u} - 1\right) a_w^u - S_w \Delta x \Delta y}, \\
d_s &= \frac{{\varepsilon_s}^2 \Delta x}{\left(\dfrac{1}{\alpha_v} - 1\right) a_s^v - S_s \Delta x \Delta y}, \quad d_n = \frac{{\varepsilon_n}^2 \Delta x}{\left(\dfrac{1}{\alpha_v} - 1\right) a_n^v - S_n \Delta x \Delta y}
\end{aligned}
\tag{4.49}
$$

Also in SIMPLEC the pressure relationship given in Equation 4.22 does not need to be under-relaxed since the SIMPLEC method employs a consistent approximation when deriving the pressure correction equation.

4.7 The Interface Face Properties

In this chapter, no references have been made as to how the properties were determined at the location of the interface of the control volumes. In Section 3.5 a brief reference was made as to how the Darcy number and Forchheimer coefficient were set in the fluid and porous matrix regions. Now to elaborate further, in the calculation of the diffusive coefficients and the source term, it is necessary to have the properties defined at the interface of the control volumes for the diffusion coefficients and at the center of the control volume for the source terms. This poses a problem because of the way in which the staggered grid is arranged, even so Patankar [12] showed that reasonable estimates of the properties at the interface could be obtained by using the harmonic mean. In two-dimensional problems the harmonic mean concept is extended by using a weighted harmonic mean using the areas of the four neighboring nodes as weighing factors to calculate the effective property at the desired node by:

$$\frac{1}{\Gamma_{effective}} = \frac{1}{\sum(A_1 + A_2 + A_3 + A_4)}\left[\frac{A_1}{\Gamma_1} + \frac{A_2}{\Gamma_2} + \frac{A_3}{\Gamma_3} + \frac{A_4}{\Gamma_4}\right] \tag{4.50}$$

In this study all the properties were defined at the location of the p-pressure nodes, then by using Equation 4.50 or the one-dimensional harmonic mean the properties were calculated at the interface between the adjacent pressure control volumes. It is important to emphasize that the properties located at the fluid-porous interface were determined by using the harmonic mean and that at no point in this study were the governing equations altered to match the shear stress, the velocity gradients, or temperature gradients along the fluid-porous interface. For this study, use was made solely of the Brinkman-Forchheimer-extended Darcy equations for both the fluid and porous matrix regions. As stated in Table 3.2 a numerical approximation was made to eliminate the Darcy and Forchheimer terms from the governing equations for the fluid domain. This approximation allowed the full computational domain to be considered as a single domain. The use of such an approximation made it is necessary to find the effective properties at the fluid-porous interface.

4.8 Line-by-Line Method

In the solution process of the two-dimensional parallel plate channel flow with sixteen staggered porous baffles, a finite volume technique was used to provide reasonably approximate and realistic results. Finite volume numerical techniques for the solution of two-dimensional heat transfer and fluid flow problems invariably involves solving the general discretization Equation 4.4. This equation links the five nodal points (Figure 4.1) with each other. The equation represents just one node and its surrounding neighbors. In this two-dimensional case, a grid of size [a x b] (a rows and b columns) is considered it would mean that a x b discretization equations such as (4.4) would have to be solved. If direct numerical methods were invoked to solve the (a x b) number of equations directly it would be unwise because it would be extremely cost prohibitive. However, an alternate to this dilemma is that, a solution can still be obtained by using the Gauss-Seidel point-by-point method to obtain the desired solution.

The Gauss-Seidel point-by-point method is essentially an iterative method where all the P nodes (Figure 4.1) in the grid are updated by visiting them in a particular order. Each time a grid point is visited the transport property ϕ_P at that location is updated using Equation 4.4. The advantage of the Gauss-Seidel point-by-point method is that it is very cost effective when the demands on computer memory are of the utmost importance. However, this advantage comes with the penalty of slow convergence. In meteorological weather predictions, this penalty is unacceptable. The demands of such needs have resulted in better numerical methods.

A much faster and computationally cost effective procedure known as the line-by-line has been developed to solve the discretization equations for a group of points along the same row or column. This method of solving a group of nodes all at the same time is in essence a combination of the tri-diagonal matrix algorithm (TDMA) and the Gauss-Seidel method. The direct method (TDMA) being less expensive to compute as only a single row or column is considered. The advantage of the TDMA method is that the information from the boundary is brought immediately into the interior of the computational domain. This is particularly so because the differential equation that governs the heat transfer and fluid flow in the porous media for this study are elliptic.

4.9 Convergence Criteria

All numerical methods provide approximate solutions to the problems that were investigated using such techniques. For some problems exact analytical solutions exists. However, in numerical methods a convergence criterion has to be used to reach an acceptable solution. The selection of this criterion depends on the problem being solved if a severe restriction is placed on it; it is possible that in the process of computation the computational errors dominate the solution process resulting in divergence or possible blowup of the solution process. In this study it was found that if a severe constraint was placed on the pressure residual the solution process resulted in divergence. The convergence criteria used in this study was:

$$\overline{R}_u = \frac{\sum\left|a_e^u u_e - \sum a_{nb}^u u_{nb} - b_u - \varepsilon_e^2 A_e^u \left(p_P - p_E\right)\right|}{\sum\left|a_e^u u_e\right|} < 10^{-5} \tag{4.51}$$

$$\overline{R}_v = \frac{\sum\left|a_n^v v_n - \sum a_{nb}^v v_{nb} - b_v - \varepsilon_n^2 A_n^v \left(p_P - p_N\right)\right|}{\sum\left|a_n^v v_n\right|} < 10^{-5} \tag{4.52}$$

$$R_P = \sum\left|\rho\left(u_w - u_e\right) + \rho\left(v_s - v_n\right)\right| < 10^{-3} \tag{4.53}$$

$$R_T = \sum\left|a_p^T T_P - \sum a_{nb}^T T_{nb} - b_T\right| < 10^{-4} \tag{4.54}$$

The above criteria were used for all the parametric runs in this study.

CHAPTER V

VALIDATION AND GRID INDEPENDENCE

After having developed a computer code it was imperative that the code be tested for its ability to produce valid results. This validating process has to be done before the production runs are carried out. For validation, it was important to demonstrate that the developed code was capable of solving some benchmark problems in heat transfer and at the same time yield results within the acceptable limits of computational errors. For this validation purpose three different test cases were considered. After validating the code, grid independence was established.

5.1 Validation Test Case 1: Heat Transfer in a 2-D Rectangular Channel

For the first validation test a case of laminar flow and heat transfer in a 2-D rectangular channel subjected to uniform heat flux (UHF) boundary conditions was investigated. A uniform grid (102 x 42) was used for this test case. The Nusselt number was one of the parameters, that was used to compare the numerical solution, obtained by the test case, to the analytical solution that is available in a standard heat transfer textbook Mills [13].

Since, the current code was developed for simulations of flow and heat transfer in porous media, it was necessary to treat the whole computation domain as a single block of porous media that was impervious at the top and bottom walls. For this porous block the porosity ε was set to 1, the permeability K of the medium was set to 1E+60 and the Forchheimer coefficient was set to 1E-30. This constraint was imposed on the

Brinkman-Forchheimer-extended Darcy model equation in order to reduce it to the Navier-Strokes equation which governs the flow field for this test case. This approximation in turn serves as a limiting condition that establishes the soundness of the developed code. Table 5.1 shows the boundary conditions that were imposed on this first test case. At the exit the natural conditions $\partial u/\partial x = \partial v/\partial x = 0$ were applied for the velocity field; while the axial diffusion was set to a non-zero constant for the temperature field. The channel was assumed to be long enough so as not to have any elliptic effects at the exit. A uniform grid in both x and y (the axial and transverse coordinates) directions was used to obtain the numerical solution. In addition to the above, Table 5.2 lists the geometric, physical, and non-dimensional parameters used for this test case. In this test case the following parameters were investigated,

Table 5.1 Boundary conditions for validation Test Case 1 in: 2-D rectangular channel flow

Channel Entrance	Channel Exit	Top Wall	Bottom Wall
x = 0, $u = u_o$	x = L, $\partial u/\partial x = 0$	y = H, $u = 0$	y = 0, $u = 0$
x = 0, $v = 0$	x = L, $\partial v/\partial x = 0$	y = H, $v = 0$	y = 0, $v = 0$
x = 0, $T = T_o$	x = L, $\partial T/\partial x$ = constant ≠ 0	y = H, $\dot{q}'' = k\,\partial T/\partial y$	y = 0, $\dot{q}'' = -k\,\partial T/\partial y$

Table 5.2 Geometric, physical, and non-dimensional parameters for validation Test Case 1: 2-D rectangular channel flow

Re (Reynolds Number $\mathrm{Re} = \frac{\rho U_o H}{\mu}$)	400
Pr (Prandtl Number $\mathrm{Pr} = \frac{\mu c_p}{k}$)	0.7
L (Length of channel)	2.5908 m
H (Height of channel)	7.62E-2 m
ρ (Density of fluid)	1.177 $\frac{\mathrm{Kg}}{\mathrm{m}^3}$
μ (Dynamic viscosity)	1.843E-5 $\frac{\mathrm{N.s}}{\mathrm{m}^2}$
c_p (Specific heat at constant pressure)	1.005E+3 $\frac{\mathrm{J.Kg}}{\mathrm{K}}$
q constant uniform heat flux	10 $\frac{\mathrm{W}}{\mathrm{m}^2}$

1. The exit u-velocity should take a parabolic profile given by the second order polynomial

$$u(y) = 6u_o \frac{y}{H}\left(1 - \frac{y}{H}\right) \tag{5.1}$$

Where u_o is the uniform inlet velocity to the channel and y is the transverse coordinate. The location of the origin was fixed at the bottom left corner of the channel. The numerical u-velocity profiles, as a function of the y-coordinate at various cross sections have been plotted, along with the analytic u-velocity profile given by the parabolic polynomial (Equation 5.1) is represented in Figure 5.1. The analytic u-velocity profile has been included in this plot to serve as a comparison for the fully developed condition. The maximum relative absolute percentage error was found to be less than 1.25%.

2. Theory dictates that the v-velocity at the exit region should be zero, this is found to be true in the numerical sense as the maximum absolute v-velocity at the exit was found to be 9.21E-10. Though this value is not zero nevertheless it is small enough to be considered zero in comparison to magnitude of u-velocity encountered at the exit.
3. The streamlines plot Figure 5.2 was obtained by the use of the commercial software Tecplot v 8.0. The results illustrated by this plot confirm that the flow attained the fully developed velocity profile at the channel exit.
4. The Nusselt number at the channel exit for a thermally fully developed flow, between parallel plates subjected to constant UHF, is 8.235 [13]. Figure 5.3 illustrates the results that were obtained for this test case problem. At the entry region of the channel the Nusselt numbers were found to be large while progressively decaying to a asymptotic value that was found to be 8.254 for this test run, this value is found to be within 0.25% of the stated value in Mills [13]. The Nusselt number for both the bottom and top wall has been plotted to validate the symmetry of this test case which can be clearly established from Figure 5.3.

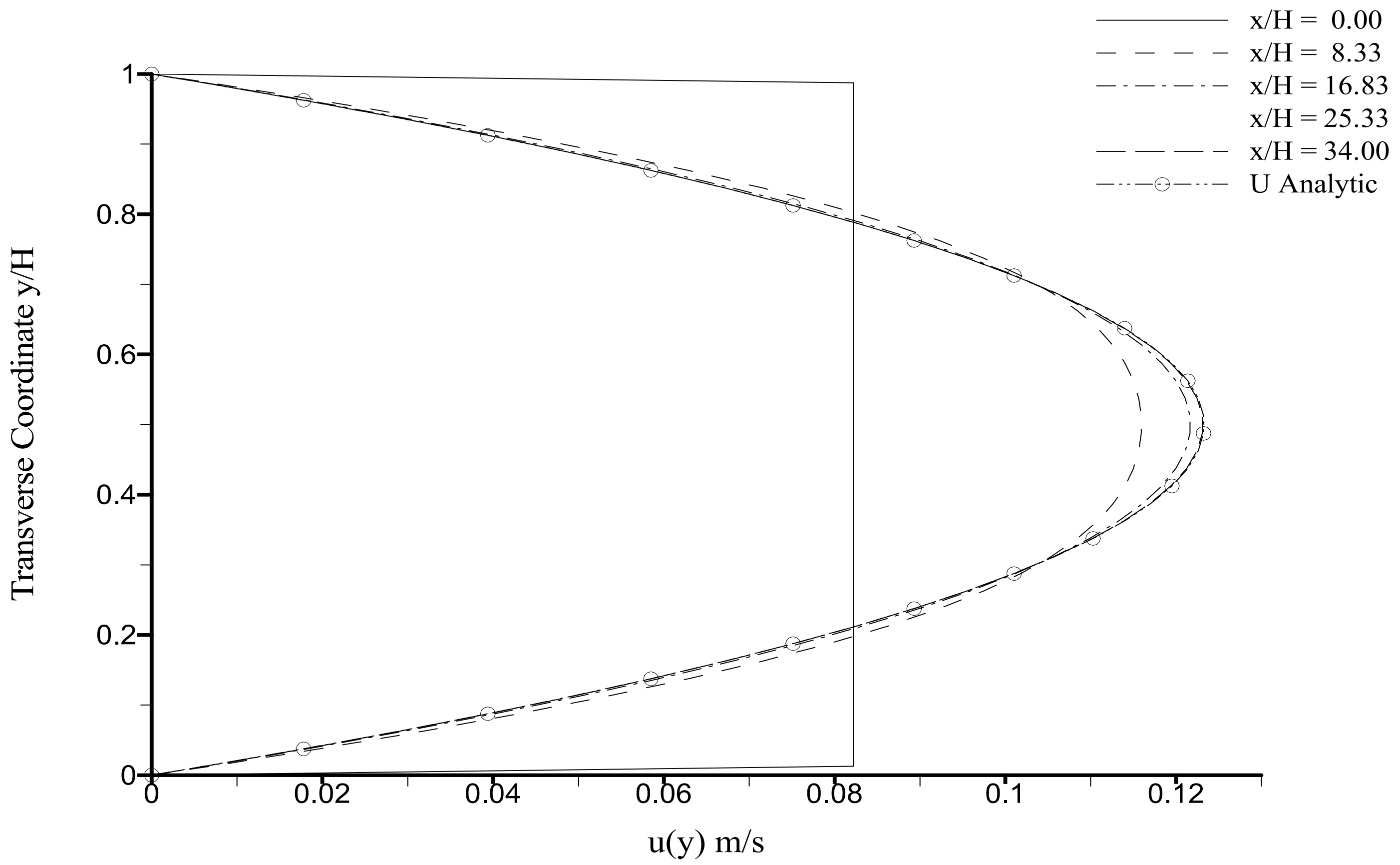

Fig. 5.1 Developing u-velocity profiles at various axial locations

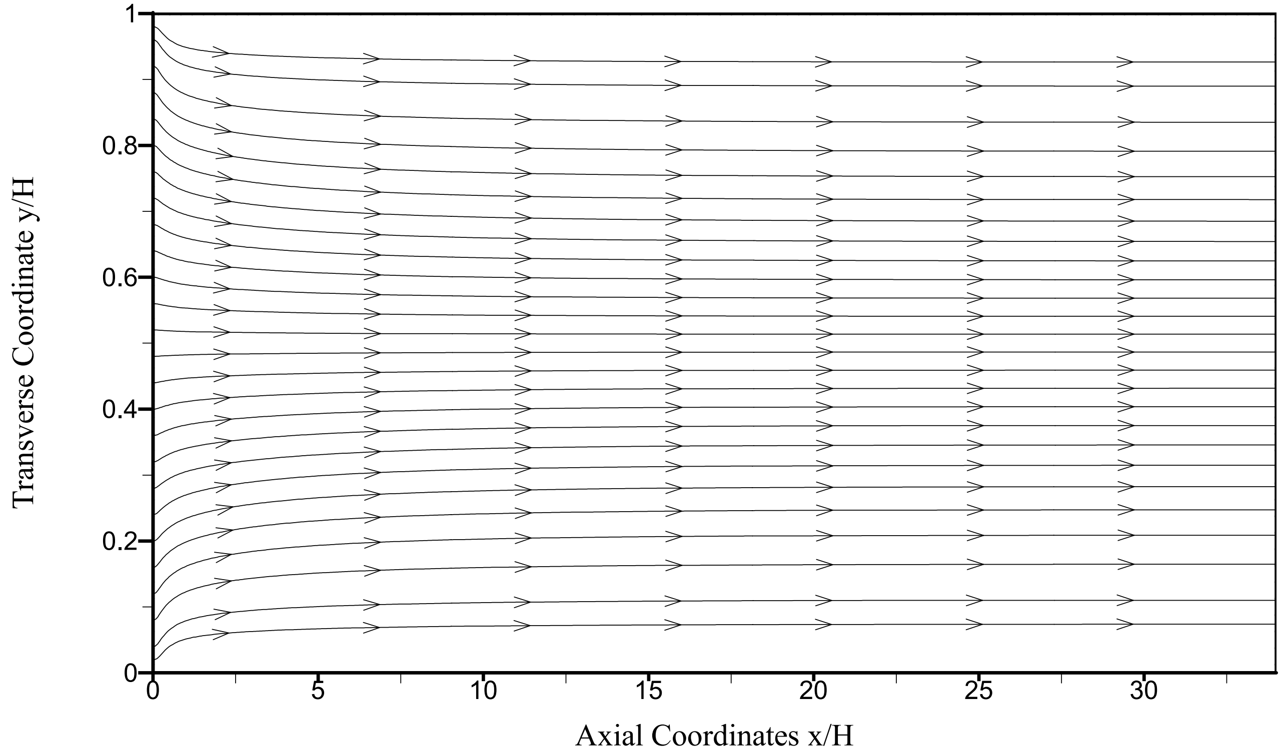

Fig. 5.2 Streamlines for the developing flow Test Case 1

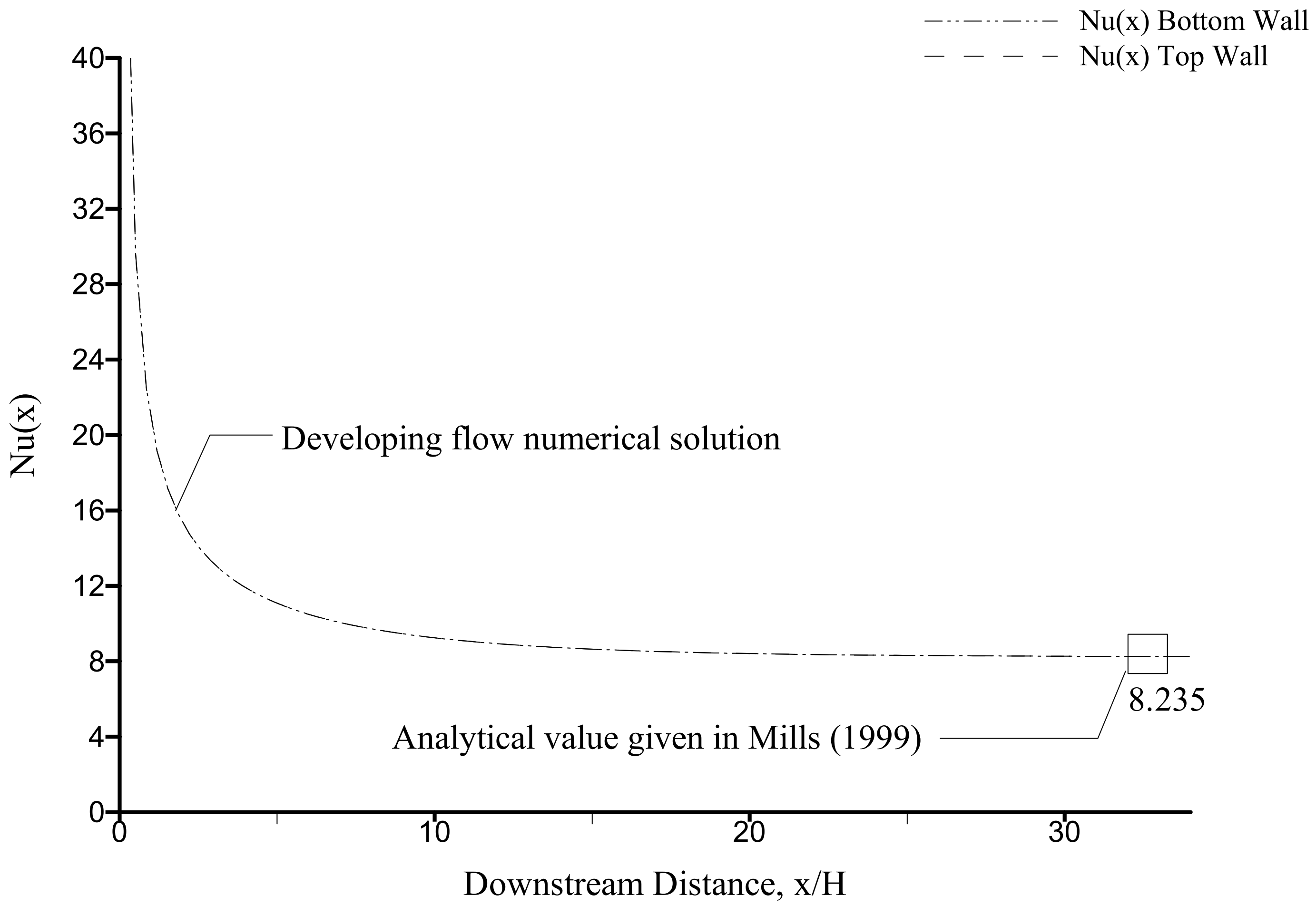

Fig. 5.3 Nusselt number for top and bottom wall for developing flow

By the use of the above criteria, it ensures that the developed code is capable of accurately solving the 2-D laminar developing flow problem subjected to UHF boundary conditions.

5.2 Validation Test Case 2: Heat Transfer in a 2-D Rectangular Channel with Porous Packed Bed

For the second validation test the simple porous media heat transfer case of forced convection was carried out in a channel filled with porous media. The wall temperature at various axial locations was used as the criteria for comparison in this test case. Nakayama [14] in one of his examples solved this problem. The boundary conditions that were imposed on this problem are the same as those shown in Table 5.1. The spatial variation of the porosity of the fully packed porous bed was defined as,

$$\varepsilon\left(y\right)=0.4\left[1+1.4e^{-5\left(\frac{H-y}{d_p}\right)}\right] \tag{5.2}$$

Where d_p = 1E-3 m is the particle diameter, H is the height of the channel, and y is the transverse coordinate. The permeability of the porous medium K (m^2) was defined by,

$$K=\frac{\varepsilon^3}{150\left(1-\varepsilon\right)^2}d_p^2 \tag{5.3}$$

The effective thermal conductivity was defined by,

$$k_e=\frac{\mu c_p}{Pr}\left[\varepsilon+\left(1-\varepsilon\right)\frac{k_s}{k_f}\right] \tag{5.4}$$

Table 5.3 Geometric, physical, and non-dimensional parameters for validation Test Case 2: 2-D rectangular channel with porous packed bed

<table>
<tr><td>$\mathrm{Re}_H = 1250$</td><td>Pr = 6</td><td>L = 1 m</td><td>H = 1E-1 m</td></tr>
<tr><td>$\rho = 1\mathrm{E}{+}3 \frac{\mathrm{Kg}}{\mathrm{m}^3}$</td><td>$\mu = 8\mathrm{E}{-}4 \frac{\mathrm{N.s}}{\mathrm{m}^2}$</td><td>$\dot{q}'' = 2000 \frac{\mathrm{W}}{\mathrm{m}^2}$</td><td>$\frac{k_s}{k_f} = 1.25$</td></tr>
<tr><td colspan="2">T_o (Uniform inlet temperature) = 20 C^o</td><td colspan="2">u_o (Uniform inlet u-velocity) = 1E-2 $\frac{\mathrm{m}}{\mathrm{s}}$</td></tr>
<tr><td colspan="2">d_p (Particle diameter) = 1E-3 m</td><td colspan="2">$c_p = 4.180\mathrm{E}{+}3 \frac{\mathrm{J.Kg}}{\mathrm{K}}$</td></tr>
</table>

In addition to these boundary conditions, Table 5.3 lists the geometric, physical, and non-dimensional parameters used for this test case.

Nakayama's [14] solution served as a very useful benchmark for the developed code. Although, Nakayama [14] made use of the axis of symmetry in his solution for this problem, this condition was not utilized here for validation. Rather the whole physical domain was used by reconstructing a symmetric grid about the axis of symmetry by using the non-uniform half domain grid used by Nakayama [14]. Nakayama's [14] solution was obtained by the use of the Hybrid Differencing Scheme and the SIMPLE (Semi-Implicit Method for Pressure Linked Equations) algorithm. In the developed code the solution was obtained by the use of the Power Law Scheme and the SIMPLEC (Semi-Implicit Method for Pressure Linked Equations Consistent) algorithm.

Table 5.4 Development of the temperature along the channel wall

x (m)	Nakayama's [14] Numerical (C^o)	Present Calculations Top Wall (C^o)	Present Calculations Bottom Wall (C^o)
0.15	25.4	25.4	25.4
0.35	27.7	27.7	27.7
0.55	29.6	29.6	29.6
0.75	31.3	31.3	31.3
0.95	32.7	32.7	32.7

The comparison of Nakayama's [14] solution with that obtained by the developed code is shown in Table 5.4. This comparison using two different methods and two different implementation techniques has proved beyond a doubt the ability of the developed code to solve numerical simulations in porous media.

5.3 Validation Test Case 3: Channel with a Single Porous Block

Having successfully demonstrated the ability of the developed code to solve simple problems in porous media and unobstructed flow in channels, as a final test case the problem with single porous block in a channel was investigated. Sung et al. [5] solved the problem of an isolated heat source in a channel with porous media. They used a single porous block. While considering Sung et al. [5] the developed code had to be modified slightly to account for the differences in the governing equation given in Sung et al. [5] and Nakayama [14]. Nakayama [14] considered the governing equations to be those listed in Equations 4.16 and 4.17 while the governing equation considered by Sung et al. [5] differed form Nakayama [14] only in the pressure drop term in Equations 4.16 and 4.17, Sung et al. [5] used ε instead of ε^2. However, this modification was restricted to the property subroutine of the developed code and did not pose many problems. The comparison between the results of the present study with the published results of Sung et al [5] are shown in Figures 5.4 and 5.5. Although, the maximum error, between the published results and the present test case for the lower surface of the channel, was below 12% (Re = 100) the other two cases showed small differences. On the other hand, excellent agreement of results were obtained for the lower surface of the channel for all the cases as can be clearly seen from Figure 5.5. This was important to establish because the porous block was attached to the lower surface of the channel; while the heating source was located at the bottom of the porous block.

All three cases have successfully demonstrated the ability of the developed code to yield physically realistic solutions. Since, this goal was achieved, the next goal was to establish the grid independence.

5.4 Grid Setup

Before describing the grid independence process it is important to understand how the actual grid was setup for the configuration considered in this study. The computational domain was divided into three distinct regions, the entry region, the baffle region, and the exit region. In the entry and the exit region of the computational domain a uniform grid was used in the x-direction i.e., in the axial direction. The size of the

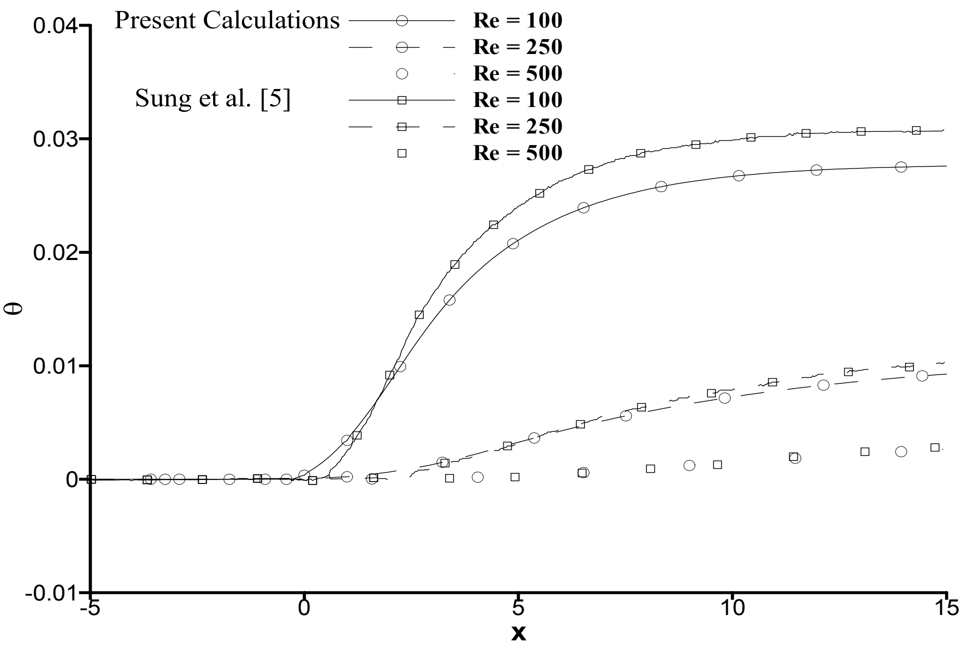

Fig. 5.4 Comparison of developing non-dimensional temperature of upper surface with previously published results

uniform control volume depended on the size of the largest axial control volume found in the module region, see Figure 3.2. This was done to reduce the number of nodes required for the simulation and at the same time reduce the miss match that would be encountered at the meeting planes of these three regions.

The x-direction gridlines setup in the module region (Figure 5.6) was complicated because each of the porous baffles required that a fine grid be placed on either side of the baffle. An unsuccessful attempt resulted while trying to use a geometric progression grid generation technique with large expansion factors in the x-direction. This attempt was unsuccessful because of the recirculation encountered between the

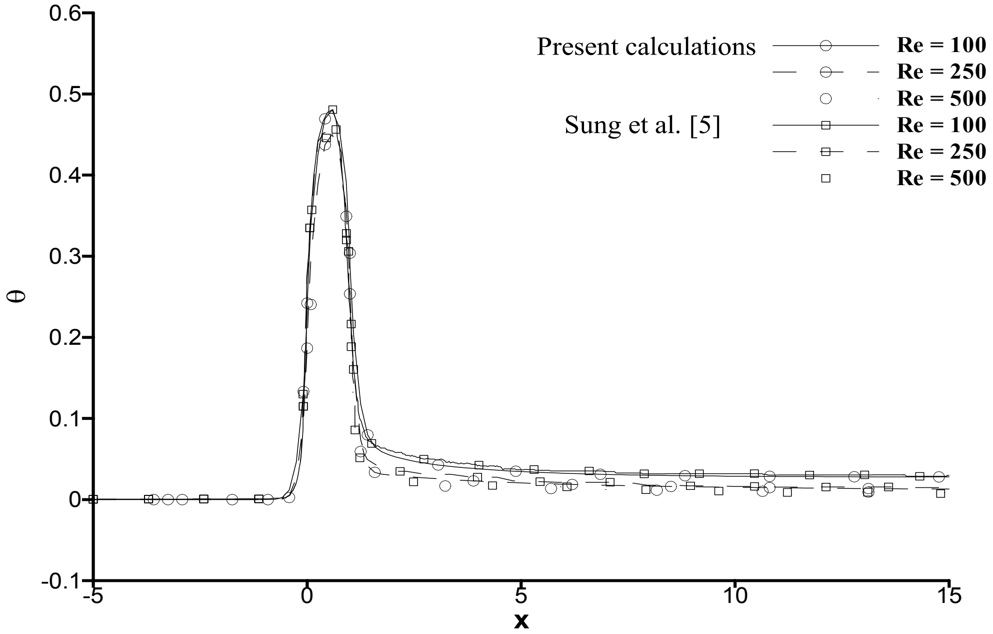

Fig. 5.5 Comparison of the developing non-dimensional temperature of lower surface with previously published results

porous baffles. This problem was overcome by adopting a grid generation technique described in Patankar [15]. The use of Equations 5.5 and 5.6 given in Patankar [15] was made while generating the grid in the x-direction, in the region between the baffles. These equations however, have been modified from the given form in Patankar [15] to better suit the current developed code but the essence remains the same.

$$\frac{XU(I)}{XL}=1-\left(1-\frac{I-2}{L1-2}\right)^{N} \qquad 5.5$$

$$\frac{XU(I)}{XL}=\left(1-\frac{I-2}{L1-2}\right)^{N} \qquad 5.6$$

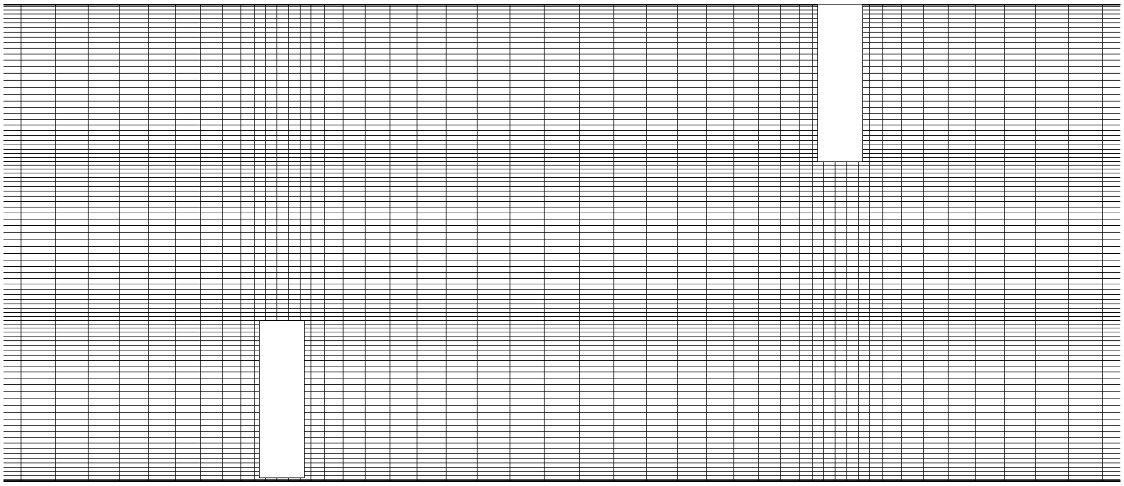

Fig. 5.6 A typical grid arrangement for a module

Where, XU is the location of the u-velocities in the x-direction and N is the expansion factor. N was taken to be 1.4 after trial and error especially taking into consideration the number of gridlines in the x-direction. The goal was to find an acceptable value of N which resulted in a requirement of x-direction gridlines to be less than 2000. XL is the length of the section where the gridlines were supposed to be setup. L1 is the total number of gridlines in the XL section. Besides this it is important to point out that since N > 0, Equation 5.5 results in a grid that is coarse near the left boundary and becomes progressively finer towards the right, see Figure 5.6 (e.g. region from the entrance of the module up to the left vertical face of the lower baffle). On the other hand Equation 5.6 results in a grid that is finer near the left boundary and becomes progressively more coarse towards the right, see Figure 5.6 (e.g. region beginning from the right vertical face of the upper baffle up to the exit of the module). At the entrance region of a module Equation 5.5 was used while in the region between the lower and upper baffles a symmetric use of Equation 5.6 was made followed by Equation 5.5, and finally in the exit region of the module Equation 5.6 was used to setup the grid. In addition to this, in the porous baffles a uniform grid in the x-direction was used, the size of which depended on the smallest control volumes generated by Equations 5.5 and 5.6.

In the y-direction, the grid setup was considerably simple; the height of the channel was divided into three identical regions. For the y-direction a geometric progression type grid was used with an expansion factor, that constrained the geometric expansion so that the ratio between the largest and smallest control volume was less than or equal to two. This was done to minimize computational errors and to capture the recirculation zones in the flow field to yield sensible results. Besides this in each of the identical regions the size of the control volumes take the shape of a convex lens i.e., finer at the edges and coarser at the center.

5.5 Grid Independence

Now that the grid setup has been explained it is possible to explain the grid independence test carried out. For grid independence the following parameters Da = 1.791E-5, H/w = 12, d/w = 11, b/w = 4, K = 100, and Re = 400 were considered. Grid independence was carried out by fixing JPMAX = 92. This was done with the experience gained from previous unsuccessful attempts of using geometric progression in the x-direction for the grid independence test. In those tests, it was noted that the present study was not sensitive to the variations in the y-direction for JPMAX > 74. The grid independence test was done using the following grid sizes 29x92, 41x92, 49x92 and

61x92 per module in all 8 modules, besides these 8 modules, the entry module and the exit module had uniform gridlines in the x-direction. This systematic increase was useful in determining the grid independent solution for the given set of grids.

The results for the various grid tests have been tabulated in Tables 5.5 and 5.6. It is evident from these tables that the difference in the solutions for the grid case 49 x 92 and 61 x 92 are very small. The maximum absolute error for these two cases is: for friction factors it was less than 2.6%, for the mean Nusselt number it was less then 1.8%. This concludes the validation and grid independence tests.

Table 5.5 Average friction factors for various grids

Module	29x92	41x92	49x92	61x92
1	29.57	31.67	31.25	31.01
2	32.05	36.16	36.54	36.96
3	29.95	36.42	36.59	37.53
4	26.12	32.12	31.03	31.33
5	23.70	27.71	26.21	25.82
6	22.83	25.76	24.73	24.41
7	22.66	25.59	25.12	25.26
8	16.58	17.09	17.15	17.49

Table 5.6 Average mean Nusselt number ratio for various grids

Module	29x92	41x92	49x92	61x92
1	1.1434	1.1381	1.1221	1.1151
2	1.2371	1.2846	1.2497	1.2434
3	1.2098	1.2894	1.2606	1.2662
4	1.1822	1.2846	1.2833	1.3057
5	1.1792	1.2862	1.2824	1.2931
6	1.1800	1.2776	1.2694	1.2698
7	1.1803	1.2737	1.2642	1.2606
8	1.2200	1.3240	1.2985	1.2915

CHAPTER VI

RESULTS AND DISCUSSIONS

As discussed earlier in Section 3.5 the governing independent parameters influencing fluid flow and heat transfer in a channel with porous baffles are the Reynolds number (Re), Darcy number (Da), Prandtl number (Pr), the baffle thickness aspect ratio (H/w), non-dimensional baffle spacing (d/w), non-dimensional baffle height (b/w), the thermal conductivity ratio $\left({}^{k_s}\!/_{k_f} \right)$, and the porosity (ε) of the porous medium. In parametric studies the Reynolds number was varied from 100 – 400. Calculations were made for Darcy number values of 8.783E-6, 1.309E-5, and 1.791E-5, a selection of these Darcy numbers were guided by the work of Kim et al. [8]. In this study, consideration was given to airflow, therefore the Prandtl number was fixed at 0.7. In this work three different baffle value thicknesses were considered (H/w = 12, 6, and 4), and the channel height (H) was fixed, accordingly H/w = 12 represented a very thin baffle and H/w = 4 represented a relatively thick baffle. While varying d/w, the value of H/w was fixed at 12, thus d/w = 15 represents the largest baffle spacing and d/w = 11 represents the smallest baffle spacing, in all three different baffle spacings (d/w = 11, 13, and 15) were considered in this study. The height of the baffles was also held fixed at one-third the channel height therefore the non-dimensional baffle height was always one-third the ratio of H/w. The thermal conductivity ratio was varied from 1 to 100; the upper bounds were set by taking into account a study by Kelkar [9]. In this study, the porosity ε of the porous media was fixed at 0.92, and the Forchheimer

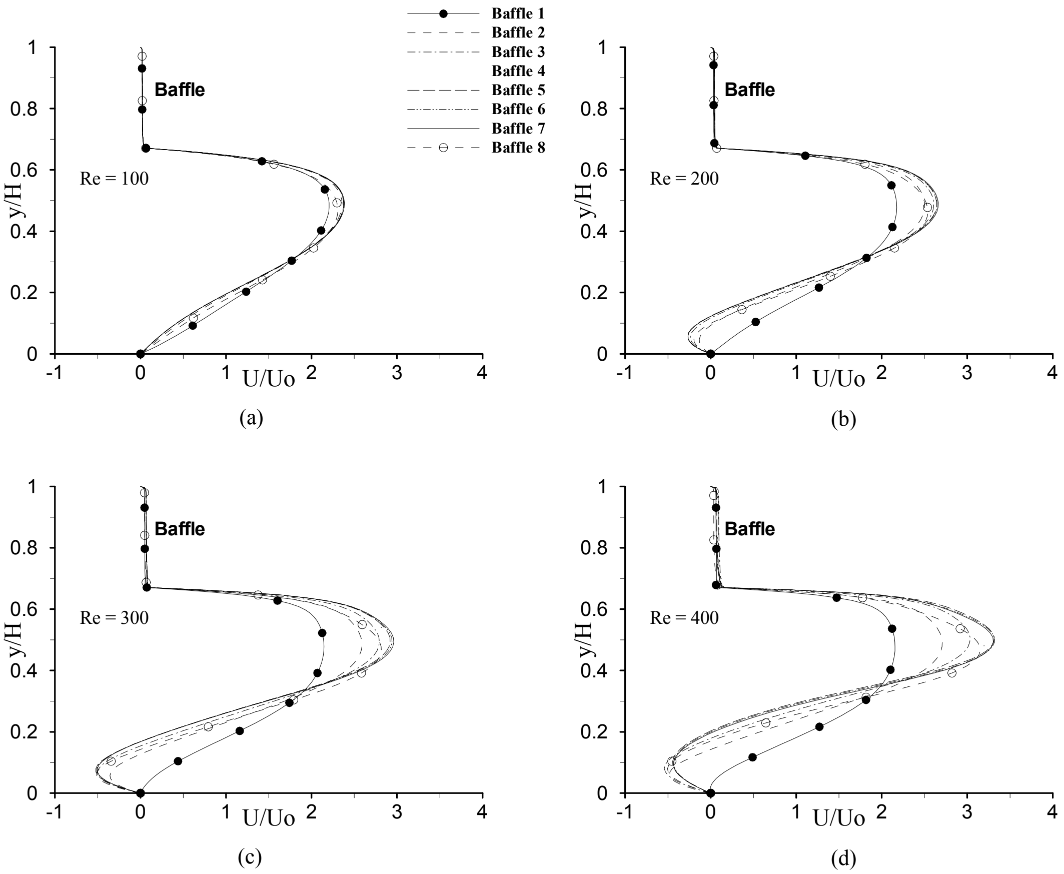

(a) (b) (c) (d)

Fig. 6.1 Effect of Reynolds number on the developing velocity profiles along the centerlines of the upper wall baffles in the transverse direction Da = 8.783E-6, H/w = 12, d/w = 11, b/w = 4: (a) Re = 100, (b) Re = 200, (c) Re = 300, and (d) Re = 400

coefficient was taken to be 0.55 in line with the study by Sung et al. [5]. In all 180 different parametric runs were made. However, only representative results are presented in this thesis. Figures 6.1 and 6.2 show the effect of Re on the non-dimensional stream-wise velocity profiles. The velocity was normalized with respect to inlet velocity Uo. Velocity profiles presented in Figures 6.1 and 6.2 corresponds to the midline of each baffle. Figures 6.1 and 6.2 illustrate the non-dimensional velocities along the top and bottom walls, respectively. The Reynolds number was varied from 100 to 400 while

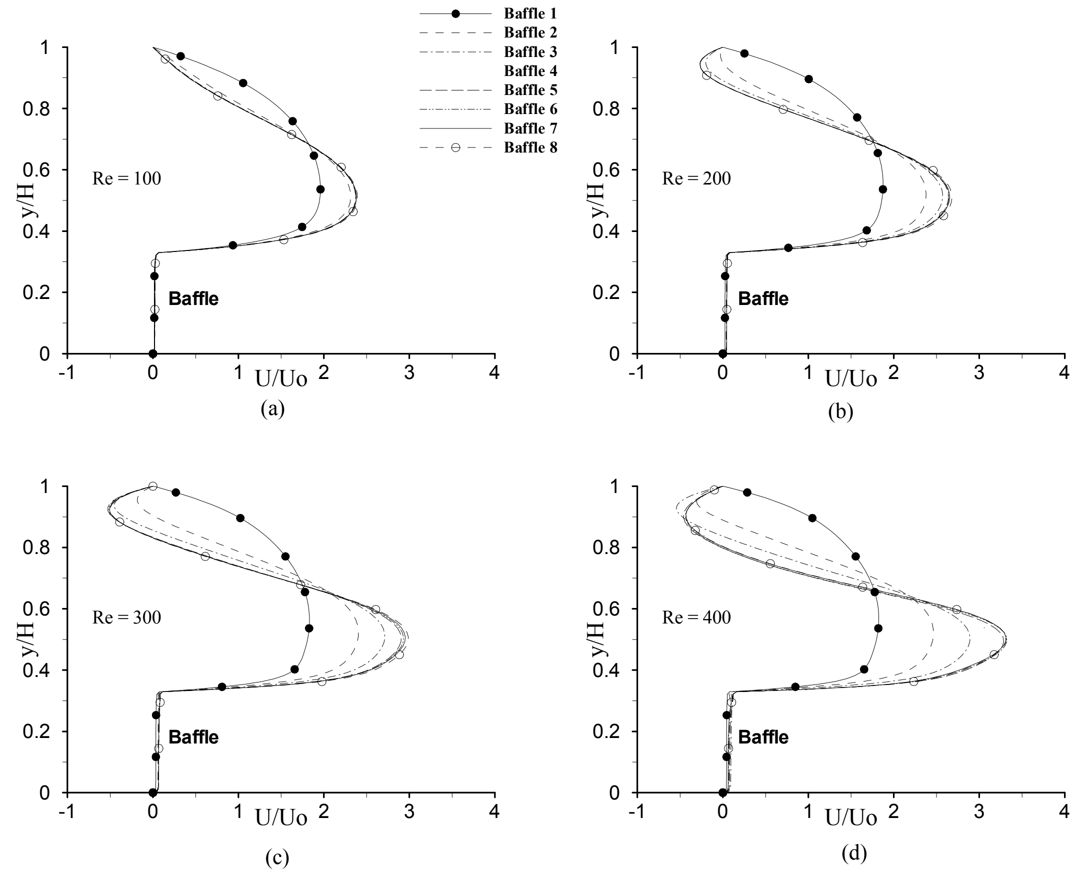

Fig. 6.2 Effect of Reynolds number on the developing velocity profiles along the centerlines of the lower wall baffles in the transverse direction Da = 8.783E-6, H/w = 12, d/w = 11, b/w = 4: (a) Re = 100, (b) Re = 200, (c) Re = 300, and (d) Re = 400

other parameters were held constant (Da = 8.783E-6, H/w = 12, d/w = 11, and b/w = 4). As expected the maximum velocity increases with the increase in Re. Typically, the maximum velocity occurs in the centerline of the channel. Along the top and bottom walls, the velocity inside the baffles is fairly constant for all baffles.

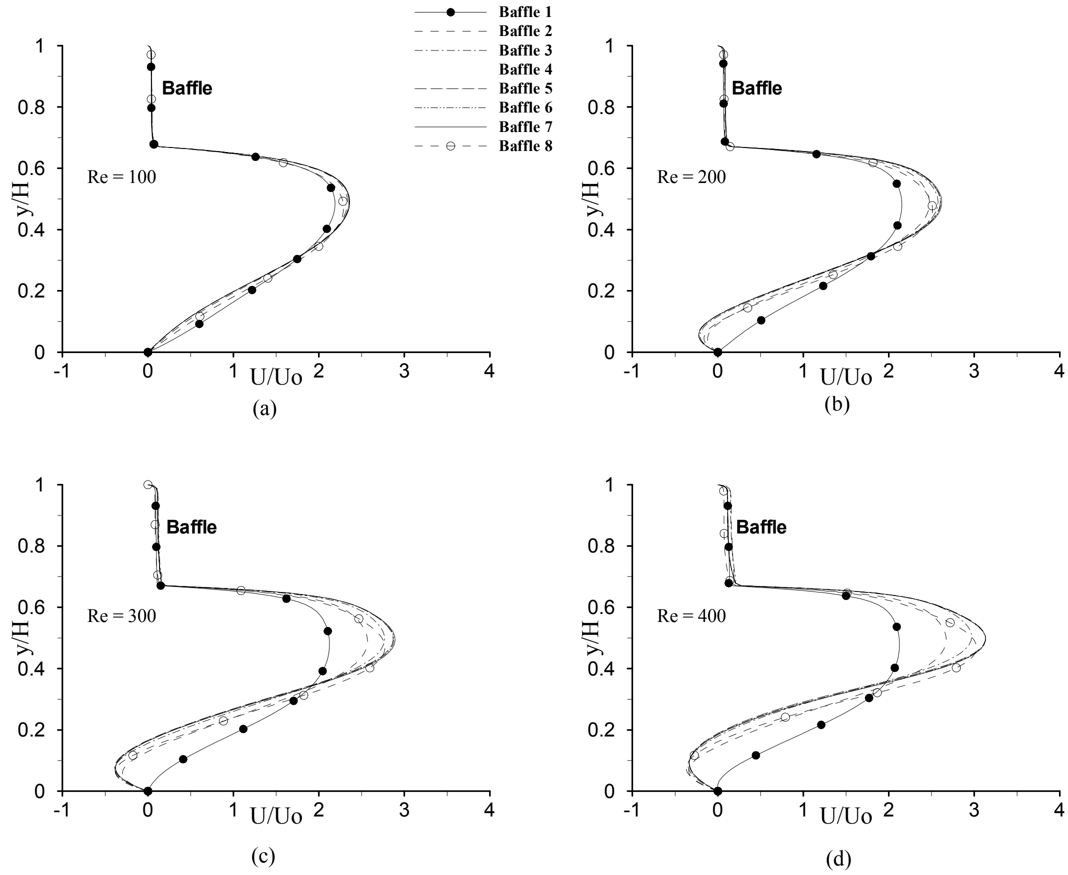

Fig. 6.3 Effect of Reynolds number on the developing velocity profiles along the centerlines of the upper wall baffles in the transverse direction Da = 1.791E-5, H/w = 12, d/w = 11, b/w = 4: (a) Re = 100, (b) Re = 200, (c) Re = 300, and (d) Re = 400

6.1 Effects of Reynolds Number on the Developing Velocity Profiles

Representative stream-wise developing velocity profiles along the centerline of the upper and lower wall baffles are shown in Figures 6.3 and 6.4. The parameters took the following values Da = 1.791E-6, H/w = 12, d/w = 11, b/w = 4. For the purpose of clarity henceforth the word “core” will be used to represent the rectangular zone from the entry to the exit of the channel that does not have any porous media in it. The word “cavity” will be used to represent the space between two consecutive lower or upper

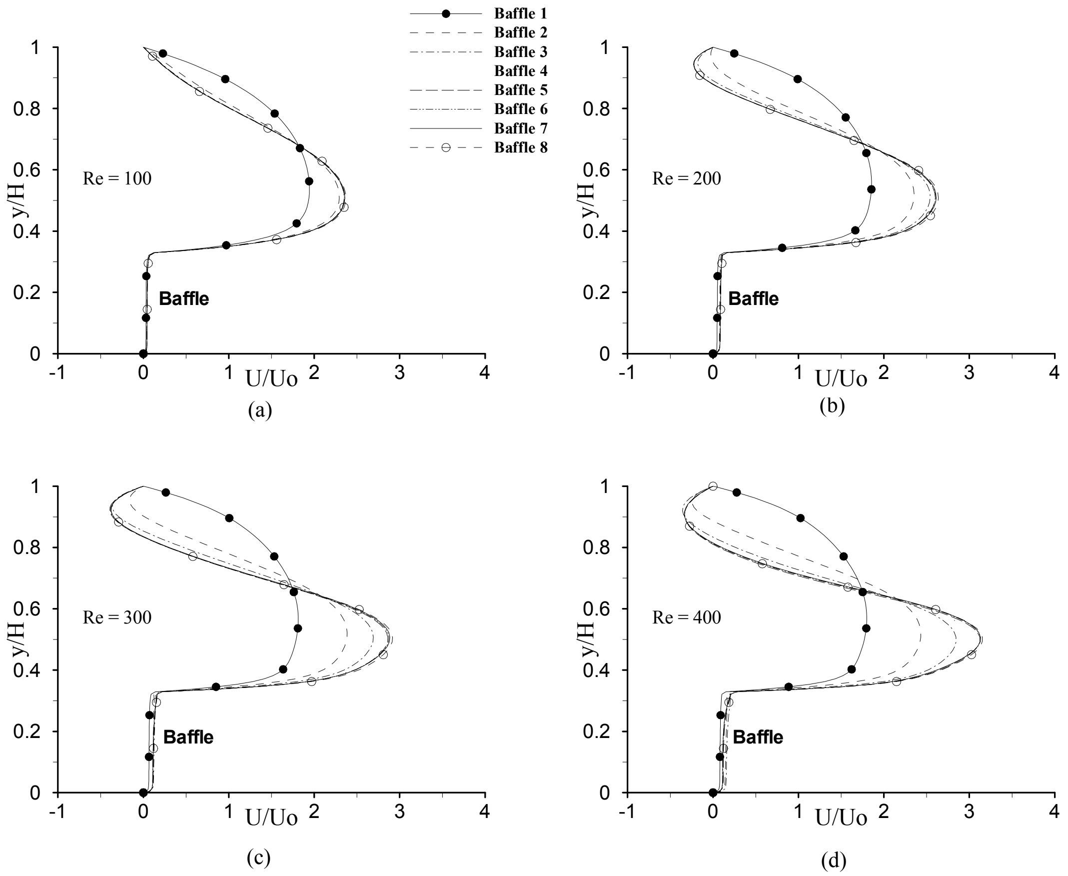

Fig. 6.4 Effect of Reynolds number on the developing velocity profiles along the centerlines of the lower wall baffles in the transverse direction Da = 1.791E-5, H/w = 12, d/w = 11, b/w = 4: (a) Re = 100, (b) Re = 200, (c) Re = 300, and (d) Re = 400

wall baffles that are bound by the nearest wall and the nearest edge of the core in the transverse direction. From Figures 6.3 and 6.4 it can be established that as the Reynolds number increases the maximum velocity in the core increases while, the negative velocity in the cavity that is transversely opposite to the baffle in consideration, increases in magnitude. This increase in the negative velocity is the direct result of the conservation of mass principle as the excess flow in the core has to be compensated with an increase in the negative flow in the cavities. For the upper wall baffles at higher

Reynolds numbers (Re = 300 and 400) it is evident that the velocity profile for the last baffle (8th baffle) was skewed toward the lower wall of the channel, this can be clearly seen in Figures 6.1c, 6.1d, 6.3c, and 6.3d. This is because the location of the last baffle from the entrance of the channel is on the upper wall. The absence of the lower baffle in the exit region results in a sudden expansion. This sudden expansion is more pronounced for Re > 200, and these cases have larger recirculation regions in all the cavities. Although the velocity profile inside the baffle is uniform and small it can be seen in

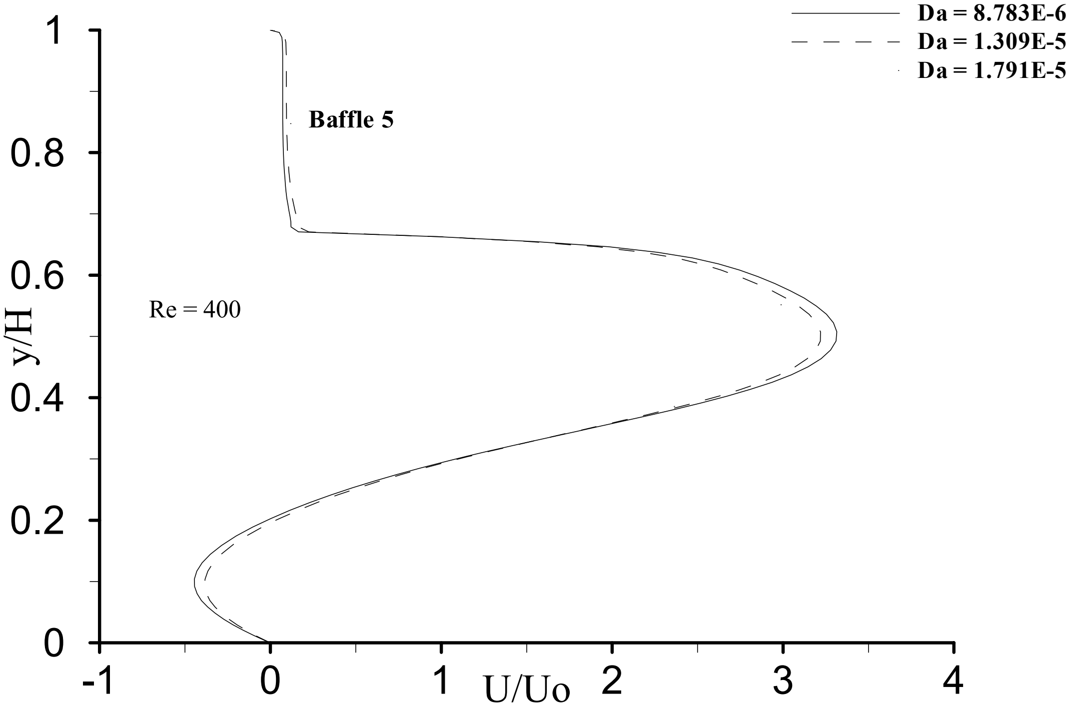

Fig. 6.5 Effect of Darcy number on the developing velocity profiles along the centerlines of the upper wall fifth baffle in the transverse direction Re = 400, H/w = 12, d/w = 11, b/w = 4

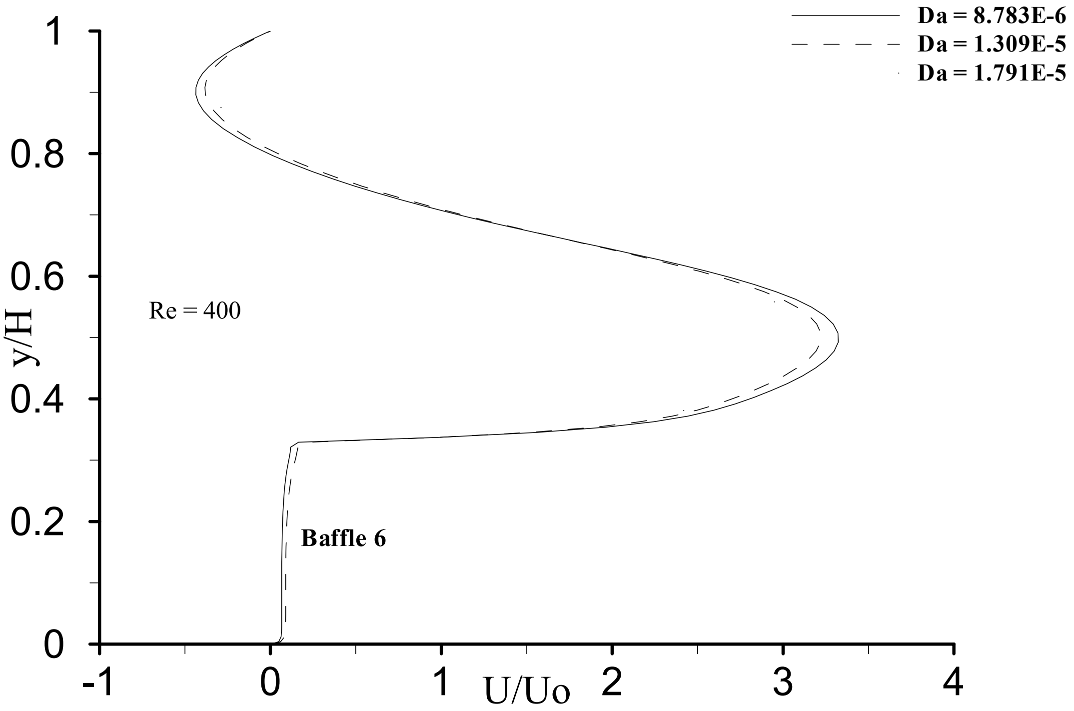

Fig. 6.6 Effect of Darcy number on the developing velocity profiles along the centerlines of the lower wall sixth baffle in the transverse direction Re = 400, H/w = 12, d/w = 11, b/w = 4

Figure 6.1 - 6.4 that it marginally increases as Reynolds numbers increase from 100 to 400.

6.2 Effects of Darcy number on the Developing Velocity Profiles

A negligible change in the velocity profiles was observed when Darcy numbers were varied in the selected range. A comparison of Figures 6.1 to 6.3 and 6.2 to 6.4, respectively, indicates negligible difference; therefore, a larger and more distinct velocity profile representation, like Figures 6.5 and 6.6, has been plotted to clearly show the small variations in the velocity profiles. Figure 6.5 shows the velocity profile in a comparison between the fifth porous baffle along the upper wall. Figure 6.6 shows velocity profile in the sixth porous baffle along the lower wall. In Figures 6.5 and 6.6, the selected Darcy numbers were taken into consideration to provide a clear and better understanding of the changes that affect the velocity profiles.

Examining the velocity profiles in Figures 6.5 and 6.6 it can be seen that there is a negligible change in the velocity profiles when the Darcy number was varied from 8.783E-6 to 1.791E-5. The Darcy number is directly proportional to the permeability$\left(K/H^2 \right)$. Accordingly, the velocity profile should assume the shape of the velocity profile that would be obtained from the study of a fully developed flow in a channel without obstruction $\left(K \to \infty \right)$ to the flow. However, due to the selection of the Darcy numbers based on the permeability values given in Kim [8], this comparison did not yield a large difference in the velocity profiles. Even so, a decrease was noted in the core velocity when the Darcy number was 1.791E-5. While minor velocity increases as expected were observed in the middle of the baffles. This velocity increase in the middle of the baffles occurs at the expense of the maximum core velocity and is the direct consequence of the conservation of mass.

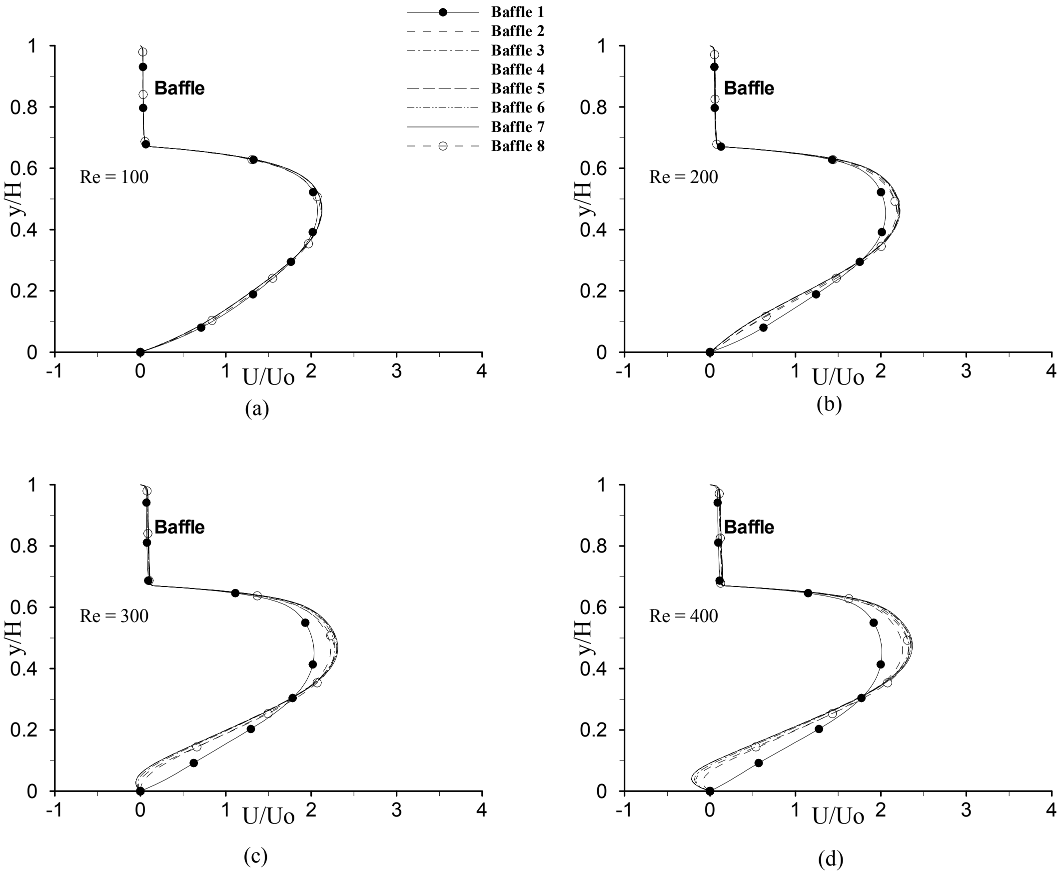

(a) (b) (c) (d)

Fig. 6.7 Effect of Reynolds number on the developing velocity profiles along the centerlines of the upper wall baffles in the transverse direction Da = 1.791E-5, H/w = 12, d/w = 15, b/w = 4: (a) Re = 100, (b) Re = 200, (c) Re = 300, and (d) Re = 400

6.3 Effects of Non-Dimensional Baffle Spacing (d/w) on the Developing Velocity Profiles

Comparison of Figures 6.3 to 6.7 and 6.4 to 6.8, respectively, shows the most drastic changes to developing velocity profiles. When the non-dimensional baffle spacing (d/w) between two consecutive upper and lower baffles increases from 11 to 15 the maximum velocity in the core drastically decreases. This decrease in the core occurs because there is more space in the cavities for the flow to expand, as it flows over and

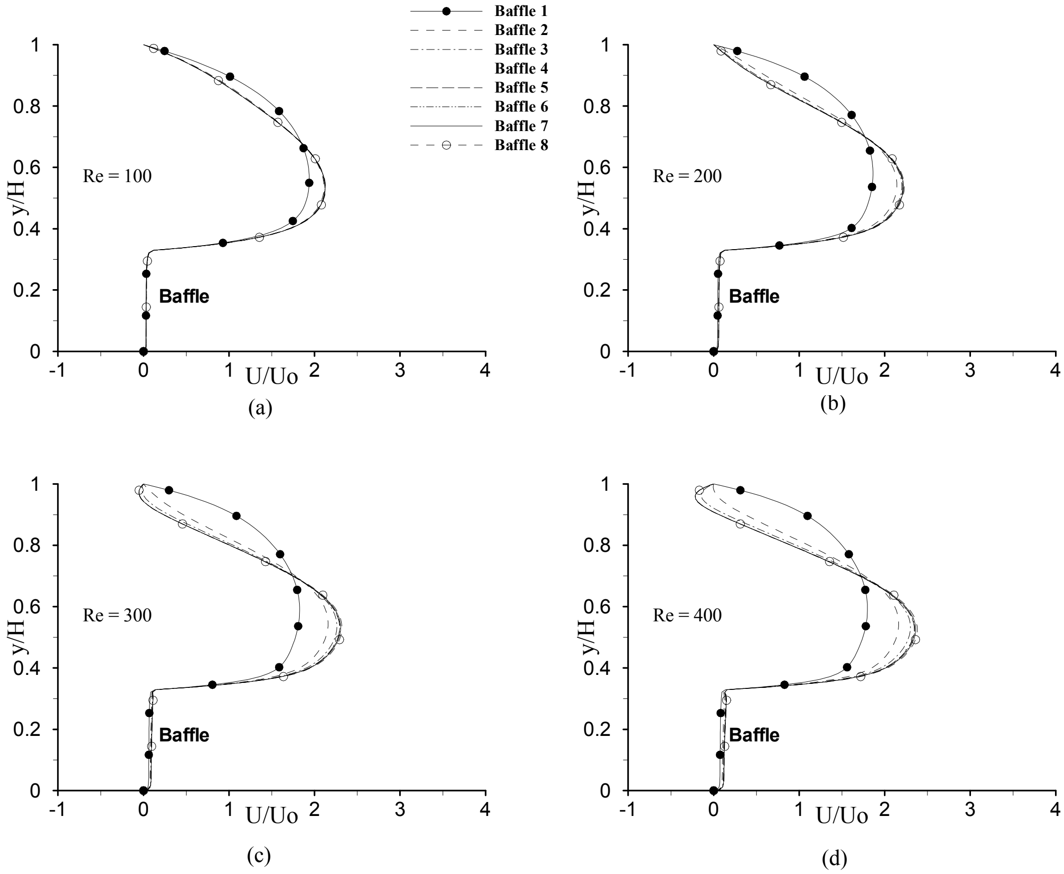

Fig. 6.8 Effect of Reynolds number on the developing velocity profiles along the centerlines of the lower wall baffles in the transverse direction, Da = 1.791E-5, H/w = 12, d/w = 15, b/w = 4: (a) Re = 100, (b) Re = 200, (c) Re = 300, and (d) Re = 400

through each baffle preceding a cavity. In addition, for d/w = 15 it is evident that flow attains periodically fully developed profile downstream of the third baffle from the entrance for Re = 400, this happens to be the case for both the upper wall baffles and the lower wall baffles as evident from Figures 6.7d and 6.8d. For Re = 200 and Re = 300 the flow attains periodically fully developed profile downstream of the second baffle Figures 6.7b-c and Figures 6.8b-c. For Re = 100 the flow attains periodically fully developed velocity profile downstream of the first baffle Figures 6.7a and 6.8a. For the d/w = 15,

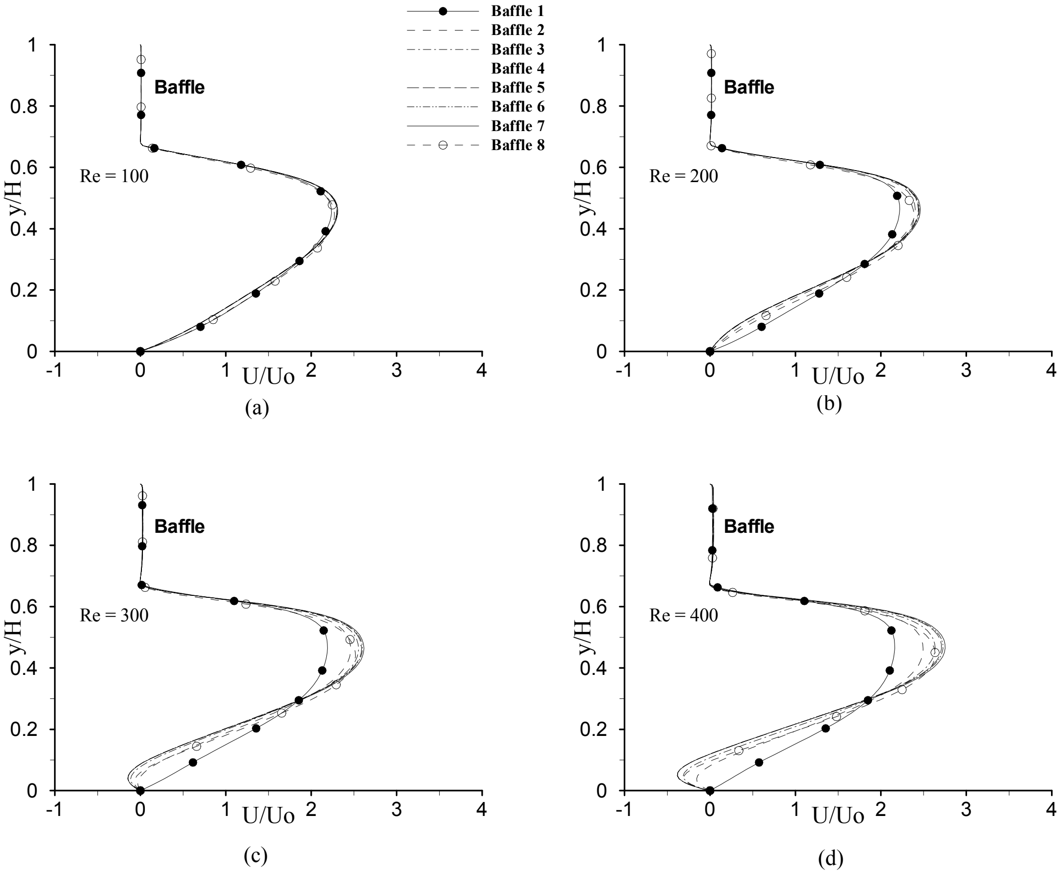

(a) (b) (c) (d)

Fig. 6.9 Effect of Reynolds number on the developing velocity profiles along the centerlines of the upper wall baffles in the transverse direction Da = 1.791E-5, H/w = 4, d/w = 11/3, b/w = 4/3: (a) Re = 100, (b) Re = 200, (c) Re = 300, and (d) Re = 400

from Figures 6.8 and 6.9 it can be seen that the velocity profile at the last (8^{th}) baffle, for Re = 300 and Re = 400, does not skew towards the bottom wall this is because as the d/w increases each baffle becomes isolated from its neighbors.

6.4 Effects of Baffle Thickness Aspect Ratio (H/w) on Developing Velocity Profiles

As the porous baffles become thicker, the ability of the fluid to penetrate through

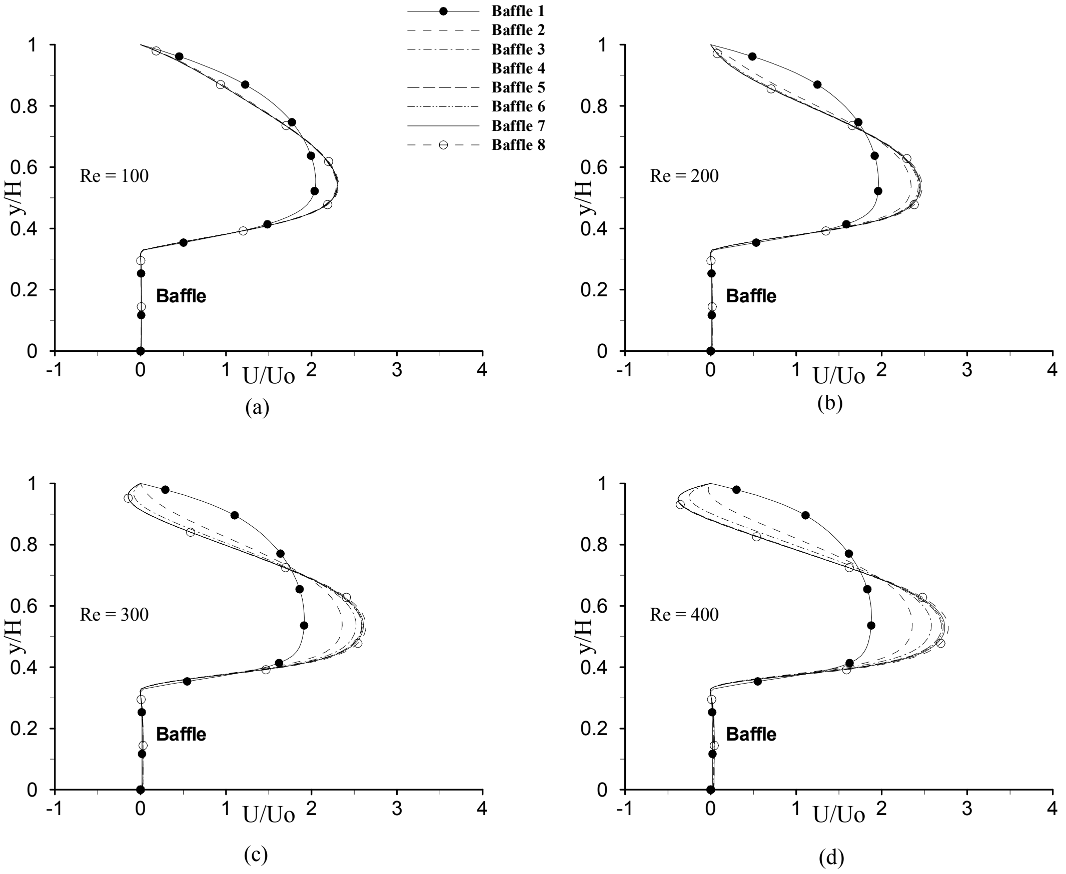

(a) (b)

(c) (d)

Fig. 6.10 Effect of Reynolds number on the developing velocity profiles along the centerlines of the lower wall baffles in the transverse direction Da = 1.791E-5, H/w = 4, d/w = 11/3, b/w = 4/3: (a) Re = 100, (b) Re = 200, (c) Re = 300, and (d) Re = 400

them decreases, and the immediate conclusion would be to assume that the velocity in the core region should increase to satisfy the mass balance. However, this was found not to be the case, this abnormality is documented in Figures 6.9 and 6.10. A close comparison of these figures with Figures 6.3 and 6.4, respectively, would clearly establish that the velocity decreases in the core regions with a decrease in H/w (increase in baffle thickness) from 12 to 14. This decrease can be clearly seen when comparing Figures 6.3d with 6.9d and 6.3d with 6.10d. The case of Re = 400 encounters the most change when the baffle thickness increases (H/w decreases 12 to 4). Besides the decrease in the core velocity, a few other changes were noticed for the thick porous baffles case. The negative velocities (recirculation) in the cavity zones decrease in magnitude. The axial velocity along the centerline of the baffles is uniform but practically zero. The core velocity for the upper wall baffles are skewed towards the lower wall and the core velocity for the lower wall baffles are skewed towards the upper wall. The reason for the decrease in the recirculation length (stream-wise), in the cavity zones, occurs because the fluid cannot penetrate the thick porous baffles. This failure results in the recirculation behind the porous baffle not being blown farther downstream and away from the porous baffles. This stops the recirculation regions from elongating like that found when using thin porous baffles. The decrease in the axial velocity is bound to occur because the fluid faces greater resistance as it flows through the porous baffles. In fact, there is a possibility for stagnation to occur if the baffles are sufficiently thick. The conservation of mass imposes the constraint that the fluid that enters the porous baffles must exit the baffles; but since the fluid cannot penetrate the porous baffles to exit behind the baffles, it exits the porous baffles through the horizontal surface (free end). This curving of the flow in the porous baffles is better known as the “blowing effect”. The blowing effect and the lack of through-flow in the porous baffles results in the recirculation height increasing while the thickness of the baffles is increased. This taller recirculation obstructs the through-flow in the core region causing it to impinge into the cavity regions. Now the fluid expands into the cavities due to the presence of the tall recirculation, this expansion of fluid into the cavity in turn decreases the maximum velocity in the core, to preserve the conservation of mass.

6.5 Calculation of Streamlines

After obtaining the converged solution for the velocities and the temperature the streamlines were computed, by the use of the well known relationships, connecting the velocities and the stream function in the form of:

$$\psi_{x,y=0} = \psi_{x=0,y=0} - \int_0^x v dx \tag{6.1}$$

$$\psi_{x,y} = \psi_{x,y=0} - \int_0^y u dy \tag{6.2}$$

In Equation 6.1 $\psi_{x=0,y=0}$ was arbitrarily taken to be zero, while the integral term on the right side of Equation 6.1 computes to zero because the v-velocity is zero along the lower wall of the parallel plate channel. Now it should be noted that the stream function ψ is not in the non-dimensional form. The current units of the stream function ψ is m^2/s, in order to make the stream function non-dimensional it is necessary to compute Ψ^* by using:

$$\Psi^* = \frac{\psi}{U_o H} \tag{6.3}$$

Where U_o is the inlet velocity and H is the height of the channel. In the developed code the stream function ψ was computed by using Equation 6.2 and noting that the right-hand side of Equation 6.1 is zero. Then the computed stream function ψ was made into the non-dimensional stream function Ψ^* by the use of Equation 6.3. The non-dimensional stream function Ψ^* was defined to be 0 at the lower wall of the channel and 1 at the upper wall of the channel. However, computed values of Ψ^* lower than zero and higher than one were found in cavities between the adjacent baffles, the lower cavities having values less than zero and the upper cavities having values above one.

6.6 Effect of Reynolds Number on the Streamlines

Figure 6.11 is a representative figure of the non-dimensional stream function Ψ^* for Da = 1.791E-6, H/w = 12, d/w = 11, b/w = 4, with Re = 100, 200, 300, and 400, respectively. Table 6.1 lists the minimum and the maximum values of the non-dimensional stream function Ψ^* found in Figure 6.11. A close examination of Figure 6.11 would reveal certain distinct features and trends. As the Reynolds number increases from 100 to 400 a secondary recirculation appears along the bottom wall for Re = 400 in the exit module of the channel, in addition to this the eye of largest recirculation increases in magnitude from 1.03 to 1.07 while, the length and the size of the recirculation itself gets larger. Besides these clearly visible changes, the recirculation between adjacent baffles is blown farther downstream of the vertical face of the porous baffle as the Reynolds number increases from 100 to 400. This downstream blowing of the recirculation behind each baffle causes the recirculation to practically occupy the whole cavity. This fact is clearly visible for the case of Re = 400, this occupation of the cavity by a recirculation obstructs the flow in the core from coming into contact with either the lower or upper wall of the channel depending on the location of the cavities.

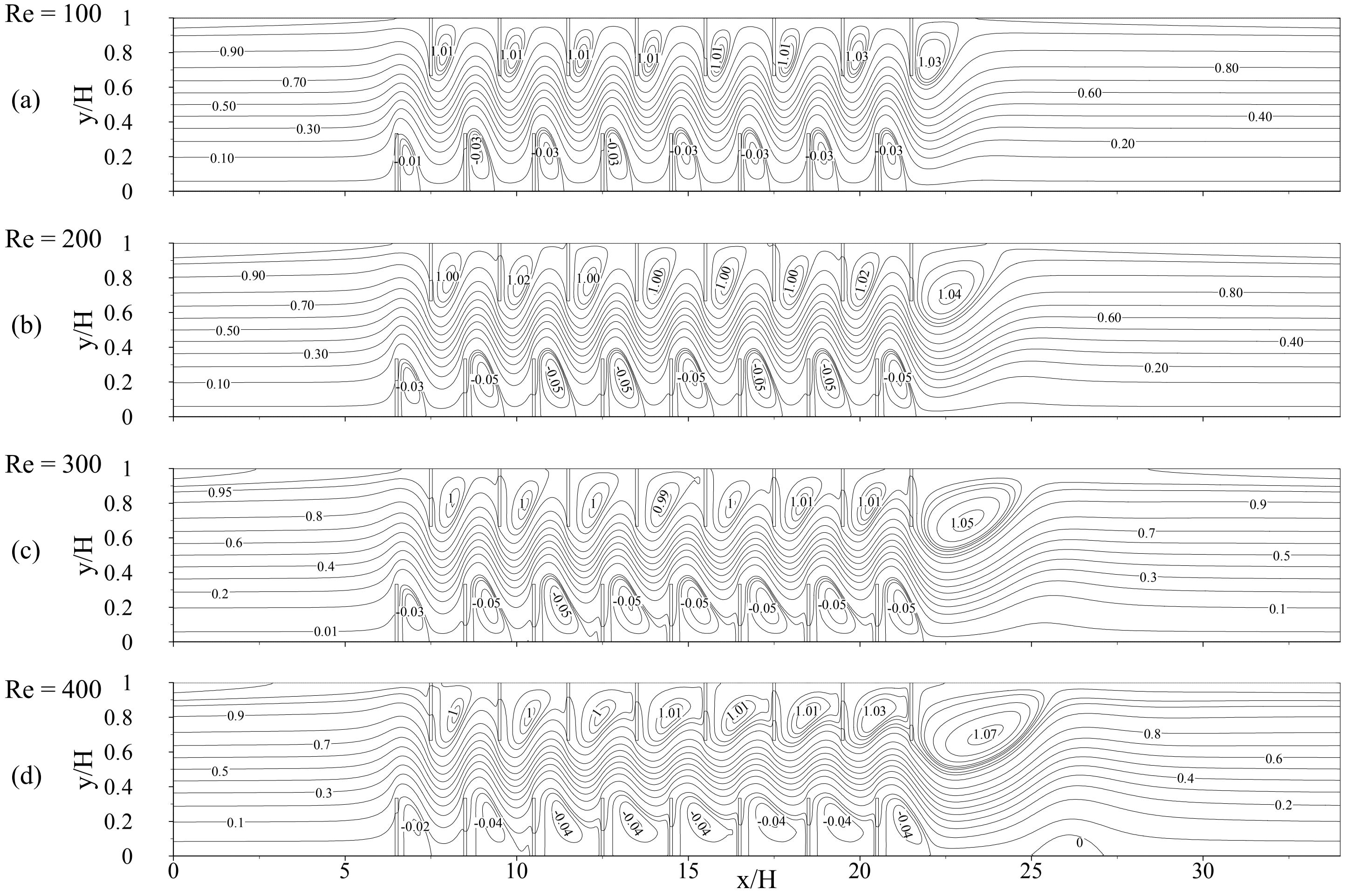

Fig. 6.11 Effects of Reynolds number on the non-dimensional stream function Ψ^* Da = 1.791E-6, H/w = 12, d/w = 11, b/w = 4: (a) Re = 100, (b) Re = 200, (c) Re = 300, and (d) Re = 400

This in turn will have significant impact on the Nusselt number (heat transfer) details which shall be discussed later in this chapter. A careful examination of Figure 6.11a (Re = 100) would also reveal that the length of the recirculation downstream of each baffle was less than half the non-dimensional baffle spacing (d/w). At this point it should be noted by observing the geometry in Figure 6.11 that if any two adjacent baffles on the top or bottom wall were to be selected then there will always be a single baffle between them on the opposite wall. A centerline through this single baffle on the opposite wall will bisect the baffle spacing (d/w) between these two adjacent baffles. Thus, the velocity profiles along this centerline will not take on negative values whenever the length of the recirculation downstream of each baffle is less than half the non-dimensional baffle spacing (d/w). In Figures 6.1a, 6.2a, 6.3a, and 6.4a the absence of negative velocities in the velocity profiles can be noted. In addition, for all the parametric runs with Re = 100 the recirculation downstream of each baffle was found to

Table 6.1 The minimum and the maximum non-dimensional stream function Ψ^* values for varying Reynolds numbers Da = 1.791E-6, H/w = 12, d/w = 11, b/w = 4

Re	Ψ^*_{min}	Ψ^*_{max}
100	-0.037015	1.03179
200	-0.053757	1.04626
300	-0.051776	1.05612
400	-0.041950	1.07491

Table 6.2 The minimum and the maximum non-dimensional stream function Ψ^* values for varying Darcy numbers Re = 400, H/w = 12, d/w = 11, b/w = 4

Da	Ψ^*_{min}	Ψ^*_{max}
Solid Baffles	-0.112729	1.12261
8.783E-6	-0.065627	1.09211
1.309E-6	-0.052833	1.08334
1.791E-6	-0.041950	1.07491

be less than half the non-dimensional baffle spacing (d/w) for each corresponding parametric run.

6.7 Effects of Darcy Number on the Streamlines

Table 6.2 lists the minimum and the maximum values of the non-dimensional stream function values Ψ^* shown in Figure 6.12. Figure 6.12 is a representative figure of the non-dimensional stream function Ψ^* for the case of Re = 400, H/w = 12, d/w = 11, b/w = 4, for different Darcy numbers (Da = 0 (solid baffles), 8.783E-6, 1.309E-5, and 1.791E-5). The largest recirculation in the exit module decreases from 1.12 to 1.07 in intensity as the Darcy numbers increase from 0 (solid baffles) to 1.791E-6. It should be noted that the solid baffles case can be approximated by setting the Darcy number to zero although it physically does not exist. The height of the secondary recirculation (smaller) in the exit module of the channel decreases as the Darcy number increases. These two observations are in agreement with theoretical assumptions that as the Darcy

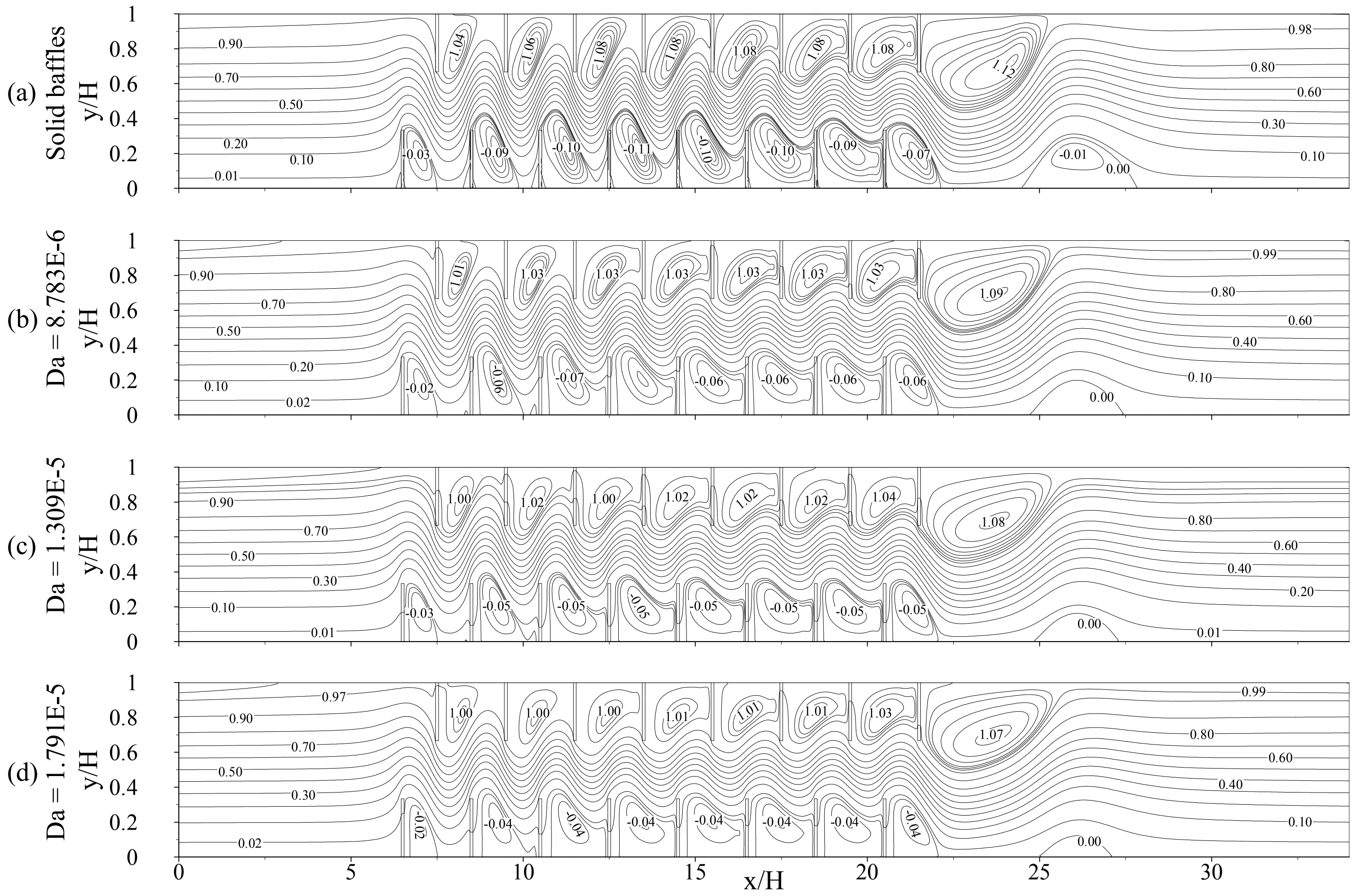

Fig. 6.12 Effects of Darcy number on the non-dimensional stream function Ψ^* Re = 400, H/w = 12, d/w = 11, b/w = 4: (a) Solid Baffles (Da = 0), (b) Da = 8.783E-6, (c) Da = 1.309E-5, and (d) Da = 1.791E-5

number increases the velocity profile of the flow in the channel should take the shape of the velocity profile for a flow in a two-dimensional parallel plate channel with no baffles. In the cavities for the porous baffles the streamlines are fairly similar in shape (see Figures 6.12b, 6.12c, and 6.12d) but are considerably different from the case of the solid baffles (see Figure 6.12a). In Figure 6.12a for the solid baffles case the streamlines in the cavity are steeper and crowded closer to the downstream vertical side of the solid baffles. This is to be expected, as solid baffles are impervious to the fluid, which results in the recirculation not being blown farther downstream of the vertical side of the baffle. It was found in Figure 6.12 that the height of vortices in the cavity regions gradually decreases, as the Darcy number increases from 0 to 1.791E-5; observe the gradual reduction in the height of the small secondary recirculation in the exit module of the channel. This occurs because as the length of the recirculation increases the height of the recirculation decreases to preserve mass balance.

Table 6.3 The minimum and the maximum non-dimensional stream function Ψ^* values for varying non-dimensional baffle Spacing (d/w) Da = 1.791E-6, H/w = 12, Re = 400, b/w = 4

d/w	$\mathbf{\Psi^*_{min}}$	$\mathbf{\Psi^*_{max}}$
11	-0.041195	1.07491
13	-0.058947	1.04658
15	-0.064003	1.04685

Table 6.4 The minimum and the maximum non-dimensional stream function Ψ^* values for varying baffle aspect ratio (H/w) Da = 1.791E-6, Re = 400

H/w	Ψ^*_{min}	Ψ^*_{max}
12	-0.041950	1.07491
6	-0.064558	1.06090
4	-0.064304	1.04457

6.8 Effects of Non-Dimensional Baffle Spacing (d/w) on the Streamlines

Table 6.3 lists the minimum and the maximum values of the non-dimensional stream function Ψ^* values in Figure 6.13. Figure 6.13 is a representative figure to determine the variation of non-dimensional stream function Ψ^* for Re = 400, H/w = 12, Da = 1.791E-5, b/w = 4, with baffle spacing d/w = 11, 13, and 15. Before discussing Figure 6.13 it is important to mention that Figure 6.13b and 6.13c show only the partial exit module, as can be observed by the missing solid line at the channel exit unlike Figure 6.13a which shows the whole geometry. This truncation does not have any implications for the representative results as the elliptic effects in Figure 6.13 are adequately represented. In Figure 6.13a (d/w = 11) the recirculation zones completely occupy the cavities, this in turn stops the flow in the core from coming into contact with the lower or upper walls of the channel between the baffles. These large vortices adversely affect heat transfer at the top and bottom walls of the channel. This is because heat transfer takes place only by diffusion (conduction) through the layers of fluid between the vortices and the core. Higher heat transfer coefficients are associated in heat

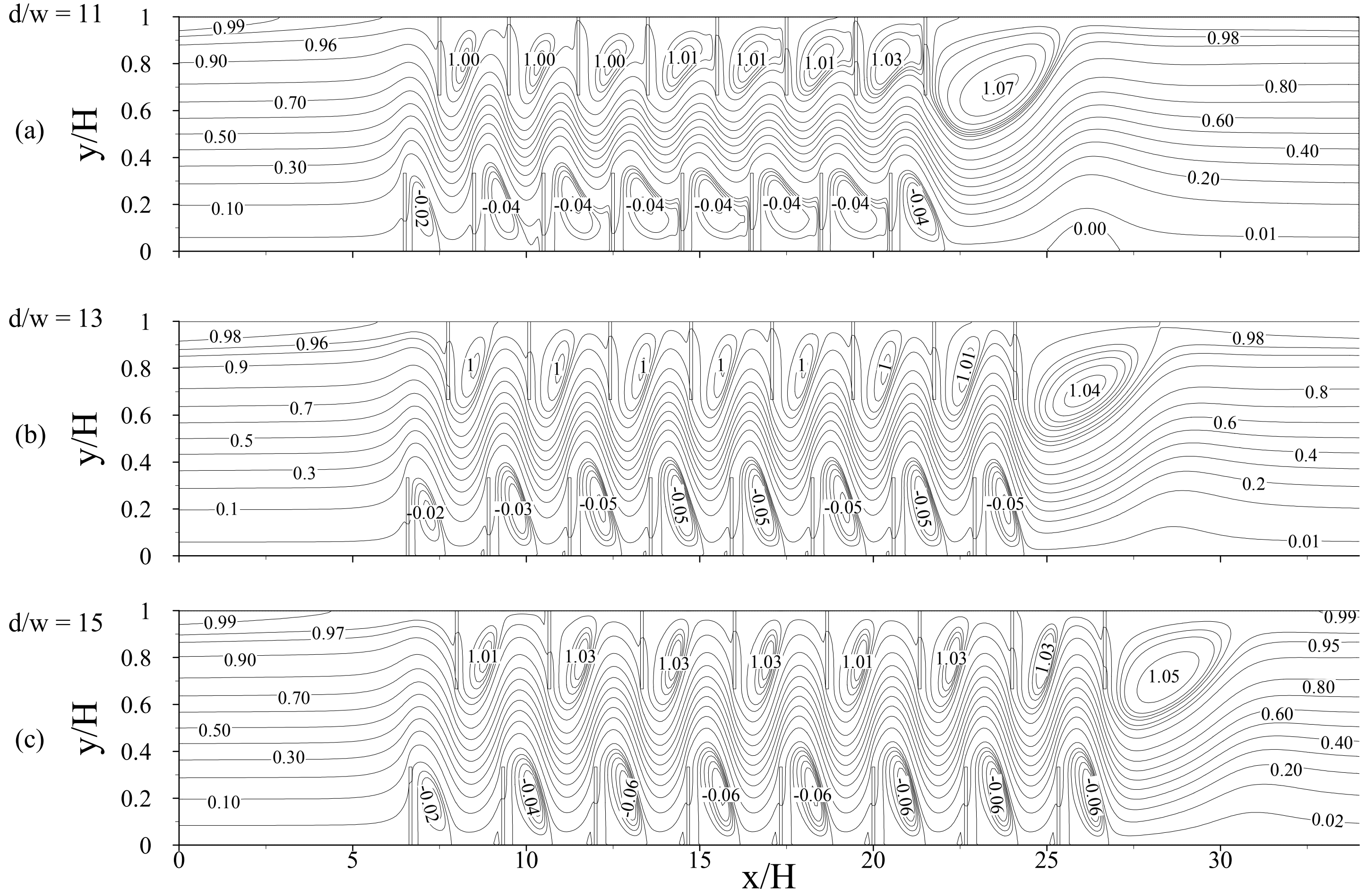

Fig. 6.13 Effects of non-dimensional baffle spacing (d/w) on the non-dimensional stream function Ψ* Da = 1.791E-6, H/w = 12, Re = 400, b/w = 4: (a) d/w = 11, (b) d/w = 13, and (c) d/w = 15

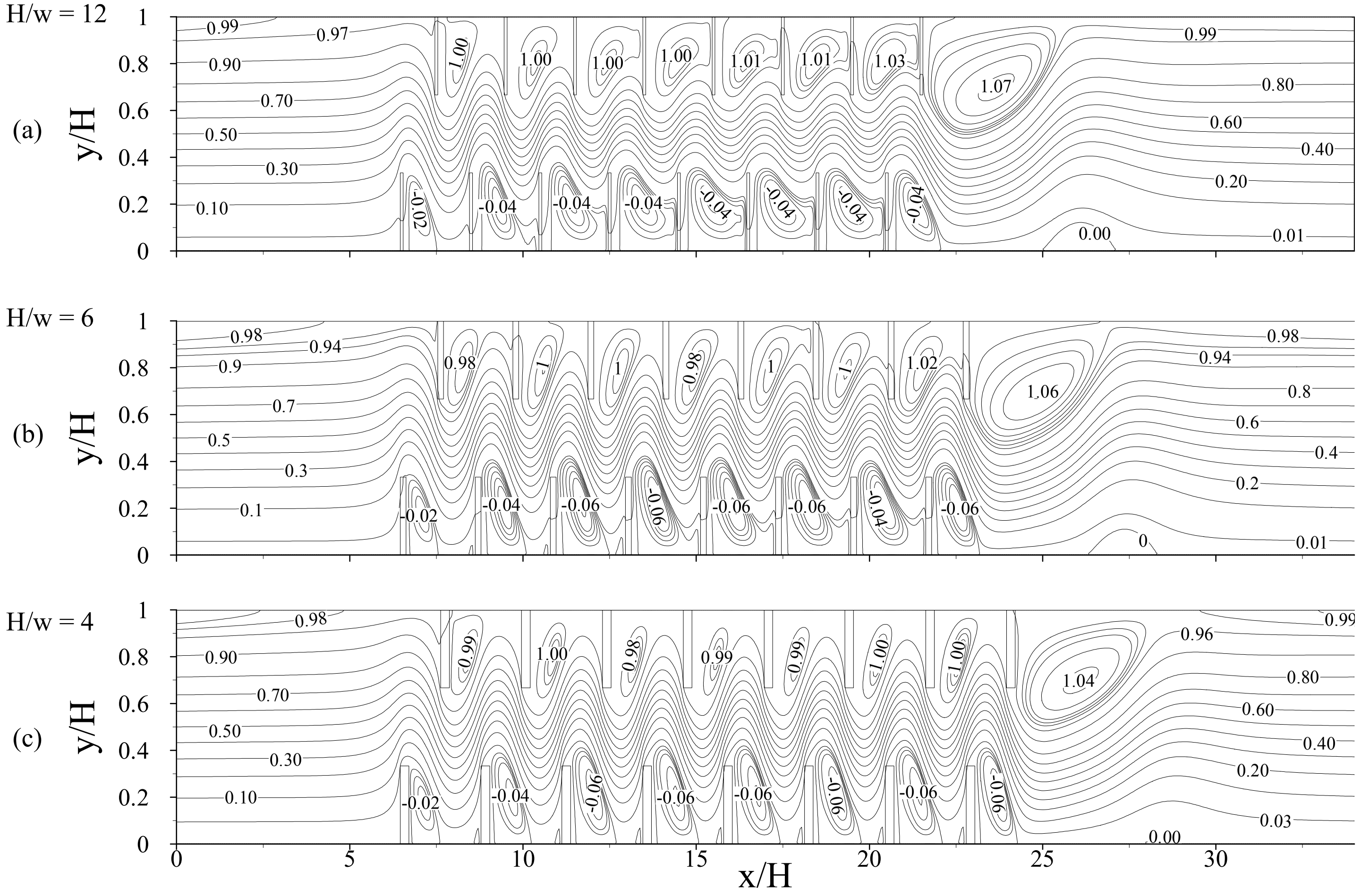

Fig. 6.14 Effects of varying baffle aspect ratio (H/w) on the non-dimensional stream function Ψ* Da = 1.791E-6, Re = 400: (a) H/w = 12, d/w = 11, b/w = 4 (b) H/w = 6, d/w = 11/2, b/w = 2 c) H/w = 4, d/w = 11/3, b/w = 4/3

transfer flows where convection is the dominant means of heat transport as opposed to diffusion (conduction). In addition, impinging of flow on heated surfaces also produces desirable effects on the heat transfer. From Figure 6.13b (d/w = 13) it can be seen that the recirculation does not fully occupy the cavities as the non-dimensional baffle spacing

transfer flows where convection is the dominant means of heat transport as opposed to diffusion (conduction). In addition, impinging of flow on heated surfaces also produces desirable effects on the heat transfer. From Figure 6.13b (d/w = 13) it can be seen that the recirculation does not fully occupy the cavities as the non-dimensional baffle spacing

(d/w) increases. While the recirculation height increases as the baffle spacing increases, this increase in height, causes the flow in the core to deflect into the cavities and impinge upon the lower or upper wall between adjacent baffles, depending on the location of the recirculation. In addition, the secondary recirculation (along the bottom wall) in the exit module of the channel disappears. In Figure 6.13c (d/w = 15) the streamlines variation is almost like those in the Figure 6.13b (d/w = 13), this is probably because in the d/w = 13 case the baffle spacing is sufficiently large enough to isolate the individual baffles from their neighbors and a further increase in the baffle spacing to d/w = 15 does not cause drastic changes to the streamlines.

6.9 Effects of Baffle Aspect Ratio (H/w) on the Streamlines

Table 6.4 lists the minimum and the maximum values of the non-dimensional stream function Ψ^* for the case shown in Figure 6.14. Figure 6.14 is a representative figure of the non-dimensional stream function Ψ^* for Re = 400, Da = 1.791E-5, for varying baffle aspect ratios H/w = 12, 6, and 4. Figures 6.14b and 6.14c show only the partial exit module, as can be observed by the missing solid line at the channel exit unlike Figure 6.14a which shows the whole geometry. In the exit module of the channel the intensity of the larger recirculation decreases form 1.07 to 1.04 while the secondary recirculation (along the bottom wall) disappears as the baffle aspect ratio decreases. For the baffle aspect ratio H/w = 12, d/w= 11, b/w = 4 case (Figure 6.14a) the recirculation in the cavity region occupies the whole cavity preventing the flow in the core from coming into contact with the bottom or top wall between the adjacent baffles. As the baffle aspect ratio H/w reduces, the baffles become thicker; this thickening of the baffles results in a decrease of flow through the baffles, this can be seen in Figures 6.14b and 6.14c where the streamlines are crowded closer to the downstream vertical side of the baffles. It can also been seen that the height of the recirculation increases with the decrease in the baffle aspect ratio. The net effect of this is that the fluid from the core region is deflected by the tall recirculation into the cavities and the fluid can be clearly seen to impinge on the lower and upper walls as shown in Figure 6.14c. It should be noted that the baffle spacing and height remain constant for all cases in Figure 6.14. Therefore, the increase in the recirculation height has to be explained. Although, it cannot be clearly seen in Figure 6.14 there is a blowing effect caused by fluid flowing through the horizontal surface (free end) of the baffles and this is caused because the fluid that enters the porous baffle faces greater resistance in the stream-wise direction it does flowing in the transverse direction (perpendicular to the stream-wise flow) as the baffle thickness increases. In turn this blowing effect causes the recirculation height to increase.

6.10 Calculation of Average Nusselt Number Ratio

After obtaining the converged solution for velocities and temperature the local Nusselt number along the lower and upper walls of the parallel plate channel was calculated by using the following relationship:

$$Nu_x = \frac{2H}{\left(T_w - T_b\right)} \frac{\partial T}{\partial y}\bigg|_{y=0 \text{ or } y=H} \tag{6.4}$$

$$Nu_x = \frac{2Hk_{eff}}{k_f\left(T_w - T_b\right)} \frac{\partial T}{\partial y}\bigg|_{y=0 \text{ or } y=H} \tag{6.5}$$

In Equations 6.4 and 6.5, H is the height of the channel, k_{eff} is the effective thermal conductivity of the porous matrix, k_f is the thermal conductivity of the fluid, T_w is the temperature of the wall, T_b is the bulk temperature of the fluid defined as:

$$T_b = \frac{\int_0^H |u| T dy}{\int_0^H |u| dy} \tag{6.6}$$

Equation 6.4 was considered when dealing with regions having no porous material attached to the lower or upper walls of the channel, while Equation 6.5 was considered for regions having porous attachments on the lower and upper walls. In essence Equation 6.4 can be obtained from Equation 6.5, by assuming $k_{eff} = k_f$ in regions having no porous material attached to the lower or upper walls of the channel. In the developed code, Equation 6.5 was used. The harmonic mean was used to calculate the thermal conductivity at the fluid-porous interface. Having calculated the local Nusselt number along the lower and upper walls of the channel the average Nusselt number for the lower and upper walls of the entrance module, the eight modules, and exit module was calculated by using:

$$\overline{Nu} = \frac{1}{(b-a)} \int_a^b Nu_x dx \tag{6.7}$$

Where the limits "a" and "b" of the integral are the location along the x-axis demarking the starting and the ending of the module, respectively. Now the average Nusselt number along the lower and upper wall of each module is different because of the way in which the baffles were arranged. Therefore, the average Nusselt number for a module was defined to be:

$$\overline{Nu_{ave}} = \frac{\overline{Nu_{lower}} + \overline{Nu_{upper}}}{2} \tag{6.8}$$

This average Nusselt number was then further normalized by dividing it by the Nusselt number (Nu_o) that would have been obtained for fully developed flow and heat transfer from the study of a parallel plate channel. The value of Nu_o was taken to be 8.235 (Mills [13]). In the following discussion on the various effects on the Nusselt number the definition $\overline{Nu_{ave}}/Nu_o$ has been used to illustrate the results.

6.11 The Local Nusselt Number Along the Lower and Upper Wall of the Channel

As discussed in Section 6.10 the local Nusselt number calculation was computed only along the lower and upper wall of the channel. This computation did not take into consideration the fluid/porous interface surface of the porous baffle. Now, Figure 6.15 is a representative plot of the local Nusselt number Nu_x along the lower and upper wall of the channel for Da = 1.791E-5, H/w = 12, d/w = 11, b/w = 4, K = 100 and Re = 400. At the entrance of the channel the local Nusselt numbers are very large. The local Nusselt number then asymptotically decreases until it reaches the vicinity of the first porous baffle. This happens because the rate of heat transfer becomes retarded with the development of the hydrodynamic and thermal boundary layers. In the first three modules the local Nusselt number increases but does not attain its highest values because the flow is developing in this region. Then, from the fourth to the seventh module the local Nusselt number attains its highest values and stays fairly constant. This is because the flow approaches a periodically developed state. This was concluded by using Figure 6.12 and noticing the constant heights of the peaks of the local Nusselt number for those modules. In the eighth module the height of the peak decreases because the flow is disrupted by the sudden expansion of the fluid. Finally, in the exit region the local Nusselt number has a relatively shorter but wider peak. This is because the recirculations that appear in the exit module are caused by the sudden expansion of the flow after the eighth module.

6.12 Effects of Reynolds Number on the Average Nusselt Number Ratio

Figure 6.16 is a representative figure of the average Nusselt number ratio $\overline{Nu_{ave}} / Nu_o$ for varying Reynolds numbers for Da = 1.791E-5, H/w = 12, d/w = 11, b/w = 4, K = 100.

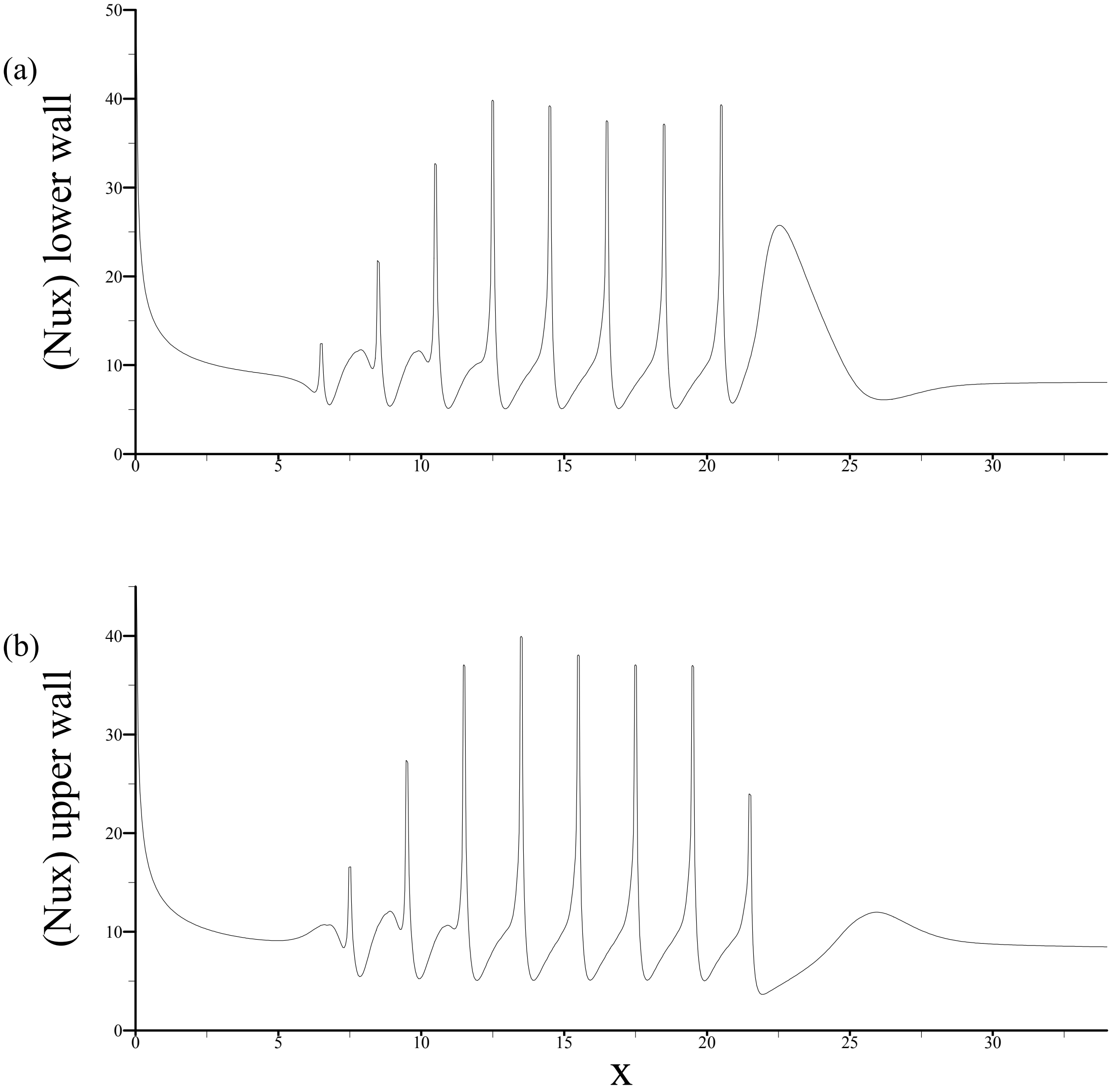

Fig. 6.15 The profile of the local Nusselt number with Da = 1.791E-5, H/w = 12, d/w = 11, b/w = 4, K = 100, Re = 400 along: a) lower wall, b) upper wall

An examination of this figure would establish that for all the cases of Reynolds numbers the solid baffles yield higher $\overline{Nu_{ave}}/Nu_o$ values for all the modules. For Re = 100 the

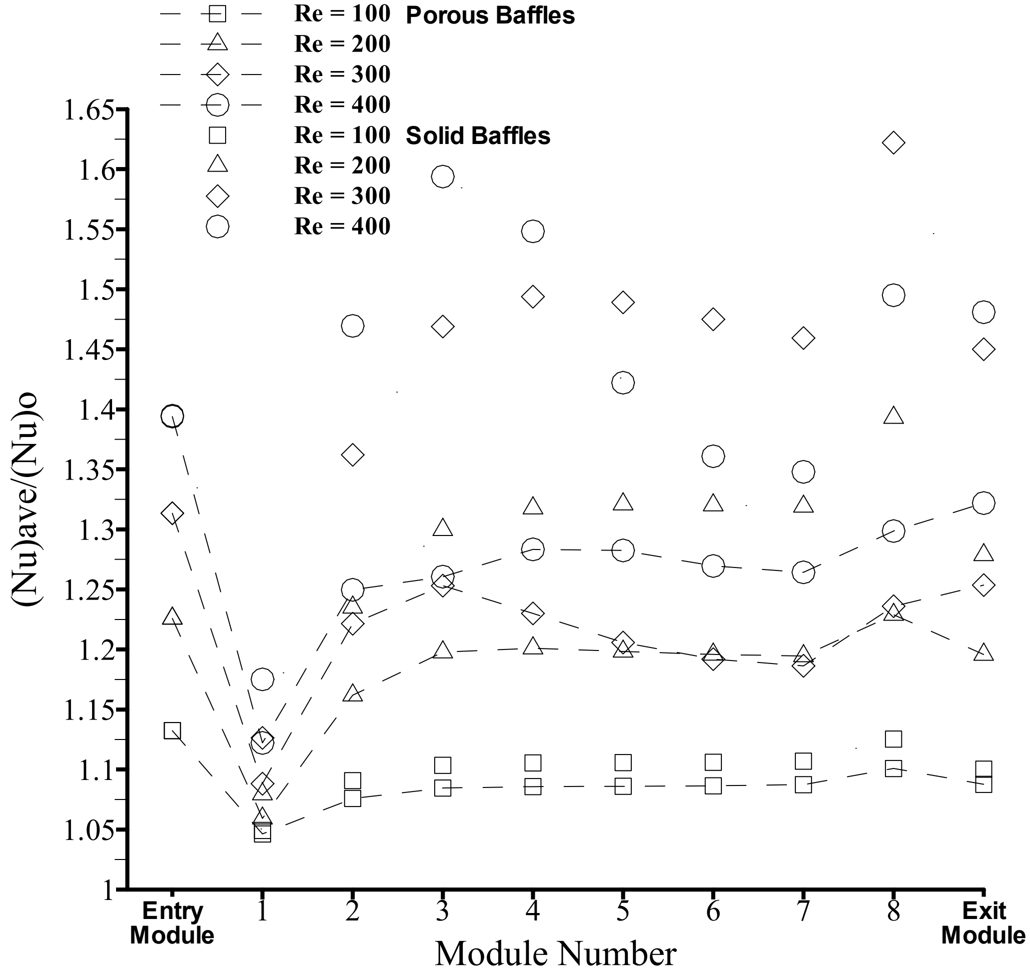

Fig. 6.16 Effects of Reynolds number on the average Nusselt number ratio Da = 1.791E-5, H/w = 12, d/w = 11, b/w = 4, K = 100

$\overline{Nu_{ave}}/Nu_o$ ratio for the solid baffles is about 1.1 which is slightly larger than that obtained by the use of porous baffles 1.09. The Re = 100 case has the least divergence between the two plots as can be observed in Figure 6.16 by the close proximity of the two plots. For Re = 200 the trend of the plots is identical to that observed for Re = 100.

However, the two plots diverge from each other the value of $\overline{Nu_{ave}}/Nu_o$ for the porous baffles is close to 1.2 while that for the solid baffles is 1.3. For Re = 300 there is distinct deviation from the general trend for the case of porous baffles, while for the solid baffles the trend continues in line with Re = 100 and Re = 200. To better understand why this change occurs it would be helpful to refer to Figure 6.11c. A comparison of this figure with Figures 6.11a and 6.11b would reveal that the recirculation in the cavities appears to occupy the whole cavity, thereby preventing fluid in the core from coming in contact with the heating wall in the cavities downstream of the third module. The formation of a large recirculation which occupies the entire cavity downstream of the third module coincides with the sharp drop in the average Nusselt number ratio. This is because regions of recirculation that covers large heating surfaces, are known to be associated with poor Nusselt numbers (poor heat transfer). This is because conduction is the dominant means by which heat transfer occurs between the layers of fluid in the recirculation and the layers of fluid in the core. Convection dominant heat transfers are known to be associated with higher Nusselt numbers like the cases shown in Figures 6.11a and 6.11b. Also, it should be noted that the average Nusselt number ratio for the exit module is higher than that for the 8th module for Re = 300. This occurs because a secondary recirculation along the bottom wall is probably beginning to form in the exit module as can be seen by comparing Figures 6.11c to Figure 6.11b. This secondary recirculation is likely to cause the fluid in the exit module to impinge on the upper wall causing an increase in the heat transfer. For Re = 400, the plot for the porous baffles regains the general trend observed for Re = 100 and Re = 200, the only discrepancy being the higher average Nusselt number ratio for the exit module. This is due to the secondary recirculation that occurs in the exit module which can be clearly seen in Figure 6.11d. In contrast to the solid baffles when Re = 400, there is a large deviation from the general trend. In order to understand this trend it would be helpful to refer to Figure 6.12a. A close examination of Figure 6.12a reveals that the recirculation in the cavities downstream of the third module occupies the whole cavity; this is similar to the phenomenon observed for the porous baffles with Re = 300. In this case the average Nusselt number for the exit module is only slightly less than that for the eighth module. Now comes the important question why do the porous baffles deviate at lower Re values (Re = 300) from the general trend? The porous baffles due to the through-flow cause the recirculation downstream of the vertical surface of the baffles to be blown farther downstream. This results in complete occupation of the cavity regions at lower Re values.

6.13 Effects of Darcy Number on the Average Nusselt Number Ratio

Figure 6.17 is a representative figure of the average Nusselt number ratio $\overline{Nu_{ave}}/Nu_o$ for varying Darcy numbers with Re = 400, H/w = 12, d/w = 11, b/w = 4, K = 100. An examination of this figure would establish that for all the cases of Reynolds numbers the solid baffles yield higher $\overline{Nu_{ave}}/Nu_o$ values for all the modules. The lowest average Nusselt numbers was found to be associated with Da = 1.791E-5. The average Nusselt numbers were shown to increase with decreasing Darcy numbers, attaining

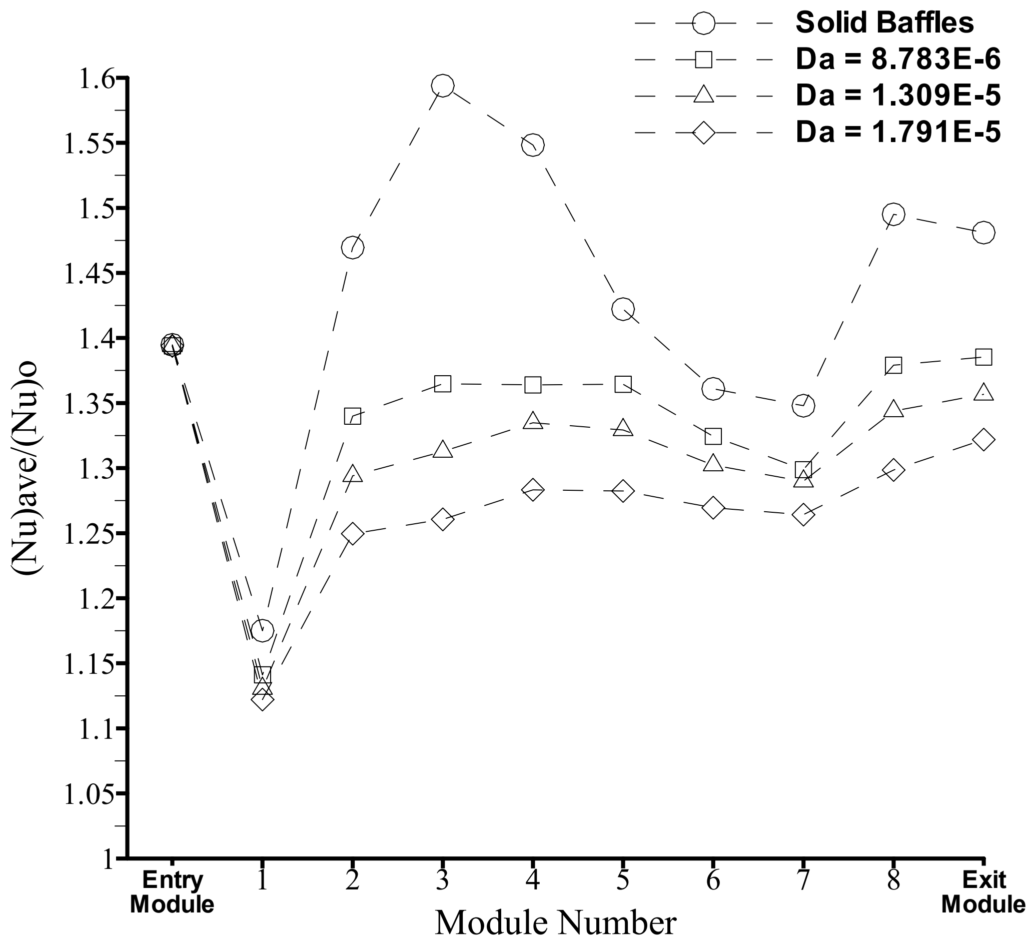

Fig. 6.17 Effects of Darcy number on the average Nusselt number ratio Re = 400, H/w = 12, d/w = 11, b/w = 4, K = 100

maximum values for the solid baffles. Theoretically porous baffles should yield average Nusselt numbers between the two, limiting the conditions of a parallel plate channel with no baffles (Da $\rightarrow \infty$) and a parallel plate channel with solid baffles (Da = 0). Average Nusselt number $\left(\overline{Nu_{ave}} / Nu_o \right)$ plots for flows with large Darcy numbers should resemble that which could be obtained from the use of a parallel plate channel without porous baffles. While low Darcy numbers should resemble the average Nusselt number plots for the solid baffles. This can be seen in Figure 6.17 as the lowest Darcy number yields the largest average Nusselt number ratio. Another trend that can be observed in Figure 6.17 is that variations in Darcy numbers produces similar trends while the solid baffles do not exhibit the same trends as the porous baffles. This, as mentioned in Section 6.11, probably happens because the porous baffles have already passed the stage of partial occupation of the heating wall in the cavity regions at Re = 300. At Re = 400 the recirculation in the cavity fully occupies the heating surface in the cavity, this however, is not the case for the solid baffles as this transition from the partial occupation of the heating wall to the total occupation happens around Re = 400. This is why the average Nusselt number sharply drops downstream of the third module for the solid baffles. Another interesting fact is the apparent higher $\overline{Nu_{ave}}/Nu_o$ values for the exit module compared to the corresponding eighth module. This seems to indicate that a secondary recirculation along the bottom wall in the exit module is about to form or has formed. There is a sharp drop in the average Nusselt number ratio from the entrance module to the first module as shown in Figure 6.17. This phenomenon can be explained by realizing that at the entrance of the channel the heat transfer rates are very high because of the developing thermal boundary layer. However, farther downstream of the entrance, the hydrodynamic and thermal boundary layers become developed. This development of the thermal boundary hinders the heating process. This is the reason why solid baffles and porous baffles are often used to disrupt this development, in turn this introduction of baffles artificially creates an array of entrance lengths each associated with higher heat transfer.

6.14 Effects of Non-Dimensional Baffle Spacing (d/w) on the Average Nusselt Number Ratio

Figure 6.18 is a representative figure of the average Nusselt number ratio $\overline{Nu_{ave}}/Nu_o$ for varying non-dimensional baffle spacing (d/w) for Da = 1.791E-6, H/w = 12, Re = 400, b/w = 4, and K = 100. An examination of this figure would establish that as the non-dimensional baffle spacing (d/w) decreases the average Nusselt number ratio also decreases. For the d/w = 11 baffle spacing case it should be noted that the average Nusselt number ratio for the exit module is higher than that for the eighth module. This suggests that there is a secondary recirculation along the bottom wall in the exit module region. This secondary recirculation can also be seen clearly in Figure 6.13a. The association of low average Nusselt number ratio values with d/w = 11 can be explained by referring to Figure 6.13a. In this figure the recirculation in the cavity occupies the whole cavity and in doing so the heating surface in the cavity is completely isolated from contact with the fluid in the core region. Thus, conduction is the dominant means by which heat transfer takes place between the fluid layers in the recirculation and the fluid layers in the core. However, it should be noted that at the heating surface, heat transfer takes place by means of convection and diffusion; but, due to the recirculation this heat gain is localized and can only be dissipated to the flow in the core by conduction. For baffle spacing d/w = 13 the average Nusselt numbers are higher than d/w = 11 with the

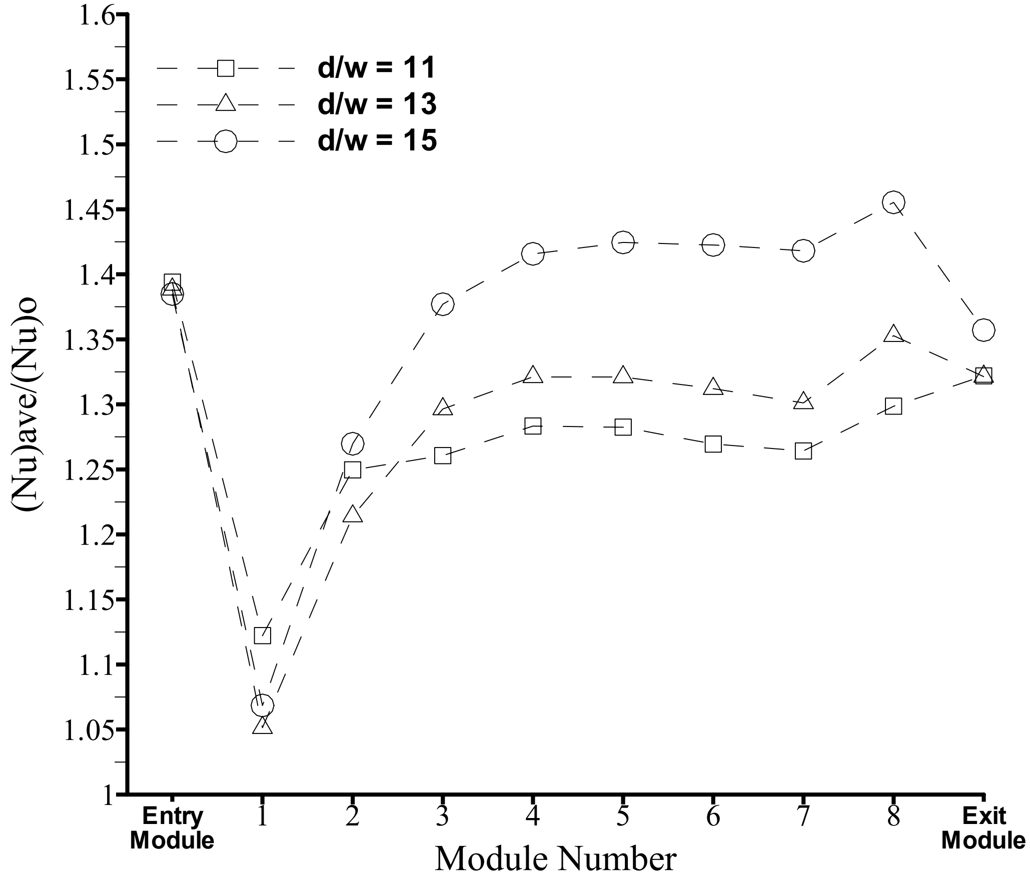

Fig. 6.18 Effects of non-dimensional baffle spacing (d/w) on the average Nusselt number ratio Da = 1.791E-6, H/w = 12, Re = 400, b/w = 4, K = 100

exception of the second module which has lower values. The exit module for this case is less then the 8th module this would indicate the lack of a secondary recirculation in the exit module as can be clearly seen in Figure 6.13b. In this figure it can also be seen that the recirculation in the cavity region does not occupy the whole cavity, this translates to a higher average Nusselt number ratio $\overline{Nu_{ave}}/Nu_o$ as can be seen in Figure 6.18. For baffle spacing d/w = 15, the highest $\overline{Nu_{ave}}/Nu_o$ were achieved as seen in Figure 6.18. A reference to Figure 6.13c is needed to explain these sharp gains. An examination of this figure reveals that the recirculation behind the vertical surface downstream of the baffles does not interact with the baffle downstream of the recirculation. In fact a close examination will reveal that a small secondary recirculation in front of the baffles is beginning to form. As the baffle spacing progressively gets larger it should be expected that the fluid from the core will encroach into the cavity region. This encroaching into the cavity in turn will result in a decrease in the maximum velocity in the core flow to preserve mass balance. When the baffle spacing is large (e.g. d/w = 15) to allow fluid from the core to impinge on the heating surface between the baffles, the fluid that is heated by the heating surface is carried back into the core. This is clearly a convection dominant heat transfer system therefore it should not come as a surprise that the highest average number ratios are associated with d/w = 15.

6.15 Effects of Varying Baffle Aspect Ratio (H/w) on the Average Nusselt Number Ratio

Figure 6.19 is a representative figure of the average Nusselt number ratio $\overline{Nu_{ave}}/Nu_o$ for varying baffle aspect ratios (H/w) for Da = 1.791E-6, Re = 400, and K = 100. An examination of this figure would establish that as the baffle aspect ratio (H/w) decreases the average Nusselt number ratio increases. H/w = 4 being the thickest baffle and H/w = 12 being the thinnest baffle case considered. Although, it may seem to the

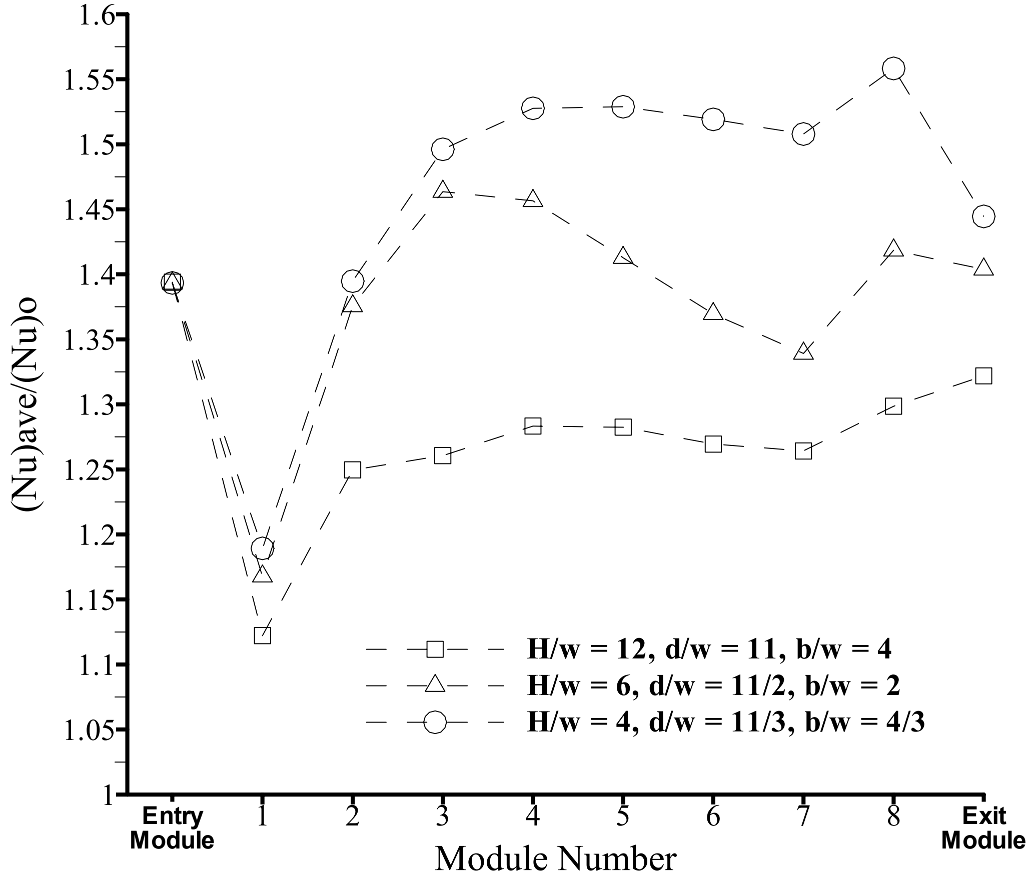

Fig. 6.19 Effects of varying baffle aspect ratios (H/w) on the average Nusselt number ratio Da = 1.791E-6, Re = 400, K = 100

reader that the baffle spacing (d) and the baffle height (b) have been varied, in Figure 6.19 the baffle height (b) and the baffle spacing (d) are held constant and the dimensional parameters have been made non-dimensional by using the baffle width (w), A close examination of Figure 6.19 shows that the thinnest baffle H/w = 12, d/w = 11, b/w = 4, yields the lowest average Nusselt number ratios with the exit module having a higher average Nusselt number than the 8th module. The reason why this occurs is because the thinnest porous baffle offers the least resistance to fluid flow through the porous baffles. This causes the recirculation downstream of the vertical surface of the baffle to be blown farther away from the baffle. Due to this the recirculation occupies the whole cavity as can be seen in Figure 6.14a; in this figure the secondary recirculation in the exit module can also be seen. The covering of the heating surface by the long recirculation, occupying the cavity, results in a conduction dominant heat transfer system. Heat can only be dissipated to the flow in the core region by conduction through the fluid layers in the recirculation and the fluid layers in the core region. For the intermediate baffle thickness values H/w = 6, d/w = 11/2, b/w = 2 considered for this study the trend of the average Nusselt number ratio is drastically altered. This can be explained by comparing Figures 6.14a and 6.14b, a first glance at these figures reveals that the recirculation in the first three modules in Figure 6.14b partially occupies the cavity in addition to this it can be seen that a small recirculation appears in front of the baffle. It can be seen that the height of the recirculation in Figure 6.14b is greater than in Figure 6.14a. To understand why this occurs, it is important to understand the mechanics of the fluid flow through the porous baffles. As the porous baffles become thicker the resistance to the fluid increases in the stream-wise direction. Fluid that enters the porous baffle from the vertical side of the porous baffle has to satisfy the mass balance principle but since it faces stiff resistance (with increasing baffle thickness) in the stream-wise direction the fluid squeezes itself out from the horizontal end (free end) of the porous baffle. This free end is also a boundary of the core region and the fluid that squirts through this surface into the core region has the effect of nudging the flow in the core region. This deflection of flow results in the flow impinging on the heating surface directly above or below the free end depending on the baffle location. For the baffle aspect ratio H/w = 6 some fluid does get through the porous baffles after the third module Figure 6.14b. For the thickest baffle H/w = 4, d/w = 11/3, b/w = 4/3 the porous baffles are sufficiently thick so as to considerably reduce fluid flow through the baffles. The net effect of this and the blowing effects through the horizontal surface on the free end of the baffles is that the recirculation in all the cavities partially occupy the cavity and are also taller then those in Figure 6.14a. Now that the flow in the core is deflected and impinges on the heating surface between the baffles the Nusselt number ratio shoots up because the dominant means by which heat transfer occurs is convection. Thus, the average Nusselt number ratios for this case are very high. It should also be noted that $\overline{Nu_{ave}} / Nu_o$ for the exit module is lower than that for the 8th module and coincides with the disappearance of the secondary recirculation in the exit module.

6.16 Effects of Varying the Thermal Conductivity Ratio K on the Average Nusselt Number Ratio

Figure 6.20 is a representative figure of the average Nusselt number ratio $\overline{Nu_{ave}} / Nu_o$ for varying thermal conductivity ratio K with Da = 1.791E-6, H/w = 12, Re = 400, and b/w = 4. Examination of this figure would establish that as the thermal conductivity ratio K decreases the average Nusselt number ratio also decreases. The

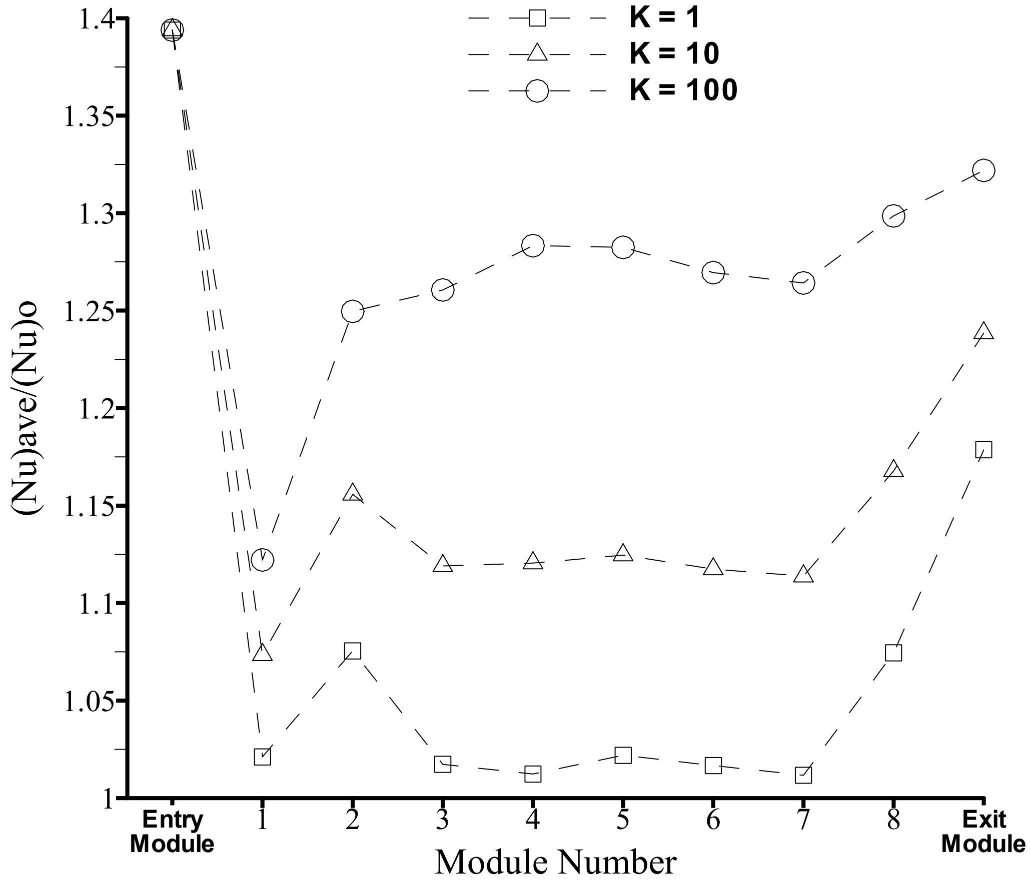

Fig. 6.20 Effects of varying the thermal conductivity ratio K on the average Nusselt number ratio Da = 1.791E-5, Re = 400, H/w = 12, d/w = 11, b/w = 4

$\overline{Nu_{ave}}/Nu_o$ plots for K = 1 and K = 10 reveals similar trends, with a noticeable increase for K = 10, however for K = 100 this trend is not preserved. For K = 100 the values of the average Nusselt number downstream of the 2nd module are higher than those for the 2nd module. This is understandable because with higher thermal conductivity ratios the porous baffle should exhibit very little variation in the temperature. Fluid in the cavity regions transports heat by the through flow. The fluid that flow through the porous baffles even though small is considerably heated because of the large thermal conductivity ratio. A part of this hot fluid flows into the core region and the rest flows into the recirculation region. It is quite plausible that some of the fluid does reach the core flow because the recirculation downstream of the vertical surface of the porous baffle whipsthe fluid (by shearing fluid layers) into the core region. Thus the average Nusselt number ratio for K = 100 downstream of the 2^{nd} module are typically larger. A close examination of Figure 6.20 reveals that for the 8th module and the exit module the average Nusselt number increases, while the interior modules yield fairly constant and lower average Nusselt number ratios. The reason this occurs is because the thinnest porous baffle was used to create Figure 6.20 i.e., H/w = 12, d/w = 11, b/w = 4. Because of this the porous baffle offers the least resistance to fluid flow through it. This causes the recirculation downstream of the vertical surface of the baffle to be blown farther away from the baffle. Due to this, the recirculation occupies the whole cavity as can be seen in Figure 6.14a; in this figure the secondary recirculation in the exit module can also be seen.

6.17 Calculation of the Darcy Friction Factor Ratio

After obtaining the converged solution for velocities and temperature the average pressure at the entrance and the exit of the channel was calculated by:

$$\bar{p} = \left. \frac{\int_0^H p\,dy}{\int_0^H dy} \right|_{x=0 \text{ or } L} \tag{6.9}$$

Now, the Darcy friction factor for the whole channel is defined as:

$$f = \frac{\bar{p}(0,y) - \bar{p}(L,y)}{L} \frac{2H}{\rho u_{bulk}^2 / 2} \tag{6.10}$$

In Equation 6.10 f is the Darcy friction factor, H is the height of the channel, L is the length of the channel, ρ is the density and the terms $\bar{p}(0,y)$ and $\bar{p}(L,y)$ were evaluated using Equation 6.9. The bulk velocity of the channel was evaluated at the entrance of the channel using:

$$u_{bulk} = \left. \frac{\int_0^H u\,dy}{\int_0^H dy} \right|_{x=0} \tag{6.11}$$

Now the analytical solution yields a relationship between the Reynolds (hydraulic diameter) and the Fanning coefficient of friction c_f for fully developed flow in a circular-tube annuli. When the ratio of the radii of the internal tube to the external tube approaches one this relation is [16]:

$$c_f \operatorname{Re}_H = 24 \tag{6.12}$$

However, the Fanning coefficient of friction c_f is also related to the Darcy friction factor for fully developed flow f_0 by:

$$4c_f = f_0 \tag{6.13}$$

Now using Equations 6.10, 6.12, and 6.13 to obtain the Darcy friction factor ratio:

$$\frac{f}{f_0} = \frac{\bar{p}(0,y) - \bar{p}(L,y)}{L} \frac{2H}{\rho u_{bulk}^2 / 2} \frac{\mathrm{Re}_H}{96} \tag{6.14}$$

6.18 Heat Transfer Performance Ratio

Tables 6.5 to 6.9 lists various parameters and their influence on the heat transfer performance ratio. Heat transfer performance ratio is the ratio of increase in heat transfer to the unit increase in pumping power. The numerator of the ratio represents the ratio of the average Nusselt number for the channel with porous baffles to the Nusselt number

Table 6.5 Effects of Reynolds number on heat transfer performance ratio H/w = 12, d/w = 11, b/w = 4, K = 100

Re	$\left(\frac{Nu_{ave}}{Nu_o}\right) \Big/ \left[\frac{f}{(f)_o}\right]^{1/3}$ Da = 1.791E-5	$\left(\frac{Nu_{ave}}{Nu_o}\right) \Big/ \left[\frac{f}{(f)_o}\right]^{1/3}$ solid baffles
100	0.7676	0.7663
200	0.7110	0.7303
300	0.6696	0.7108
400	0.6642	0.6633

Table 6.6 Effects of Darcy number on heat transfer performance ratio Re = 400, H/w = 12, d/w = 11, b/w = 4, K = 100

Da	$\frac{Nu_{ave}}{Nu_o} \Big/ \left[\frac{f}{(f)_o}\right]^{1/3}$
Solid baffles	0.6633
8.783E-6	0.6697
1.309E-6	0.6686
1.791E-5	0.6642

Table 6.7 Effects of non-dimensional baffle spacing (d/w) on heat transfer performance ratio Da = 1.791E-5, H/w = 12, Re = 400, b/w = 4, K = 100

d/w	$\frac{Nu_{ave}}{Nu_o} \Big/ \left[\frac{f}{(f)_o}\right]^{1/3}$
11	0.6642
13	0.7204
15	0.7783

Table 6.8 Effects of varying baffle aspect ratio (H/w) on heat transfer performance ratio Da = 1.791E-5, Re = 400, K = 100

H/w =, d/w = , b/w =	$\frac{Nu_{ave}}{Nu_o} \Big/ \left[\frac{f}{(f)_o}\right]^{1/3}$
12, 11, 4	0.6642
6, 11/2, 2	0.6939
4, 11/3, 4/3	0.7436

Table 6.9 Effects of varying the thermal conductivity ratio K on heat transfer performance ratio Da = 1.791E-5, Re = 400, H/w = 12, d/w = 11, b/w = 4

K	$\frac{Nu_{ave}}{Nu_o} \Big/ \left[\frac{f}{(f)_o}\right]^{1/3}$ for porous baffles	$\frac{Nu_{ave}}{Nu_o} \Big/ \left[\frac{f}{(f)_o}\right]^{1/3}$ for solid baffles
1	0.6079	0.6192
10	0.6316	0.6399
100	0.6642	0.6633

for a fully developed flow in a corresponding channel. The denominator represents the ratio of the Darcy friction factor for the channel with porous baffles to the Darcy friction factor for the corresponding channel with no baffles. The friction factors are raised to one-third power as the pumping power is proportional to the one-third power of the friction factor. Ideally, one desires the heat transfer performance ratio to be greater than unity. As evident from Tables 6.5 – 6.8 this ratio is always less than one. Thus the proposed heat transfer enhancement strategy is not attractive from the pumping power point of view. However, the heat transfer enhancement ratio (Nu/No) was greater than unity for all the cases considered in this study. Accordingly, the proposed heat transfer enhancement strategy is very attractive for cases wherein pressure drop is not the main concern and is available in abundance (e.g. off-shore platforms and automobiles). For Re = 100 and Re = 400 in Table 6.5 the porous baffles yields higher heat transfer performance ratio. The heat transfer performance ratio for the porous baffles is better than those for the solid baffles, refer to Table 6.6. When the baffle spacing is increased the Nusselt number ratio is shown to increase which in turn results in gradual betterment of the average Nusselt number ratio as shown in Figure 6.18. When the baffle aspect ratio H/w is decreased the heat transfer performance ratio increases, a similar trend was observed for the average Nusselt number ratio as discussed earlier. The channel with porous baffles under-perform when compared to solid baffles for K = 1 and K = 10. Though for K = 100 the porous baffles slightly out perform the solid baffles.

6.19 Periodically Fully Developed Flow

Periodically fully developed flow (PDF) occurs in heat transfer problems that involve a repetition of geometric modules as in heat exchangers. Initially, there are considerable changes in the flow field and the heat transfer but farther downstream, away from the entrance effects, the flow field assumes periodicity this is where PDF conditions are said to exist. In most engineering applications involving heat transfer, PDF conditions are said to exist barring the entrance and exit regions. The heat transfer for periodically fully developed flow forms the lower bound, accordingly it provides good design information. Such information can be economically obtained by studying only a PDF module instead of the entire channel. In the developing flow problem, investigated in this study sixteen porous baffles in a staggered arrangement were used, see Figure 3.2. The sixteen porous baffles were arranged in a manner that produced 8 modules. The 8 module geometric setup used for this numerical study was sufficient to produce PDF like conditions away from the entrance and the exit module of the channel. The formation of a PDF like condition in this study (developing flow problem) can be observed to occur from the 3rd module until the 7th module (see Figure 6.17). The first two modules are affected by entrance effects (developing length) and the 8th module is affected by the exit effects due to a break in the continuation of the geometric module repetition. Note that this does not hold true when Re = 300 for the porous baffles and Re = 400 for the solid baffles. As those are two transitory phases that occur when the recirculation in the cavities shifts from a partial to a total occupation of the cavity regions.

CHAPTER VII

SUMMARY AND CONCLUSIONS

A detailed numerical study was conducted on flow and heat transfer in a 2-D parallel plate channel with 16 staggered porous baffles. The effects of the Reynolds number, Darcy number, non-dimensional baffle spacing (d/w), the baffle aspect ratio (H/w) and thermal conductivity ratio (K) on developing velocity profiles, streamlines, average Nusselt number ratio, and heat transfer performance ratio were examined.

In the course of this study it was found that there exists a transitory phase where the recirculation in the cavity regions switches from partial occupation to total occupation. During this switching phase the average Nusselt number ratio for both the porous baffles and the solid baffles encounters drastic changes in the general trends that were associated with these baffles. It was also found that this transitory phase occurs at Reynolds numbers lower than those typically associated with solid baffles. For Porous baffles this transitory phase occurs at around Re = 300 while for solid baffles it occurs at Re = 400.

For all the cases considered in this study the average Nusselt number ratios for the solid baffles were found to be higher than those for porous baffle simulations carried out and having the same geometric setup. The difference in the average Nusselt numbers ratios was found to be small for Re = 100, but progressively got larger reaching a maximum for Re = 300. It should be borne in mind that flows in porous baffles undergo transition from partial occupation of the cavity to full occupation of the cavities for Re = 300. Therefore, Re = 300 produces the maximum deviation between the results for the porous baffles and the solid baffles. For Re = 400 the difference in the average Nusselt number ratios, for solid baffles and porous baffles, is larger but the difference is not as large as that for Re = 300.

The heat transfer performance ratio for the solid baffles was found to be consistently below unity for both the solid baffles and the porous baffles. The heat transfer performance ratio was found to vary in the range of 0.62 – 0.77 for the solid baffles and 0.61 – 0.78 for the porous baffles. Porous baffles for Re = 100 and Re = 400 showed improvement over the solid baffle yielding higher heat transfer performance ratios.

Increasing the Darcy number from 8.783E-6 – 1.791E-5 was found to produce less desirable average Nusselt number ratios, this is because lower Darcy numbers exhibit properties closer to solid baffles as far as the average Nusselt number goes. This trend was also found to hold for the heat transfer performance ratio where lower Darcy numbers showed better performance.

An increase in the non-dimensional baffle spacing (d/w) and the baffle aspect ratio (H/w) were found to produce desirable effects on the average Nusselt number like in the case of large baffle spacing d/w = 15 and thick porous baffles H/w = 4. Because of the formation of large recirculation in the cavity regions it was desirable to have larger baffle spacing to isolate baffles from recirculation and to provide space for a convection dominated heat transfer to occur with a favorable outcome. Thicker porous baffles were found to produce blowing effects through the horizontal surface (free end) of the porous baffles, this through flow in turn resulted in a deflection of the flow in the core region into the cavity below or above depending on the position of the porous baffle. This also resulted in favorable heat transfer.

From this study it can be concluded that the porous baffles, perform better from a heat transfer point of view at larger baffle spacings (d/w), lower baffle aspect ratios (H/w), lower Darcy numbers (Da), and higher thermal conductivity ratios (K).

NOMENCLATURE

A = surface area

a = coefficients of discretization equation

B^* = non-dimensionless baffle height $\left({}^{\mathrm{b}}\!/_{\mathrm{H}} \right)$

b = baffle height (m)

b = source term

c_f = Fanning coefficient of friction

c_p = specific heat at constant pressure ${}^{\mathrm{J}}\!/_{(\mathrm{Kg} \cdot \mathrm{K})}$

D = diffusion

D^* = non-dimensionless baffle spacing $\left({}^{\mathrm{d}}\!/_{\mathrm{w}} \right)$

Da = Darcy number $\left({}^{K}\!/_{H^2} \right)$

d = baffle spacing (m)

dA = unit normal vector

d_p = pore diameter

dV = control volume element

F = Forchheimer coefficient (0.55)

F = convection

f = Darcy friction factor

f_0 = Darcy friction factor for fully developed flow

H = height of channel (m)

I = integer counter of grid lines

$\tilde{\boldsymbol{I}}$ = identity tensor

JPMAX = maximum number of grid lines in *y*-direction for pressure nodes

K = permeability of porous medium or thermal conductivity ratio $\left({k_e}\big/{k_f} \right)$

K^* = thermal conductivity ratio $\left({k_e}\big/{k_f} \right)$

k = thermal conductivity $\left({W}\big/{\left(m \cdot K^o\right)} \right)$

k_{eff} = effective thermal conductivity

k_f = thermal conductivity of the fluid

k_s = thermal conductivity of the solid

L = length of channel (m)

L1 = characteristic length, or total number of grid lines in the *x*-direction

L_1 = entry length of the channel

L_2 = exit length of the channel

L_3 = length of each module

Nu = Nusselt number

Nu_x = local Nusselt number

Nu_o = Nusselt number for fully developed flow in a parallel plate channel (8.235)

$\overline{Nu}$ = average Nusselt number

$\overline{Nu_{ave}}$ = average Nusselt number for a module

$\overline{Nu_{lower}}$ = average Nusselt number for lower wall of a module

$\overline{Nu_{upper}}$ = average Nusselt number for upper wall of a module

p = pressure

P = pressure

P = Peclet number

Pr = Prandtl number $\left(\mu_f c_{pf} \diagup k_f \right)$

$\overline{p}$ = average pressure

q = constant uniform heat flux $\left(\mathrm{W} \diagup \mathrm{m}^2 \right)$

$\dot{q}''$ = constant uniform heat flux $\left(\mathrm{W} \diagup \mathrm{m}^2 \right)$

R = residual as defined by Equations 4.54-5.57

Re = Reynolds number $\left(2\rho_f u_o H \diagup \mu_f \right)$

Re_H = Reynolds number based on hydraulic diameter

$\boldsymbol{r}$ = body force

S = source term

T = temperature $\left(C^o \right)$

T_b = bulk temperature

T_w = wall temperature

U = axial velocity component $\left({}^{m}\!/_{s} \right)$

u = axial velocity component $\left({}^{m}\!/_{s} \right)$

u_o = inlet velocity

$\boldsymbol{u}$ = velocity vector

u_{bulk} = bulk velocity of the channel

V = transverse velocity component $\left({}^{m}\!/_{s} \right)$

V = control volume

v = transverse velocity component $\left({}^{m}\!/_{s} \right)$

W^* = non-dimensionless baffle thickness $\left({}^{\mathrm{H}}\!/_{\mathrm{w}} \right)$

w = baffle thickness (m)

XU = location of u-velocities in x-direction

x = axial coordinate

y = transverse coordinate

Greek Symbols

α = under relaxation factor

Δ = length of control volume

δ = diffusion length, distance between grid points

ε = porosity

Γ = diffusion coefficient

μ = dynamic viscosity $\left(\mathrm{N.s}/\mathrm{m}^2 \right)$

ρ = density $\left(\mathrm{Kg}/\mathrm{m}^3 \right)$

$\tilde{\boldsymbol{\tau}}$ = stress tensor for Newtonian fluid

ϕ = general variable

Ψ = stream function

Ψ^* = non-dimensional stream function

$< >$ = intrinsic volume averaged

Subscript

b = bulk

C = constant

d = dispersion

E = east control volume center

e = east control volume's interface

eff = effective

f = fluid

i = interface porous/fluid

N = North control volume center, or expansion factor (1.4)

n = north control volume's interface

P = center of current control volume

p = porous

S = South control volume center

s = solid or south control volume’s interface

W = west control volume center

w = west control volume’s interface

w = wall

x = local

Superscript

f = pore

o = initial condition

s = solid

u = u-velocity locations

v = v-velocity locations

$'$ = fluctuating components or correction value

* = dimensionless quantity or guessed value

REFERENCES

[1] Huang, P. C., and Vafai, K., 1994, “Analysis of Forced Convection Enhancements in a Channel Using Porous Baffles”, Journal of Thermophysics and Heat Transfer, **8**(3), pp. 563-573.

[2] Ould-Amer, Y., Chikh, S., Bouhadef, K., and Lariat, G., 1998, “Forced Convection Cooling Enhancements by Using Porous Materials”, International Journal of Heat and Fluid Flow, **19**, pp. 251-258.

[3] Kim, S. J., and Vafai, K. 1990, “Analysis of Surface Enhancement by a Porous Substrate”, ASME Journal of Heat Transfer, **112**, pp. 700-706.

[4] Amiri, A., Vafai, K., and Kuzay, T. M., 1995, “Effects of Boundary Conditions on Non-Darcian Heat Transfer Through Porous Media and Experimental Comparison”, Numerical Heat Transfer, **27**, Part A, pp. 651-664.

[5] Sung, H. J., Kim, S. Y., and Hyun, J. M., 1995, “Forced Convection from an Isolated Heat Source in a Channel with Porous Medium”, International Journal of Heat and Fluid Flow, **16**, pp. 527-535.

[6] Webb, B. W., and Ramadhyani, S., 1985, “Conjugate Heat-Transfer in a Channel with Staggered Ribs”, International Journal of Heat and Mass Transfer, **28**(9), pp. 1679-1687.

[7] Vafai, K., and Tien, C. L., 1981, “Boundary and Inertia Effects on Flow and Heat Transfer in Porous Media”, International Journal of Heat and Mass Transfer, **24**, pp. 195-203.

[8] Kim, S. Y.; Kang, B. H.; Kim, J. H.; 2001, "Forced Convection from Aluminum Foam Materials in an Asymmetrically Heated Channel", International Journal of Heat and Mass Transfer, **44**, pp. 1451-1454.

[9] Kelkar, K. M., 1990, “Iterative Method for the Numerical Predication of Heat Transfer in Problems Involving Large Difference in Thermal Conductivity”, Numerical Heat Transfer, **17**, Part B, pp. 113-128.

[10] Patankar, S. V. and D. B. Spalding, 1972, "A Calculation Procedure for Heat, Mass and Momentum Transfer in Three-Dimensional Parabolic Flows", International Journal of Heat and Mass Transfer, **15**, pp. 1787-1806.

[11] Van Doormal, J. P. and Raithby, G. D., 1984, "Enhancements of the SIMPLE Method for Predicting Incompressible Fluid Flows", Numerical Heat Transfer, **7**, pp. 147-163.

[12] Patankar, S. V., 1980, "*Numerical Heat Transfer and Fluid Flow*", Taylor & Francis, Bristol, PA.

[13] Mills, A. F., 1999, "*Heat Transfer*", Prentice Hall, Inc., Upper Saddle River, NJ.

[14] Nakayama A., 1995, "*PC-Aided Numerical Heat Transfer and Convection Flow*", CRC Press, Inc., Boca Raton, FL.

[15] Patankar, S. V., 1991, "*Computation of Conduction and Duct Flow Heat Transfer*", Innovative Research, Inc., Maple Grove, MN.

[16] Kays, W. M.; Crawford, W. E., 1993, “*Convective Heat and Mass Transfer*”, McGraw-Hill, Inc, New York.

VITA

Bruno Monte da Silva Miranda (born on December 10, 1973 in Margao, Goa, India) received a degree of Bachelor in Engineering in Mechanical Engineering from N.E.D University of Engineering & Technology, Karachi in April 1998. In Jan 2000 he joined Texas A&M University, College Station, Texas to pursue his M.S. degree in Mechanical Engineering.

All correspondence should be addressed care of author's mother:

Zelia de Sa Miranda
17006 88th Ave Apt 4A,
Jamaica, NY 11432-4539,
USA